

UNIVERSITY OF OKLAHOMA  
GRADUATE COLLEGE

AGN AND THEIR ENVIRONMENT: A MULTI-WAVELENGTH  
PHOTOMETRIC AND SPECTROSCOPIC STUDY OF AGN AND GALAXY  
CLUSTERS, AND THE CO-EVOLUTION OF AGN AND THE LARGE SCALE  
STRUCTURES

A DISSERTATION  
SUBMITTED TO THE GRADUATE FACULTY  
in partial fulfillment of the requirements for the  
Degree of  
DOCTOR OF PHILOSOPHY

By

Hora D. Mishra  
Norman, Oklahoma  
2022

AGN AND THEIR ENVIRONMENT: A MULTI-WAVELENGTH  
PHOTOMETRIC AND SPECTROSCOPIC STUDY OF AGN AND GALAXY  
CLUSTERS, AND THE CO-EVOLUTION OF AGN AND THE LARGE SCALE  
STRUCTURES

A DISSERTATION APPROVED FOR THE  
HOMER L. DODGE DEPARTMENT OF PHYSICS AND ASTRONOMY

BY THE COMMITTEE CONSISTING OF

Dr. Xinyu Dai, Chair

Dr. Phillip Gutierrez

Dr. Nathan Kaib

Dr. Martin Montminy

Dr. Ferah Munshi



To my family, who inspired me to pursue Astrophysics, and always encouraged me in my endeavors. And to the family I gained during my PhD journey. I am extremely grateful to have these people in my life, and for all the support that I have received.

# Acknowledgements

I would like to acknowledge my advisor Dr. Xinyu Dai who gave me the opportunity to study the extra-galactic universe and guided me during the course of my PhD. I would also like to acknowledge the support I received from my undergraduate and graduate professors who taught me various Physics and Astronomy courses, helped me with research and paper-writing, and provided me with mentorship throughout my education. I would especially like to extend my gratitude to Dr. Chris Kochanek, Dr. Ferah Munshi, Dr. Phil Gutierrez, Dr. Ron Kantowski, Dr. Joel Rauber, and Dr. Dan Smith.

# Table of Contents

<b>1</b>	<b>Introduction</b>	<b>1</b>
1.1	The Large-Scale Structure . . . . .	1
1.1.1	Galaxy Clusters . . . . .	1
1.1.2	Fields . . . . .	7
1.1.3	Cosmic Voids . . . . .	7
1.2	Active Galactic Nuclei . . . . .	9
1.2.1	The AGN Structure . . . . .	9
1.2.2	AGN Classification . . . . .	12
1.2.3	Unification Theory for AGN . . . . .	14
1.3	The AGN-Environment Co-evolution . . . . .	14
1.4	Dissertation Summary . . . . .	16
1.4.1	Telescopes, Instruments, and Organizations . . . . .	17
<b>2</b>	<b>Lower AGN Abundance in Galaxy Clusters at <math>z &lt; 0.5</math></b>	<b>20</b>
2.1	Introduction . . . . .	20
2.2	The Data . . . . .	23
2.2.1	Cluster Sample . . . . .	23
2.2.2	SDSS and WISE Galaxy Catalogs . . . . .	25
2.3	Methodology . . . . .	26
2.4	Results . . . . .	28
2.4.1	Dependence on environment . . . . .	28
2.4.2	Dependence on redshift . . . . .	29
2.4.3	Dependence on angular cluster-centric distance . . . . .	30
2.4.4	Dependence on absolute magnitudes . . . . .	31
2.5	Discussion . . . . .	33
2.6	Conclusions . . . . .	38
2.7	Acknowledgements . . . . .	39
<b>3</b>	<b>Active Galactic Nuclei Abundance in Cosmic Voids</b>	<b>47</b>
3.1	Introduction . . . . .	47
3.2	Data and Methodology . . . . .	50
3.2.1	Galaxy Catalogs . . . . .	50
3.2.2	Quasar Catalog . . . . .	51
3.2.3	The Void Sample . . . . .	51
3.2.4	Methodology . . . . .	52
3.3	Results . . . . .	53
3.4	Discussion and Conclusions . . . . .	55
3.5	Acknowledgements . . . . .	58
<b>4</b>	<b>The Changing Look Blazar B2 1420+32</b>	<b>64</b>
4.1	Introduction . . . . .	64
4.2	Temporal Evolution . . . . .	67
4.3	Spectral Evolution . . . . .	71
4.4	Discussion . . . . .	75

4.5	Acknowledgements . . . . .	80
<b>5</b>	<b>The Swift AGN and Cluster Survey: Detecting X-ray Galaxy Clusters</b>	<b>94</b>
5.1	Introduction . . . . .	94
5.2	Data Reduction and Source Detection . . . . .	96
5.3	Extended Source Analysis and Discussion . . . . .	98
<b>6</b>	<b>Conclusion</b>	<b>105</b>
6.1	Chapter Summaries . . . . .	105
<b>7</b>	<b>References</b>	<b>108</b>

# List of Tables

2.1	AGN fraction in clusters and fields for the five redshift bins . . . . .	46
3.1	AGN fraction in inner and outer void regions for the five redshift bins . . .	63
4.1	B2 1420+32 spectra continuum analysis . . . . .	88
4.2	B2 1420+32 spectra emission line analysis . . . . .	89
4.2	B2 1420+32 spectra emission line analysis (continued) . . . . .	90
4.2	B2 1420+32 spectra emission line analysis (continued) . . . . .	91
4.3	B2 1420+32 optical lightcurves . . . . .	92
4.4	B2 1420+32 Fermi LAT lightcurves . . . . .	93



# List of Figures

1.1	Cosmic web schematic . . . . .	18
1.2	AGN unification scheme . . . . .	19
2.1	Cluster luminosity versus redshift . . . . .	40
2.2	Optical and mid-IR color-magnitude diagram . . . . .	41
2.3	AGN fraction versus redshift . . . . .	42
2.4	Relative AGN fraction versus redshift . . . . .	43
2.5	AGN fraction versus clustercentric distance . . . . .	44
2.6	AGN fraction versus SDSS absolute magnitude . . . . .	45
3.1	Cosmic void redshift distribution . . . . .	60
3.2	Void AGN fraction versus redshift . . . . .	61
3.3	Void AGN radial profile . . . . .	62
4.1	B2 1420+32 light curves in optical and gamma-ray bands . . . . .	82
4.2	Multi-band optical and Fermi LAT light curves . . . . .	83
4.3	Cross-correlation between optical and gamma-ray light curves . . . . .	84
4.4	Spectroscopic evolution of B2 1420+32 . . . . .	85
4.5	Spectroscopic evolution of B2 1420+32 in absolute flux units . . . . .	86
4.6	Evolution of flux and equivalent width . . . . .	87
5.1	Core radius versus offaxis angle . . . . .	100
5.2	Core radius versus signal-to-noise ratio . . . . .	101
5.3	Core radius distribution . . . . .	102
5.4	The offaxis angle distribution . . . . .	103
5.5	Signal-to-noise ratio distribution . . . . .	104

# Abstract

Active galactic nuclei (AGN) are the central engines hosted by most of the galaxies in the universe and are believed to be actively accreting supermassive black holes. The growth of the central black hole is very closely tied with the host galaxy evolution, as demonstrated by relations like the  $M-\sigma$  relation. AGNs strongly influence galactic evolution by affecting star formation, as well as impacting their large-scale environment consisting of clusters, groups, and voids, via various feedback mechanisms. In addition, AGNs allow us to understand black hole physics and the evolution of supermassive black holes through the accretion processes. For my PhD research, I have attempted to understand the evolution of AGN and the role that the interplay between AGNs and the large-scale environment plays in their evolution, and have worked on the detection of galaxy clusters. For the first part of my dissertation, I have presented our investigation of the abundance of AGNs in galaxy clusters and the surrounding low-density fields using multi-wavelength surveys. We have found a decreasing fraction of AGN with increasingly denser environments –  $(2.37 \pm 0.39)\%$  in clusters and  $(5.12 \pm 0.16)\%$  in fields. This shows an environmental dependence of AGN activity. For the second part, I have presented our study of the abundance of AGNs in cosmic voids. We have found higher average fractions in the inner voids  $(4.9 \pm 0.7)\%$  than in the outer void regions  $(3.1 \pm 0.1)\%$  at  $z > 0.42$ . At low redshifts ( $z < 0.42$ ), we have found very weak AGN activity dependence on the environment. The third part of the dissertation has detailed a multi-wavelength study of a changing look blazar, B2 1420+32. We have discovered a multi-transitional changing look blazar with unprecedented photometric and spectroscopic variabilities and complex spectral features. Multi-epoch lightcurves spectra have shown very large gamma-ray and optical variability, by factors of up to 40 and 15, respectively, on week to month timescales. Over a 15-year period, the gamma-ray and optical fluxes have been ob-

served to increase by factors of 1500 and 100, respectively. Most emission line flux variations, except the Fe continuum, have been seen to be within a factor of 2–3, implying that the transitions between FSRQ and BL Lac classifications are mainly caused by the continuum variability. Finally, in the last part of the dissertation, I have presented the initial analysis for the detection of X-ray selected galaxy clusters using the SWIFT Observatory data as part of the Swift AGN and Cluster Survey (SACS) sequence.

# Chapter 1

## Introduction

### 1.1 The Large-Scale Structure

#### 1.1.1 Galaxy Clusters

Galaxy clusters are the largest and the most massive gravitationally-bound large scale structures found in the universe. They are located at the overdensity peaks (densest points) of the cosmic web, connected by the filaments, which are surrounded by vast underdense regions called cosmic voids (see Figure 1.1). Galaxy clusters are crucial to the understanding of the formation of structures and the distribution of matter on the largest scales (e.g., Abell 1958; Borgani et al. 1995). According to the current hierarchical structure formation theory, the formation of galaxy clusters is rooted in the gravitational collapse of the overdensity peaks from the initial dark matter density field fluctuations in the early universe (e.g., Bardeen et al. 1983; León et al. 2018; Gilman et al. 2022). In a bottom-up assembly model, small-mass dark matter halos constantly grow by attracting the surrounding matter to create proto-cluster regions containing small-mass collapsed objects and resulting in significant redistribution of mass and angular momentum (e.g., Lukić et al. 2009; Mo et al. 2010; Bhattacharya et al. 2013). Hierarchical growth of these systems occurs via collisions and mergers as they continue to form larger and larger virialized structures, that eventually evolve into the galaxy clusters we see in the present-day universe (e.g., Kravtsov & Borgani 2012; Li et al. 2022).

Conventionally, structures with concentration of less than 50 galaxies are called galaxy groups and structures with 50 or more galaxies are called clusters (e.g., Bahcall & Cen 1993; Bahcall 1996). These range from tens of galaxies (poor clusters) to

hundreds and thousands of galaxies (rich clusters, like the Coma cluster). Clusters are a few Mpc in size and their masses range from  $10^{14}$  to  $10^{15} M_{\odot}$  (e.g., Oort 1983; Dressler 1984).

Clusters are relatively young and rare in the universe, and their number density and distribution in space is heavily influenced by the properties of dark matter and dark energy and the density fluctuations in the dark matter field in the early universe, making them sensitive to the cosmological parameters that govern the structure growth and geometry of the observable universe (e.g., Bertschinger 1998; Coles & Lucchin 2002; Murata et al. 2019). This implies that clusters are extremely useful to independently constrain the cosmology and compare it against other cosmic phenomena used to probe the parameters of structure growth, such as the cosmic microwave background (CMB) (e.g., Sunyaev 1974; Miller et al. 1999; Fixsen 2009; Legrand & Carron 2022) and the Baryonic Acoustic Oscillations (BAO) (e.g., Sunyaev & Zeldovich 1970; Bassett & Hlozek 2010; Alam et al. 2021).

Galaxy clusters are made up of several components, galaxies, intra-cluster medium, and dark matter. They are dominated by dark matter, which is the biggest constituent of the cluster mass ( $\sim 85\%$ ) (e.g., Ostriker et al. 1974; Faber & Gallagher 1979; Randall et al. 2016). Zwicky 1933 is one of the first and most widely cited works in the field of dark matter and is based on the observations of a galaxy cluster, the Coma cluster. Fritz Zwicky observed the discrepancy in the mass needed to keep galaxies from escaping the gravitational potential of the Coma cluster due to the very high velocity dispersions of the member galaxies, and concluded that there must be a much greater amount of dark matter present in clusters than luminous matter. The most widely accepted version of dark matter is a weakly interacting, cold dark matter (CDM) (e.g., Peebles 1982; Zhang & Huang 2018; Abbott et al. 2019). The dark matter halo density profile is described by the Navarro-Frenk-White (NFW) profile (e.g., Navarro et al. 1996; Bhattacharya et al. 2013; Xu & Randall 2020).

Majority of the baryonic (luminous) matter resides in the intra-cluster medium (ICM) (e.g., Sarazin 1986; Plionis et al. 2008; Zuhone & Markevitch 2009). The ICM is a hot, dense, diffuse plasma, with typical temperature ranges of  $10^7 - 10^8$  K (e.g., Jones & Forman 1984; David et al. 1993). Its density is in the range  $10^{-4} - 10^{-2}$   $\text{cm}^{-3}$  (e.g., Jones & Forman 1992), with lower densities in the outer regions of the clusters to the upper limit of this range found near the core of relaxed clusters. The temperature of the ICM is dependent on the mass of the cluster and the depth of its gravitational potential well, and it cools via emitting radiation, dominated by the thermal bremsstrahlung. The cooling timescale is given by

$$t_{cool} \sim 8.5 \times 10^{10} \text{yr} \left( \frac{n_p}{10^{-3} \text{cm}^{-3}} \right)^{-1} \left( \frac{T}{10^8 \text{K}} \right)^{1/2}, \quad (1.1)$$

where  $n_p$  is the proton density and  $T$  is the plasma temperature (Takizawa 1998). The gas cooling timescale is greater than the age of the universe (Hubble time), except in the innermost regions of the cluster where the proton density is high (e.g., Takizawa 1998). The intra-cluster medium is weakly magnetized, with magnetic fields ranging between  $0.1 \mu\text{G}$  and a few  $\mu\text{G}$  (e.g., Dolag et al. 2001; Govoni et al. 2001). The ICM's temperature range indicates it is a highly ionized plasma, and elements, such as H and He are completely ionized. Heavy elements, like O, Mg, Si, Ar, Ca, Fe, and Ni, are partly ionized and it has metallicity about a half to a third that of the Sun (e.g., Molendi 2004; Mantz et al. 2017; Liu et al. 2020). The ICM radiates most dominantly in the X-ray wavelengths. The continuum emission comes from thermal bremsstrahlung, recombination, and two-photon decay of metastable levels (e.g., Jones & Forman 1984; Edge & Stewart 1991; Burg et al. 1994).

Depending on the cluster mass, galaxies in clusters constitute about 1% of its total mass and contain stars, gas, and dust (e.g., Dai et al. 2010, and references therein). 10-20% of galaxies reside in clusters and >50% of all galaxies live in galaxy

groups or clusters (e.g., Dressler 1980; Blanton & Moustakas 2009; Shimakawa et al. 2022). Properties and evolution of cluster member galaxies are heavily influenced by the cluster environment. Galaxy clusters are dominated by elliptical and lenticular galaxies (e.g., Dressler 1984, Blanton & Moustakas 2009; Lacerna et al. 2022). Elliptical galaxies are ‘red’ and ‘dead’ galaxies with very little ongoing star formation. Groups, on the other hand, are dominated by spiral galaxies with active star formation (e.g., Albert et al. 1977; Bamford et al. 2009; Andreon 2018). The extreme environments of galaxy clusters and groups, including the gravitational potential well, strongly influence galaxy evolution.

Galaxy clusters can be detected in different wavelength bands and detection in each band has its own advantages and disadvantages. Optical/IR surveys are the most common surveys to detect and generate large galaxy cluster catalogs. These surveys use optical (or IR) emission from the member galaxies to look for over-densities in galaxy distribution to identify clusters (e.g. Gladders & Yee 2000; Yee & Gladders 2002; Gilbank et al. 2004). There are different methods used to search for these over-densities, employed by photographic cluster surveys (e.g., Abell 1958; Zwicky et al. 1968; Baumann et al. 2002) and digital imaging surveys, which have utilized wide-area sky surveys, like the Sloan Digital Sky Survey (e.g., Popesso et al. 2004) and the Palomar Deep Cluster Survey (Postman et al. 1996). These methods are very sensitive to projection effects along the line-of-sight and can suffer from contamination when detecting over-densities in the 3-D space due to the two-dimensional photometric data which is typically analyzed. The most widely used technique to detect galaxy over-densities is the red-sequence method, which is based on the observational fact that majority of the red, passively-evolving early-type galaxies in rich clusters seem to follow a strict, linear color-magnitude relation (cluster red sequence) (e.g., Gladders & Yee 2000; Yee & Gladders 2002; Mehrtens et al. 2012). These galaxies show little to no star formation. The cluster red sequence (CRS) is

characteristic of the reddest galaxies in a group of galaxies at the same redshift on the color-magnitude diagram. A well-defined and tightly correlated CRS has been observed to high redshifts and allows for the identification of clusters up to high redshifts since it is known that these early-type galaxies prefer the dense cluster environment at any epoch (e.g., Lidman et al. 2008; Strazzullo et al. 2010). Another technique to detect galaxy clusters is through the Sunyaev–Zel’dovich (SZ) effect, in which the Cosmic Microwave Background (CMB) is distorted due to inverse Compton scattering of the radiation by hot electrons in clusters (Zeldovich & Sunyaev 1969). The CMB distortions are a signature of density differences in the universe and can be used to trace high-density clusters. In addition, the SZ effect can be used to detect clusters at high redshifts because it is independent of redshift and does not suffer from the redshift detrimental effect (e.g, Komatsu & Kitayama 1999; Hajian et al. 2013; Gong et al. 2019).

Following the first detection of X-ray emission from an extragalactic source in 1966, from a region around the galaxy M87 in the center of the Virgo cluster, other rich nearby clusters, such as the Coma cluster, were observed to emit X-rays (e.g., Byram et al. 1966; Meekins et al. 1971). The Uhuru X-ray satellite detected X-ray emission from several galaxy clusters (Giacconi et al. 1972). Galaxy clusters were found to be spatially extended, diffused extragalactic sources of X-rays, with sizes that match the distribution of galaxies in these clusters. This X-ray emission comes from the ICM (intra-cluster medium) and is dominated by the thermal bremsstrahlung radiation, with mean temperatures in the range of  $10^7 - 10^8$  K. Please see above for more details on the ICM. The detection of clusters as powerful X-ray sources has opened a new door into the investigation of the properties and evolution of galaxy clusters. X-ray surveys provide an important tool to study the ICM temperature, luminosity, metallicity, gas density, as well as to calculate the cluster mass. Correlations have been observed between the ICM temperature and cluster



properties, such as velocity dispersion of galaxies (e.g., Holt & McCray 1982; Ettori 2015; Lovisari et al. 2020). There has been extensive work done to find scaling relations which relate the total cluster mass to X-ray observables, with small scatter and robustness in the slope and redshift evolution (e.g., Stanek et al. 2006; Ettori et al. 2012). Three important scaling relations that describe the relationship between total cluster mass and different cluster properties are the X-ray luminosity–mass (e.g., Stanek et al. 2006; De Martino & Atrio-Barandela 2016; Lovisari et al. 2021), the X-ray luminosity–temperature (e.g., Edge & Stewart 1991; Markevitch 1998), and the mass–temperature (e.g., Evrard et al. 1996; Eke et al. 1998) relations. Self-similar models based on gravity as being the dominant process predict these scaling relations as a power-law on average, with a scatter around the power-law which is a lognormal distribution (e.g., Kaiser 1986). However, observations from deep surveys suggest deviations from the power-law model suggesting that non-gravitational processes may be significant in the evolution of cluster properties (e.g., Eckmiller et al. 2011). X-ray luminosity-temperature scaling relation is traditionally the best-studied relation in literature.  $L_X$ –T relation based on self-similarity models has been shown to have shallower slope, indicating the influence of dissipative processes, such as AGN feedback, radiative cooling, and star formation, which would play an important role in the change in entropy of the cluster system (e.g., Giodini et al. 2013; Zhang et al. 2021). Pratt et al. (2010) used the REXCESS sample (XMM-Newton cluster structure survey; Böhringer et al. 2007) and found that the ICM entropy got closer to the self-similar model close to  $R_{500}$ , while it was shallower near the cluster potential, pointing to a heating source in the core of the cluster. The  $L_X$ –T relation has also been found to be different for galaxy groups than rich clusters, exhibiting a steeper slope (e.g., Helsdon & Ponman 2000; Davé et al. 2008). Here,  $R_\delta$ , and its corresponding  $M_\delta$ , refer to the radius and mass of the cluster corresponding to the overdensity contrast as compared to the critical density,  $\rho_c(z)$ , of the universe.  $R_{500}$  is defined as

the region where the density of the cluster is 500 times the critical density value and is an important parameter used to define the extent of galaxy clusters. Other radii, such as  $R_{200}$  and  $R_{100}$ , are also used in the context of a galaxy cluster study. The  $L_X$ -mass relation provides a useful tool to determine the total mass of the system. However, this scaling relation gives the maximum scatter and is difficult to derive for clusters in a dynamical state where mergers and cooling effects cause deviations from regular, relaxed systems which are in hydrostatic equilibrium (Eckmiller et al. 2011; Giodini et al. 2013).

### 1.1.2 Fields

The dense compact galaxy clusters open out into long filamentary structures and two-dimensional sheets which surround the relatively empty spaces of voids. Cosmic filaments are the largest known structures in the cosmic web and may span up to  $80 \text{ Mpc h}^{-1}$  in length (e.g., Geller & Huchra 1989; Bond et al. 1996). They contain most of the universe's mass in the form of dark matter, galaxies, and groups. These filamentary structures connect clusters, and contain the low-density field regions surrounding the clusters (Poudel et al. 2017; Libeskind et al. 2018). Isolated galaxies and galaxy groups inhabit filaments and account for about half of the galaxies in the local universe (e.g., Tempel et al. 2014; Mesa et al. 2018).

### 1.1.3 Cosmic Voids

Voids are the underdense regions of almost empty space surrounded by the filaments. They contain no to few isolated galaxies. With radii spanning in the range of tens of Mpc and even up to a hundred Mpc, they make up the majority of the universe's volume (e.g., Zeldovich et al. 1982; Pan et al. 2012; Sahlén et al. 2016). Moderate density fluctuations during recombination epoch would result in the underdensities

of cosmic voids observed today (Kirshner et al. 1981; Elyiv et al. 2013; Hawken et al. 2020). Voids grow hierarchically and merge to form larger voids, while void substructures may remain inside larger voids after mergers (e.g., Sahni et al. 1994). They are characterized as being spherical in shape to first approximation and as they expand, their ellipticity reduces further, while being very sensitive to the cosmological parameters (e.g., Lee & Park 2006; Verza et al. 2019). However, the influence of their surrounding large-scale structures (clusters and filaments) prevents them from being perfect spheres (e.g. Icke 1984; Platen et al. 2008). As voids expand, they are further depleted of gas and dark matter, however it is also expected that some of the dark matter and gas in dense cluster environments can break through due to processes like mergers and end up in these empty regions (Ceccarelli et al. 2006; Paz et al. 2013). Ceccarelli et al. (2013) define two void types based on the observed radial density profiles of SDSS voids - (i) R-type voids, which have a continuous distribution of density, which is increasing outward, and (ii) S-type voids, which have a discrete density profile where the void region is surrounded by an overdense region (shell). They find that the larger voids tend to show a more smooth transition in density, indicating an R-type. In such a scenario, the void evolution seems to be through a merger process where smaller voids merge to grow larger over time (e.g., Sheth & van de Weygaert 2004; Sutter et al. 2014). On the other hand, smaller voids typically tend to be S-type because they get compressed due to the collapse of overdensity surrounding these voids and get trapped in its gravitational potential.

Cosmic voids are important probes of global cosmological parameters and are useful tools to study modified gravity, dark matter, dark energy, and density perturbations in the primordial universe, due to their sensitivity to components, such as neutrinos and dark energy (e.g., Pisani et al. 2019, and references therein). The physical structure and dynamical evolution of voids have been shown to be closely linked to the dark energy equation of state (e.g., Lavaux & Wandelt 2010). Due to

the less dramatic nature of void evolution as compared to galaxy clusters, voids have preserved the signatures of the early Universe (e.g., Mishra et al. 2021b, and references therein). The outward flow of matter from center of voids toward filaments and sheets, and the redshift space distortions can be used to calculate the mass density of the universe, which can be used to determine the amount of dark matter present (e.g., Dekel & Rees 1994; Bos et al. 2012; Vallés-Pérez et al. 2021).

## 1.2 Active Galactic Nuclei

### 1.2.1 The AGN Structure

Most galaxies have a supermassive black hole at their center. A few of these central engines actively accrete mass onto themselves and emit strong radiation powered by the gravitational potential of the black hole and which spans the entire electromagnetic spectrum (e.g., Mayall 1939; Shields 1999; Fabian & Rees 1995; Mishra & Dai 2020). These objects are known as active galactic nuclei (AGN). They are one of the brightest sources and most powerful astrophysical sources in the universe, emitting at very high luminosities of the order of  $L_{bol} \sim 10^{47} - 10^{48} \text{ erg s}^{-1}$  (e.g., Fabian 1999; Woo & Urry 2002). AGN emit powerful radiation at all the wavelengths of the electromagnetic spectrum. The basic structure of an AGN is known through the radiation emitted by different AGN components in different electromagnetic bands. The accretion disk is the disk around the supermassive black hole which is formed due to the angular momentum of the infalling gas onto the supermassive black hole and actively accretes mass onto itself (e.g., Malkan 1983; Begelman 1985; Begelman 1989). In the radiation mode, the gravitational potential energy is converted to electromagnetic radiation and the accretion disk dominates the continuum emission from the AGN (Jiang et al. 2013; Cielo et al. 2018). The accretion disk has a temperature profile of increasing temperature toward the center of the disk (e.g., Blackburne et

al. 2011; Jiang & Blaes 2020). There is the presence of a corona (e.g., Jha et al. 2022) which emits inverse-Compton radiation with a size of about 10 gravitational radii (e.g., Dai et al. 2010). The flow of gas can result into an optically thick disk which is geometrically thin, or an optically thin disk with high temperatures. Different models have been proposed to describe the gas flow, such as the advection-dominated accretion (Narayan & Yi 1995), the convection-dominated accretion (Igumenshchev et al. 1999), and the Shakura and Sunyaev disk model (Shakura & Sunyaev 1973). The broad-line region (BLR) surrounding the accretion disk produces broad emission lines dominantly in the optical and ultraviolet bands. The width of this emission, which occurs in high density gas, can range from  $1000 - 25000 \text{ km s}^{-1}$  (e.g., Done & Krolik 1996; Czerny & Hryniewicz 2011). There is a scaling relation between the BLR and AGN continuum luminosity, where the BLR is photoionized by the continuum radiation with a short time delay (Kaspi et al. 2005; Czerny & Hryniewicz 2011). Reverberation mapping has been a popularly used in AGN physics to measure the lag in light travel time in different emission regions of the AGN and study the size and structure of the accretion disk and the BLR (e.g., Kaspi et al. 2005; Uklein et al. 2019; Yu et al. 2020). The narrow-line region (NLR) can have widths of the order of hundreds of  $\text{km s}^{-1}$  (e.g., Ramos Almeida & Ricci 2017) and shows correlation with the BLR emission. However, unlike the BLR, the NLR emission doesn't show variability on very short timescales and is distributed over a much bigger region (e.g., Elvis 2000; Elitzur 2012; Storchi Bergmann 2015).

The next component of an AGN is the dusty torus surrounding the accretion disk and the BLR. Based on infrared (IR) and interferometry observations, it spans a few parsecs in size and is a compact, optically thick cloud of dust and gas (e.g., Elitzur 2006). The inner torus radius is correlated to the AGN luminosity. The dust absorbs the AGN's radiation and emits in the IR band at temperatures  $\sim 2000 \text{ K}$  (e.g., Antonucci 1993; Pier & Krolik 1993). While majority of the dust emits in the

mid-IR, the cooler component of the torus (sub-mm range) extends to a larger region (Pier & Krolik 1992; Krolik 2007). Torus models in the literature can be divided into two categories based on the processes which are considered while describing its structure: models which look at AGN feedback, disc stability etc. and models which take into account the composition and geometry of the dust cloud (e.g., Ramos Almeida & Ricci 2017; García-González et al. 2017; González-Martín et al. 2019). The torus plays a crucial role in the optical classification of AGN into type 1 and type 2 objects. Type 1 AGNs are unobscured AGN where the central engine is visible, whereas the supermassive black hole and the BLR tend to be obscured by dust from the torus in type 2 AGNs. In type 1 AGNs, the IR emission accounts for about 10% of the bolometric luminosity (Jaffe et al. 2004; Oh et al. 2015). On the other hand, IR emission is much more significant ( $\sim 50\%$  of the total luminosity) for type 2 AGNs (e.g., Jaffe et al. 2004; Osterbrock & Ferland 2006; Trindade Falcão et al. 2021). NGC1068 is a classic example of a type 2 AGN.

AGN jets form two collimated beams of relativistic particles perpendicular to the accretion disk and extend out to two lobes. Jets are produced on account of a spinning black hole in the presence of a magnetized accretion disk (e.g., Blandford 1990; Potter & Cotter 2013; Fan et al. 2018). They dominate the radio emission of the AGN electromagnetic spectrum, emitting via synchrotron radiation (relativistic charged particles are accelerated and emit radiation), and have a characteristic non-thermal emission (e.g., Begelman et al. 1984; Meier 2001; Pushkarev et al. 2012); however, they emit at all wavelengths, from radio to gamma-rays. Jet mode (radio mode) in AGNs occurs where the accretion is radiatively inefficient and the jet dominates the continuum emission. AGN jets can range from sub-parsec to Mpc scales, and at Mpc scales, these jets penetrate the host galaxy to impact their large-scale cluster environment (e.g., Burbidge 1956; Hardcastle & Croston 2020; Mishra et al. 2021a).

### 1.2.2 AGN Classification

AGN have several different classifications, such as quasars, Type 1, Type 2, Seyfert type 1, Seyfert type 2, radio-loud, radio-quiet, Blazars, BL Lac objects. Majority of these classifications are a result of orientation effects, presence of a jet component, host environment, and the widely-debated large-scale environmental effects. While these AGN classes are recognized individually, unification schemes have been proposed to identify AGN types which are fundamentally different and those which arise from orientation effects (e.g., Urry & Padovani 1995; Tadhunter 2016) (Figure 1.2). As mentioned previously, type 1 and type 2 AGNs are classified based on the presence and absence of BLR from dust obscuration respectively. Seyfert 1 galaxies are low luminosity AGN with broad emission lines, while Seyfert 2 galaxies have narrow line emission spectra (e.g., Antonucci & Miller 1985; Wilson 1997; Singh et al. 2011). Radio-loud AGN are characterized as having radio emission (at 5 GHz)  $\geq 10$  times the optical (B-band) flux (Kellermann et al. 1989; La Franca et al. 1994). Most AGN are radio-quiet AGN, which have similar optical spectra, but significantly low radio emission (e.g., Blundell & Beasley 1998; Panessa et al. 2019; Mishra et al. 2021a). Quasars (QSO) are extremely powerful AGN which outshine their entire host galaxy. Radio-loud QSO have powerful radio jets, and are characterized by compact radio source and broad emission lines. Their luminosities lie in the range  $10^{40}$  to  $10^{46}$  erg s<sup>-1</sup> (Blandford et al. 2019). Radio-loud QSO differ from narrow-line radio galaxies in that they exhibit a broad-line optical spectrum. Narrow-line radio galaxies are further classified into Fanaroff-Riley type I (low luminosity) and type II (high luminosity) radio galaxies (Fanaroff & Riley 1974; Saripalli 2012). At lower luminosities, radio-loud AGN are classified as broad-line radio galaxies. Radio-quiet QSO don't show significant radio activity and are much more common in the universe than their radio-loud counterparts (e.g., Sandage 1965; Laor & Behar 2008;

Sbarrato et al. 2021). Their luminosities lie in the range  $10^{38}$  to  $10^{40}$  erg s<sup>-1</sup> (e.g., Blandford et al. 2019).

Blazars are radio-loud QSO with their relativistic jet pointing along the line-of-sight of the observer. Due to relativistic beaming, they are one of the most powerful AGN sources and exhibit very high variability in all the electromagnetic bands at both short and long timescales (e.g., Kellermann 1992; Urry & Padovani 1995; Gaur et al. 2012). Blazars are dominated by jet emission and show high and variable polarization (e.g., Potter & Cotter 2013; Falomo et al. 2014; Pichel et al. 2020). This makes them very important to understand the particle acceleration processes in radio jets, the role of changing structure and geometry of the jets, and the interplay between the accretion disk and the jet. There are two blazar sub-types – flat-spectrum radio quasars (FSRQ) and BL Lacertae objects (e.g., Abraham et al. 1991; Padovani & Giommi 1995; Falomo et al. 2014; Mishra et al. 2021a). BL Lacertae objects are lower luminosity quasars named after their prototype BL Lacertae (Hoffmeister 1929; Schmitt 1968; Oke & Gunn 1974). They are characterized by their non-thermal continuum emission and featureless optical spectrum. In contrast, FSRQs have broad emission lines and are extremely luminous quasars (e.g., Smith et al. 1986 Mao et al. 2017; Garofalo et al. 2019). “Changing look” AGN are a special class of AGN where a source moves from one AGN type to another (e.g., Aretxaga et al. 1999; LaMassa et al. 2015; Green et al. 2017). The most common class of changing look AGN involves the AGN transforming between AGN Type I and Type II (e.g., Matt et al. 2003, Marchese et al. 2012; Katebi et al. 2019). Changing look AGNs allow us to study AGN evolution and the differences between the distinct AGN classes, as well as observed features influenced by orientation effects.



### 1.2.3 Unification Theory for AGN

Strong anisotropic radiation from radio-loud AGN which is orientation-dependent, has given rise to the need for AGN unification theories (e.g., Rowan-Robinson 1977; Antonucci & Miller 1985; Urry & Padovani 1995). Phenomena, such as dust obscuration and relativistic beaming alter the observed spectrum and produce different kinds of AGN. Thus, it is important to identify the parent AGN population and understand the differences between the AGN classes as they are intrinsic to the AGN or a result of orientation/geometrical effects. The optical unification scheme classifies AGN on the basis of the orientation of the torus and its obscuration causing the presence or absence of broad emission lines seen in the spectrum (Edelson et al. 1987; Antonucci 1993; Spinoglio & Fernández-Ontiveros 2021). For the radio unification, the orientation of the jet forms the basis for the classification into flat-spectrum (core dominated) and steep-spectrum (dominated by the end lobes) radio-loud AGN (e.g., Peacock 1987; Barthel 1989; Axon et al. 2000). Flat-spectrum and steep-spectrum radio QSO are believed to be the aligned types of Fanaroff-Riley type II radio galaxies (e.g., Fanaroff & Riley 1974; Urry 2004; Gu & Ai 2011). It is likely that the local unification differs from the unification at the quasar epoch (the peak of quasar space density) (e.g., Shaver et al. 1999; Waddington et al. 2001; Fanidakis et al. 2011; Rigby et al. 2011). While the role of obscuration in optical unification of AGN and the number of obscured AGNs is more debated than radio unification, deep, pointed multi-wavelength surveys to study obscured AGN at higher redshifts will provide greater insight into the optical AGN classes.

## 1.3 The AGN-Environment Co-evolution

It is well established that there is a strong correlation between properties of present-day galaxies and their environment. Observational data, as well as cosmological

simulations have provided useful insight into studying the complex environmental conditions in galaxies and clusters and their co-evolution with the central black hole. Relationships, such as the  $M$ - $\sigma$  relation (Ferrarese & Merritt 2000), which describes the correlation between stellar velocity dispersion of the galaxy bulge to the mass of the central supermassive black hole, demonstrate the co-evolution of the host-black hole system. For example, star formation in galaxies has been linked to AGN activity via the presence of a common fuel – cold gas reservoir (e.g., Boselli et al. 2014; Alberts et al. 2016; Ricarte et al. 2019; Travascio et al. 2020). Theoretical studies have found massive black holes at higher redshifts to be hosted by massive galaxies with large star formation rates and dominated by a bulge (e.g., Di Matteo et al. 2017; Marshall et al. 2020). Different environmental conditions in the host galaxy are responsible for triggering AGN in different AGN luminosity classes. Processes, such as galaxy interactions and mergers have been thought to be especially important for high luminosity AGNs (e.g., Bellovary et al. 2013; Mishra & Dai 2020). Extreme conditions in the cluster’s gravitational potential well, concentration of cold gas in the cluster halo, and pressure from the hot intracluster medium (ICM) significantly impact AGN evolution (Gunn, & Gott 1972; Marshall et al. 2018; Ricarte et al. 2020). Several studies show that dynamic cluster environments over the history of the universe have impacted the growth of AGN in dense environments (e.g., Eastman et al. 2007; Bufanda et al. 2017; Li et al. 2019; Mishra & Dai 2020). On the other hand, radiation from the AGN impacts evolution at galaxy and cluster scales via a process known as AGN feedback (e.g., Ciotti & Ostriker 1997; Silk 2005; Bluck et al. 2014). Feedback from the central black hole acts as a self-regulating process which prevents the gas in galaxies from cooling, which quenches the star formation and also limits the growth of the black hole (e.g., Kawata & Gibson 2005). Massive outflows and jets in radio-loud AGN producing X-ray emission on kiloparsec scales impact star formation in the host galaxy by redistributing the cold gas (Sambruna

et al. 2003; Shin et al. 2010; Robichaud et al. 2017). AGN feedback has become important in theoretical, numerical, and semi-analytic models of galaxy formation and evolution (e.g., Kaviraj et al. 2005; Springel et al. 2005; Di Matteo et al. 2005; Eckert et al. 2021). Physical processes like major and minor mergers have been well-studied in cosmological simulations to understand the possible role they might play in accreting gas from the inner regions of the galaxy. For example, McAlpine et al. (2018) use the hydrodynamical cosmological EAGLE simulation to study the rapid growth phase of SMBH and find that major galaxy interactions play a significant role in driving rapid SMBH growth at low redshifts.

However, the extent to which environment plays a role in the properties and evolution of galaxies and the relative importance of secular processes versus environmental effects (nature vs nurture) is still widely debated. Selection effects also play a significant role in determining the extent to which environmental factors impact the evolution at kiloparsec and megaparsec scales. While studies have found varying results on the degree at which the environment affects AGN activity and vice-versa, there is a general agreement that both are important and interconnected.

## 1.4 Dissertation Summary

This dissertation details the various projects undertaken during the course of the PhD to investigate active galactic nuclei (AGN) and their evolution and co-dependence with the large scale environment, and galaxy clusters. In chapter 2, I present the investigation of the relative rate of AGN occurrence in galaxy clusters and their fields. This chapter is reproduced from the following publication: Mishra, H. D. and Dai, X. 2020, AJ, 159, 69, “Lower AGN Abundance in Galaxy Clusters at  $z < 0.5$ ”, accepted in the *Astronomical Journal*. © AAS. Reproduced with permission. DOI: 10.3847/1538-3881/ab6225. In chapter 3, I present the comparative investigation

of AGN abundance in the inner and outer regions of cosmic voids. This chapter is reproduced from the publication: Mishra, H. D., et al. 2021, ApJL, 922, L17, “Active Galactic Nuclei Abundance in Cosmic Voids”, accepted in the Astrophysical Journal Letters. © AAS. Reproduced with permission. DOI: 10.3847/2041-8213/ac36d9. Chapter 4 details the discovery of a changing look blazar, B2 1420+32, with extreme photometric and spectral variabilities. Chapter 4 is reproduced from the publication: Mishra, H. D., Dai, X., et al. 2021, ApJ, 913, 146, “The Changing-Look Blazar B2 1420+32”, accepted in the Astrophysical Journal. © AAS. Reproduced with permission. DOI: 10.3847/1538-4357/abf63d. In chapter 5, I present the initial analysis of the detection of X-ray selected galaxy clusters from the NASA *Swift* catalog as an extension of the Swift AGN and Cluster Survey, to determine the number count of galaxy clusters and their properties.

### 1.4.1 Telescopes, Instruments, and Organizations

- Swift X-ray Telescope (XRT) (Gehrels et al. 2004)
- ROSAT All-Sky Survey (RASS) (Voges et al. 1999)
- Sloan Digital Sky Survey (SDSS) (Abazajian et al. 2003)
- Wide-field Infrared Survey Explorer (WISE) (Wright et al. 2010)
- All-Sky Automated Survey for Supernovae (ASAS-SN) (Shappee et al. 2014)
- Las Cumbres Observatory Global Telescope Network (LCOGT) (Brown et al. 2013)
- Fermi Large Area Telescope (LAT) (Atwood et al. 2009)
- The Transiting Exoplanet Survey Satellite (TESS) (Ricker et al. 2015)

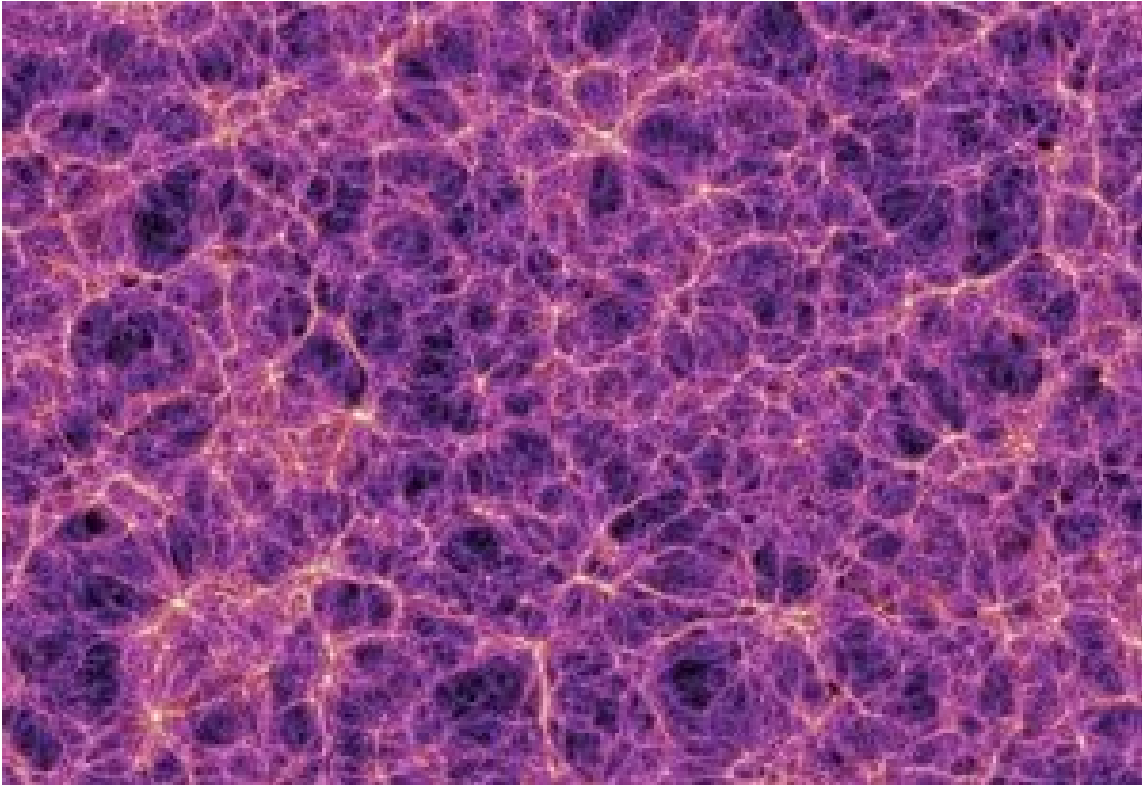


Fig. 1.1.— This diagram shows the cosmic web from the Millennium Simulation (Springel et al. 2005). Galaxy clusters are the bright points that are located at the intersection of extended filamentary structures, which surround the underdense cosmic voids (vast (almost) empty regions). This figure is reproduced from the following resource: <https://www.cta-observatory.org/science/gamma-rays-cosmic-sources/cosmic-web2/>

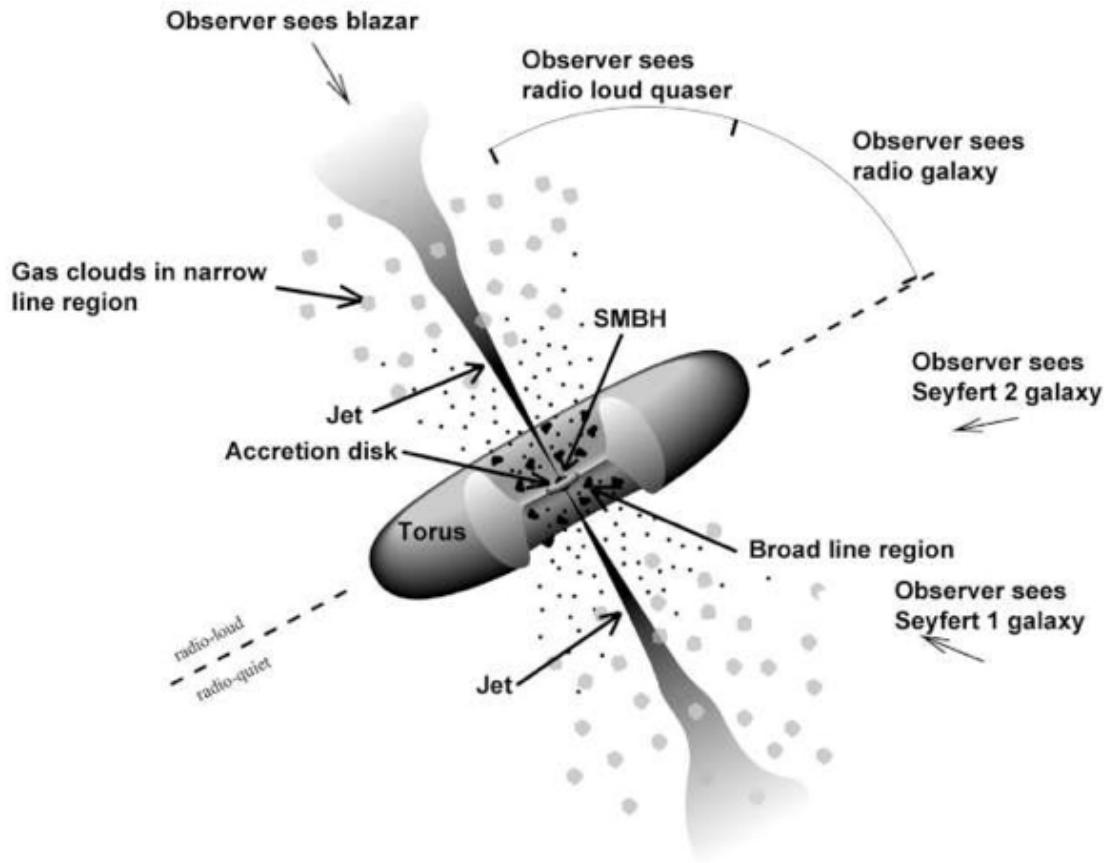


Fig. 1.2.— This diagram shows the structure of an active galactic nucleus (AGN) under the unified AGN model. The accretion disk surrounds the central supermassive black hole and open into the broad-line region. The broad-line region is enclosed in the dusty torus. This figure is reproduced from the following resource: <https://fermi.gsfc.nasa.gov/science/eteu/agn/>

## Chapter 2

# Lower AGN Abundance in Galaxy Clusters at

$$z < 0.5$$

### 2.1 Introduction

Most, if not all, galaxies have a supermassive blackhole (SMBH) at their center. Active galaxies are the ones that host active galactic nuclei (AGNs) where the supermassive black hole is accreting mass from the dense central region of the galaxy at a sufficiently high rate. For the luminous sample, the radiation from these supermassive black holes can outshine the entire host galaxy. It is not well understood why only a few SMBHs show such high nuclear activity. Galaxies are found in overdense regions of the universe which form the large-scale structures called galaxy clusters and also in very low density regions of filaments and voids. There is strong evidence that galaxy evolution is closely related to its environment, influencing star formation, stellar mass, and galaxy morphology (e.g. Alberts et al. 2016). Most massive early-type galaxies are typically found in galaxy groups and clusters, close to the center of a cluster's gravitational potential. However, large isolated galaxies have also been observed in the universe. While it is generally accepted that environment plays an important role in galaxy evolution, its role in triggering nuclear activity in active galaxies is still widely debated. The fraction of galaxies in clusters and fields that host these active SMBHs is an important probe of AGN fueling processes, cold interstellar medium at the centers of galaxies, galaxy's star formation rate, co-evolution of black holes and galaxies, and AGN influence on the local environment via the AGN feedback mechanism (e.g., Sanders et al. 1988; Hopkins et al. 2008). Powerful jets in radio-loud AGNs and/or AGN outflows interact with the surrounding interstellar

medium and can affect star formation rate in the galaxies hosting AGNs. Various local and global environmental factors, such as stellar mass density, distance from the cluster's center, cluster's velocity dispersion, cluster dynamics, host galaxy's morphology, and cosmological redshift may influence AGN fraction in clusters; however the relation between the two is not well understood. Many studies such as Lopes et al. (2017), Argudo-Fernández et al. (2018), and Ellison et al. (2019) find evidence for variation in fraction of AGNs with high and low-density environments, while several others see no to very weak correlation between the two (e.g. Miller et al. 2003; Pimblet et al. 2013; Yang et al. 2018; Man et al. 2019).

Several possible triggering mechanisms in clusters and fields to turn on the nuclear activity have been suggested, such as major and minor mergers (e.g. Di Matteo et al. 2005; Fontanot et al. 2015), disc instability (Dekel et al. 2009), bar influence (Shankar et al. 2012; Zhao et al. 2019), and tidal effects (Moore et al. 1996). Understanding the triggering mechanisms for these nuclei is crucial to the study of galaxy formation and evolution in the context of its environment. These processes are responsible for supplying gas for accretion onto the black hole, thus triggering it. Due to different accretion rates needed for different luminosity classes, it has been suggested that different physical processes are responsible for triggering the AGN. Of these processes, galaxy interactions and mergers have been thought to be especially important for high luminosity AGNs. Accretion of mass onto the black hole is possible via non-axisymmetric perturbation that triggers the AGN nuclear activity which has been observed to occur during mergers (Kawaguchi et al. 1998). Numerical simulations have shown tidal torques during mergers to efficiently move the gas inward to fuel rapid black hole mass accretion (e.g. Hernquist 1989; Springel et al. 2005; Alexander, & Hickox 2012). On the other hand, studies have found secular processes, such as minor mergers and disk instability to be the dominant mechanisms for triggering low luminosity AGNs (Hopkins, & Hernquist 2009; Hopkins et



al. 2014). Since clusters have significantly higher galaxy densities than fields, the rate of mergers is higher in clusters which would seem to trigger more AGNs in clusters. However, a combination of galaxy rich environment, extreme conditions in the cluster’s gravitational potential well, star formation rate, and concentration of cold gas in the cluster halo make the AGN dynamics more complex. Pressure from the hot intracluster medium (ICM) may cause suppressed AGN activity since it causes evaporation of the cold gas that accretes in the disk around the SMBH (Gunn, & Gott 1972). Studies show star formation to strongly co-evolve with AGN evolution (Alberts et al. 2016). Cold intracluster gas that drives star formation is also the primary fuel for AGN activity. Influence of galaxy mergers containing rich gas is similar on star formation in those galaxies to that on AGN fraction. Cluster halos, on the other hand, quench AGN formation by capturing cold gas and preventing accretion in the inner parts of the cluster by a process called “strangulation” (Larson et al. 1980). In the AGN phase model where most black holes in galaxies undergo an intense activity period, the lifetimes of emission at AGN luminosities are estimated to be in the range  $10^6 - 10^8$  years. Based on models of black hole growth via gas inflows, the strong accretion phase lasts for  $\sim 10^8$  years (Kauffmann, & Haehnelt 2000; Hopkins et al. 2005; Shankar et al. 2009).

Studying the impact of environmental factors on AGN fraction necessitates an investigation into the evolution of galaxies, clusters, and inter- and intracluster medium over cosmic time. Several studies show that dynamically evolving cluster environments over the history of the universe have affected AGN fractions in both clusters and fields (Eastman et al. 2007; Bufanda et al. 2017). In the local universe, there is evidence for anti-correlation between AGN fraction and galaxy density (e.g. Lopes et al. 2017), at least for luminous AGNs. Other studies have found comparable AGN fractions in clusters and fields for low-luminosity quasars (Haggard et al. 2010). However, at higher redshifts, the AGN evolution has been seen to follow a different

evolutionary path (Martini et al. 2013). Cosmic conditions, such as galaxy and cluster morphologies, presence of denser ICM, dominance of dark matter etc. at higher redshifts have greatly impacted the current state of the universe and large-scale matter distribution.

We look at one of the largest cluster samples to study the relative fraction of AGNs in cluster galaxies and fields. The aim of this paper is to investigate the AGN fraction in clusters relative to their field regions in the local universe (redshifts less than 0.5) using X-ray, optical, and mid-IR surveys. This is crucial to understand how the different local and global environmental factors found in clusters and low density fields may affect the AGN activity (by triggering or suppressing AGNs).

The paper is divided into the following sections: we describe the data and the photometric surveys used in Section 2. In Section 3, we describe the methodology used and in Section 4, we discuss the results. Finally, in Sections 5 and 6, we present the discussion and conclusions to our study respectively. We adopt the values for the cosmological parameters as follows:  $\Omega_m = 0.3$ ,  $\Omega_\Lambda = 0.7$ ,  $H_0 = 70 \text{ km s}^{-1} \text{ Mpc}^{-1}$ .

## 2.2 The Data

This study is based on 25801 galaxies in X-ray selected galaxy clusters and groups and 242972 field galaxies. This makes it one of the largest cluster catalogs used for studying the relative fraction of AGNs in high-density cluster environments against their surrounding low-density fields. In the following subsections, we describe the data.

### 2.2.1 Cluster Sample

The clusters studied in this paper are from the Meta-Catalog of X-ray selected galaxy clusters (MCXC), described in Piffaretti et al. (2011). It is partially based on the

*ROSAT* All-Sky Survey, abbreviated RASS hereafter. The majority of the RASS data was obtained by Position Sensitive Proportional Counter (PSPC) in the scanning mode with a count rate  $\geq 0.06$  counts/s. The catalog contains clusters from the surveys NORAS (Northern *ROSAT* All-Sky galaxy cluster survey) (Böhringer et al. 2000) and REFLEX (*ROSAT*-ESO Flux Limited X-ray Galaxy Cluster Survey) (Böhringer et al. 2004). REFLEX surveys the southern hemisphere at declinations below  $+2.5^\circ$  with a mean exposure of 335 s. It has a total coverage area of  $13924 \text{ deg}^2$ , which excludes the Galactic plane and Magellanic clouds. NORAS covers the northern sky above  $0.0^\circ$  declination and Galactic latitude  $\geq 20^\circ$ , with a mean exposure of 397 s. Additional data from the SGP survey covers a region of 1.013 steradian around the South Galactic Pole (Crudace et al. 2002). The other part of the catalog is taken from serendipitous cluster catalogs, such as WARPS (Perlman et al. 2002; Horner et al. 2008), EMSS (Gioia et al. 1990), 160SD (Mullis et al. 2003), 400SD (Burenin et al. 2007), and SHARC (Romer et al. 2000; Burke et al. 2003), that take observations of deeper pointed X-ray sources. There are five more contiguous RASS surveys and the five serendipitous surveys (mentioned above) used to create this catalog (Piffaretti et al. 2011).

The Meta-catalog of X-ray selected galaxy clusters provides the cluster redshift, standardized 0.1 – 2.4 keV band luminosity  $L_{X,500}$ , cluster mass  $M_{500}$ , and radius  $R_{500}$ , for 1743 clusters. The subscript 500 denotes the characteristic radius within which the mean density of the cluster is 500 times the critical density of the universe at the cluster redshift. The majority of MCXC cluster are at low to medium redshifts, with a redshift peak at  $z = 0.08$ . About half of the clusters (49%) have 0.1–2.4 keV band luminosities larger than  $10^{44} \text{ erg s}^{-1}$ , with a mean luminosity,  $L_{X,500} = 2.11 \times 10^{44} \text{ erg s}^{-1}$ . The cluster sample used in this study resembles a combination of multiple flux-limited samples where a large fraction of the clusters is derived from the RASS. Figure 2.1 shows the luminosity distribution with respect to cluster

redshift, where we can see the multiple flux limits. This distribution approximately contains clusters brighter than  $L_{X,500} = 10^{43} \text{ erg s}^{-1}$  at all redshift values. There are a handful of low luminosity clusters below this luminosity value for  $z < 0.1$ , and the same redshift bin has a deficit of the brightest clusters, at luminosities around  $L_{X,500} = 10 \times 10^{44} \text{ erg s}^{-1}$ , because of the lack of survey volume for the lowest redshift bin. However, as we see in Section 3.4, our mass-based classification of clusters (mass and luminosity are tightly correlated for clusters) does not show a significant difference in AGN fractions between the high- and low-mass categories in each redshift bin. Therefore, we argue that the flux-limited type of sampling from multiple surveys does not affect the AGN fraction results from this paper significantly.

The mean mass,  $M_{500}$  for these clusters is  $2.28 \times 10^{14} M_{\odot}$ . The catalog contains clusters ranging from galaxy groups to rich clusters with the mass range between  $0.96 \times 10^{12}$  to  $2.21 \times 10^{15} M_{\odot}$ . Detailed methodology to calculate X-ray luminosities ( $L_{X,500}$ ) and masses ( $M_{500}$ ) for the galaxy clusters, along with their uncertainties, can be found in Piffaretti et al. (2011). We have selected 580 X-ray selected galaxy clusters for this analysis that lie in the redshift range 0.0 and 0.5 and are a part of the SDSS footprint. The average X-ray luminosity for our sample of clusters in 0.1–2.4 keV band is  $1.77 \times 10^{44} \text{ erg s}^{-1}$  and the average mass is  $2.08 \times 10^{14} M_{\odot}$ . These are moderately rich clusters with a large fraction being galaxy groups and thus not well studied in literature.

## 2.2.2 SDSS and WISE Galaxy Catalogs

The galaxies were selected using the Sloan Digital Sky Survey data release 14 (SDSS DR14) (Abolfathi et al. 2018). SDSS is a multi-band imaging and spectroscopic survey that uses a 2.5m telescope with a survey area of 14555 square degrees. It uses five broad bands ( $u, g, r, i$ , and  $z$ ) where the average exposure time for each band is

53.9 s and the median redshift is 0.1 for the photometrically selected galaxies. This makes it a good catalog for the study of low redshift clusters. The median  $5\sigma$  depths for photometric images are 22.15, 23.13, 22.70, 22.20, and 20.71 mag for u, g, r, i, and z bands, respectively.

WISE (Wide-field Infrared Survey Explorer) is a multi-band, mid-IR all-sky survey that was launched on 2009 December 14 and completed its first complete sky coverage on 2010 July 17 (Wright et al. 2010). WISE has imaged in four passbands 3.4, 4.6, 12, and  $22\mu\text{m}$  (W1, W2, W3, and W4, respectively) with mean exposure times of 7.7 s (in W1 and W2 bands) and 8.8 s (in W3 and W4 bands). The  $5\sigma$  sensitivity in photometry is estimated to be 0.068, 0.098, 0.86, and 5.4 mJy at 3.4, 4.6, 12 and  $22\mu\text{m}$ , respectively. Saturation affects photometry for sources brighter than approximately 8.1, 6.7, 3.8, and  $-0.4$  mag at 3.4, 4.6, 12, and  $22\mu\text{m}$ , respectively.

## 2.3 Methodology

Cluster regions were defined to encompass the entire angular extent from the cluster center out to  $R_{500}$ . The typical  $R_{500}$  value for our clusters at these redshifts is about 2 Mpc and the angular size ranges from  $1'$  for the most distant clusters to  $58'$  for the nearby clusters. We then selected SDSS galaxies within the cluster region and made a redshift cut using the photometric redshift values available for the SDSS galaxy data within  $z_{cl}$  ( $1\pm 0.05$ ). For this study, we only select the galaxies in the absolute magnitude range  $-20.0$  to  $-22.0$ . This luminosity range is detectable for redshifts considered in our analysis  $z < 0.5$  given the SDSS  $r$  band limits of 22.2 mag. This range is chosen for all redshifts to avoid the selection bias toward low luminosity galaxies at low redshifts, and the range provides maximum number of galaxies for a statistical study of variation of AGN fraction with redshift. We bin the clusters with a 0.1 redshift bin, which is a factor of 2–3 of the mean uncertainties for photometric

redshifts from 0.03 for  $z < 0.3$  to 0.06 for  $z < 0.5$  (Abolfathi et al. 2018).

For each cluster, we uniquely defined a local field region,  $5 \times R_{500} - 10 \times R_{500}$  for comparison. Each SDSS galaxy in the dataset was identified uniquely with a single cluster or field region using SDSS photometric redshift (spectroscopic redshift was used where available) of the galaxy. This photometric redshift criterion will include foreground and background galaxies due to larger uncertainties in photometric  $z$  values. Therefore, we also investigate relative AGN fraction for more robust analysis. The galaxies in SDSS DR14 were then matched with sources from the WISE All Sky Survey with a matching radius of  $2''$  (e.g., Dai et al., 2015) to obtain the infrared colors. AGN fraction,  $f_A$  is defined as the ratio of the number of AGNs and total galaxies in the cluster.

While several color cuts have been proposed in literature to select mid-IR AGNs, our AGN sample was selected using the mid-IR color selection criterion described in Stern et al. (2012). Up to redshifts  $\sim 3.5$ , mid-IR AGNs have been observed to have mid-IR colors between W1 and W2 filters (W1–W2) (Stern et al. 2012), with a different color distribution than galaxies, because they have a distinct characteristic in the spectral energy distribution (Stern et al. 2005). Extinction from dust can cause extreme reddening in high redshift AGNs for optical and UV surveys and while AGNs selected in mid-IR are relatively insensitive to absorption, they need to contribute significantly to the total mid-IR luminosity to distinguish them from their host galaxy. Thus, identifying AGNs based on mid-IR colors is a robust method for heavily obscured, high-luminosity AGNs with  $z \leq 3.5$ . We impose a color cut of  $W1 - W2 > 0.8$  which is generally accepted to identify AGN dominated colors well. The optical and IR color-magnitude diagrams for the galaxies across all redshift intervals are shown in Figure 2.2. The right panel shows the mid-IR color magnitude plot for cluster and field AGNs and non-active galaxies. In the left panel of Figure 2.2, the optical colors are shown in SDSS-r and SDSS-i bands for a fraction of cluster and

field galaxies (AGNs and non-active galaxies). As can be seen, the majority of the cluster and field galaxies lie on the red sequence. The optical selection of cluster and field galaxies is biased toward red galaxies which have a more prominent  $4000\text{\AA}$  break allowing for more accurate determination of photometric redshifts. However, since this selection bias is seen in both cluster and field galaxies, the relative comparison of AGN fractions between cluster and field is not significantly affected. Hence, we perform a comparative study of AGN fractions for cluster and field environments.

## 2.4 Results

### 2.4.1 Dependence on environment

We separate the clusters in five redshift bins with a bin size of 0.1. We then calculate the AGN fractions in the clusters and fields in each redshift bin by adding all the data in the bin. In addition, we also split the cluster galaxies into two mass ranges and define those as low mass and high mass clusters. The mass cut was determined such that there were about the same number of cluster galaxies above and below the mass cut. The low mass cluster can be thought of as a group-like environment at that redshift, whereas the high mass cluster represents the more massive galaxy clusters. We define AGN fraction as the ratio of number of AGNs in a cluster (or field) to the total number of galaxies. The AGN fractions are listed in Table 4.1. The uncertainties associated with the AGN fractions are Poisson errors with  $1\sigma$  confidence limit. As discussed in section 3.3, the color cut used to select AGNs is generally reliable in selecting luminous mid-IR AGNs at low redshifts. Although our absolute AGN fractions for clusters and fields are affected by magnitude dependent AGN selection function, the relative AGN fraction between clusters and fields is a more robust quantity because it largely cancels out the selection function. In the left panel of Figure 2.3, we see that AGN fraction is lower in cluster galaxies than

that of field galaxies for each redshift bin. This result agrees with other studies in the literature that look at the environmental dependence of AGNs in clusters and fields (e.g., Lopes et al. 2017; Koulouridis et al. 2018). We infer that at low redshifts,  $z \leq 0.5$ , relatively more AGNs are found in low density field environment surrounding galaxy clusters compared to the regions closer to the core of the clusters.

The right panel of Figure 2.3 shows further classification into low and high mass objects where clusters (high-mass objects) have  $\log_{10}(M_{500}/M_{\odot}) > 14.3$  and groups (low mass objects) have  $\log_{10}(M_{500}/M_{\odot}) < 14.3$ . We choose the mass ranges to have comparable number of objects above and below the mass cut. AGN fractions for both mass ranges are very similar within the  $1\sigma$  uncertainties. The AGN fractions for group-like objects are slightly higher than cluster-like objects, except for  $0.1 \leq z \leq 0.2$  bin. Based on the result seen in left panel, we expect low mass objects to have fractions somewhere between high mass clusters and the fields, which we modestly observe, limited by the signal-to-noise ratio of the data. The salient feature we observe is a significantly higher AGN fraction in field than either low or high mass clusters which is the same environmental dependence as seen in the left panel of Figure 2.3.

## 2.4.2 Dependence on redshift

As described in Section 3.3, we divided the clusters into various redshift bins to study the fraction of AGNs as a function of redshift. First, we compared AGN fractions in cluster and field for each  $z$  interval, which is plotted in Figure 2.3, left panel. For our relatively low redshift range, it can be seen that the mean cluster AGN fraction increases as we go from  $z < 0.1$  to  $z < 0.5$ , however, the value flattens out for  $z > 0.4$  within  $1\sigma$  errors. A similar trend of AGN fraction with  $z$  is seen for field galaxies as well. The comparable  $f_A$  values within error bars for field galaxies for  $z < 0.4$



and  $z < 0.5$  could be a result of the significantly smaller samples of both cluster and field galaxies at higher redshifts. Similar trend has been found in previous studies, such as Martini et al. (2013) who studied AGN fraction at high redshift ( $z \sim 1-1.5$ ) and found an increase in X-ray AGN fraction from  $z = 0$  to  $z = 3.0$  for cluster and field AGNs. There is a 14.7 times increase in cluster AGN fraction from  $z < 0.1$  to  $z < 0.5$ . Similarly, for field region, AGN fraction increases 5.7 times from  $z < 0.1$  to  $z < 0.5$ . The percentage increase in cluster AGN fraction is higher than that in field AGN fraction. The right panel of Figure 2.3 shows the evolution of low and high mass cluster AGN fractions with redshift. For high mass clusters, there is a positive trend with  $z$  up to  $z = 0.3$  and then the values flatten out. For low mass objects, the dependence between AGN fraction and redshift follows a similar trend as high mass objects. However, the error bars are bigger for low mass objects. For field galaxies, the plot is the same as the left panel. In general, we observe an increasing AGN fraction with redshift as found in many studies done previously (e.g. Hasinger et al. 2005; Martini et al. 2013).

Figure 2.4 shows relative AGN fraction versus redshift. Relative fraction is more robust against selection effects, because they largely cancel out between field and cluster fractions. The correlation is determined using a best fit line and a positive slope of  $0.84 \pm 0.24$ , a  $3.5\sigma$  deviation from zero slope, which indicates that the relative AGN fraction also increases with redshift as is the case of absolute AGN fractions at  $z < 0.5$ .

### 2.4.3 Dependence on angular cluster-centric distance

We also investigated the dependence of AGN fraction on normalized radial offset from the center of the cluster for cluster and field galaxies. The distances are angular distances in  $R_{500}$ . In the left panel of Figure 2.5, AGN fraction is plotted as a

function of distance for cluster galaxies for the five redshift intervals. We see an increase in  $f_A$  from the core of the cluster out to  $R_{500}$  for all the intervals. The slopes and  $1\sigma$  uncertainties for the best-fit lines are  $0.016 \pm 0.004$ ,  $0.003 \pm 0.003$ ,  $0.053 \pm 0.011$ ,  $0.003 \pm 0.016$ , and  $0.060 \pm 0.021$  respectively. The dependence does not show a trend with increasing redshift. We see the slope decrease at first, then increase, then decrease again for  $0.3 < z < 0.4$ . The trend line is the steepest for the highest redshift bin. This suggests the cluster evolution may not be significant from  $z = 0.5$  clusters to present day clusters to observe an evolution in cluster-centric dependence of AGN fraction.

AGN fractions as a function of distance for field galaxies are in the right panel of Figure 2.5. As stated above, we define field galaxies as lying between  $5 \times R_{500}$  to  $10 \times R_{500}$ . There data is very scattered for field galaxies and the slopes are very close to 0 which indicates there is not a significant dependence on distance. We expect that the field fraction would not depend on the distance from the center of the cluster.

#### 2.4.4 Dependence on absolute magnitudes

We also investigate the dependence of AGN fraction on the  $M_r$ , absolute magnitude in the SDSS-r band. The absolute magnitudes for SDSS r-band were calculated using the distance modulus equation, with the K-correction terms for specific redshift values extracted from Assef et al. (2010) using the spectral energy distribution template for elliptical galaxies in clusters. The template is in the wavelength range from  $0.03 \mu\text{m}$  to  $30 \mu\text{m}$  and is based on the NOAO Deep-Wide Field Survey Bootes which has multi-wavelength photometric observations and also the AGN and Galaxy Evolution Survey which provides the spectroscopic data. This template is extended into the mid-IR (Assef et al. 2008) and is useful as we select the AGNs based on the mid-

IR color selection criteria mentioned in section 3.3. Our luminosity cut represents intermediate-luminosity AGNs ( $-22 < M_r < -20.0$ ). This luminosity cut was made to enable comparison of AGN fractions for lowest and highest redshift bins since the peak R-band luminosity shifts to lower absolute magnitudes for higher redshifts as only the most luminous AGNs would get selected at higher redshifts. Thus, analyzing  $f_A$  for a wider magnitude range would result in a biased sample of fewer faint magnitude, high  $z$  AGNs. Our magnitude range selects the majority of the AGNs in each redshift interval in our sample to avoid selection bias and therefore provides a more complete sample of cluster and field AGNs to calculate the AGN fraction. Because the selection functions cancel out between cluster and field AGN fractions, relative AGN fraction is a more robust measurement. Figure 2.6 shows AGN fraction as a function of R absolute magnitude for all the redshift bins. In the left panel, we have shown AGN fraction dependence on absolute magnitude for cluster and field galaxies. While a general trend of decreasing fraction is seen for field galaxies for  $0.1 < z < 0.5$ , it is not significant. For  $z < 0.1$ , the AGN fraction decreases and then becomes constant. The correlation for cluster galaxies is not conclusive. While AGN fraction seems to increase for the lowest  $z$  bin, it shows the opposite dependence for the next three bins. For  $z < 0.5$ ,  $f_A$  does not have a significant trend with absolute magnitude.

The right panel of Figure 2.6 shows the same relationship for relative AGN fraction. No obvious trend is seen with absolute SDSS r-band magnitude. Similar to the left panel, the relative AGN fraction increases with magnitude for  $0 < z < 0.1$ . It then decreases with absolute magnitude for next two  $z$  bins and flattens out for the highest redshift clusters in our sample. We expect a higher AGN fraction with increasing luminosity if we consider the absolute magnitude to be representative of cluster stellar mass. However, mid-IR selection criteria used in this study leads to a biased selection of AGNs as described in Stern et al. (2012) which selects WISE

AGN candidates that peak around SDSS  $r \approx 20.0$ . Very few AGN candidates selected are brighter than  $\sim 19$ th mag in SDSS r-band (Stern et al. 2012). This selection bias would explain the scattered distribution of AGN fraction relative to R absolute magnitude.

## 2.5 Discussion

We discuss some of the selection biases and the robustness of our results. For the mid-IR color selection of AGNs, we report the results for the selection we use,  $W1-W2 > 0.8$ . However, we also selected different color cuts above and below  $W1-W2 = 0.8$  and found that while absolute AGN fraction values changed, the trends seen with various cluster and galaxy properties and relative fractions are robust against the color selection criterion. The field fractions are higher than cluster fractions at all redshifts. The optical selection of cluster and field galaxies is biased toward red galaxies as described in section 3.3. However, comparing cluster AGN fraction against field fraction makes this bias unimportant as we are selecting more red galaxies in both cluster and field.

As discussed in section 3.4, our results show that AGN fraction in clusters is lower than that in fields at all redshifts considered in this study. This is in agreement with several AGN fraction studies in massive clusters done previously (e.g. Kauffmann et al. 2004; Lopes et al. 2017). This indicates cold gas inflow toward the center where the black hole is located is more efficient for isolated galaxies situated in fields, via secular processes and/or mergers. The role of mergers in being the dominant triggering mechanism for AGN activity has been debated for a long time. If low- $z$  AGNs are turned on predominantly from the inflow of gas during major galaxy interaction and merger events (e.g. Sanders et al. 1988), it would be expected that high velocity dispersions in moderate to rich clusters would decrease

the efficiency of these mergers resulting in a lower fraction of active galactic nuclei found in inner regions of clusters. Semi-analytical modeling of dynamically young, evolving galaxy groups formed by mergers of smaller galaxy systems is shown to have higher black hole accretion rate than old, relaxed galaxy groups formed from major mergers at higher  $z$  (Raouf et al. 2014; Raouf et al. 2019), leading to more efficient AGN activity and thus, higher AGN fractions. This points toward a reduced merger efficiency in the richest galaxy conglomerations. Outer regions of clusters and low density fields in the immediate vicinity of the clusters are seen to have higher fraction of AGNs at low redshifts, attributed to more efficient mergers while AGN activity is strongly suppressed in the inner regions of rich clusters (e.g. Koulouridis, & Plionis 2010; Koulouridis et al. 2018). We find a significant difference between cluster and field AGN fractions for both the cases, when we divide our clusters based on mass and when we do not, which is clearly indicative of an environmental dependence for these intermediate-mass clusters. Our conclusions are also supported by Constantin et al. (2008) who found an anti-correlation between AGN activity and local density for moderately bright galaxies ( $M_r \approx -20$ ) similar to the galaxies used in our study. Many theoretical studies that model galaxy interactions have found a close association between galaxy mergers and accretion of cold gas onto the supermassive black hole, thus triggering AGN activity (e.g. Di Matteo et al. 2003; Di Matteo et al. 2005; Croton et al. 2006). Role of mergers and hence the environment of these AGNs is also very heavily dependent on AGN selection criteria (Koulouridis et al. 2016; Goulding et al. 2018), luminosity of the galaxy sample (Melnyk et al. 2018; Chiang et al. 2019), and redshift (Martini et al. 2009; Shirasaki et al. 2018). Many studies that show no correlation between AGN activity and environment are done at high  $z$  and typically use X-ray AGNs (e.g. Silverman et al. 2009; Villforth et al. 2017). Our results agree with the recent study done by Ellison et al. (2019) which looks at the role of interactions in triggering mid-IR selected AGNs in the local uni-

verse by studying morphological disturbances in these galaxies. They find that in 59% of mid-IR AGNs, the morphology indicates interaction undergone by the galaxy and conclude that mergers seem to play a dominant role in fueling the active galactic nuclei. In their study, Ellison et al. (2019) find different results for merger-driven triggering for optical AGNs versus mid-IR selected AGNs indicating selection bias in looking at the environment dependence on the triggering of active galaxies between various studies done in the literature. Ram pressure stripping would also play an important role in stripping galaxies of their gas, especially close to the cores of these clusters (Gunn, & Gott 1972; Ebeling et al. 2014). Pressure from the hot gas in the intracluster medium drives the gas out of the galaxy, including the denser cold gas which feeds the central engine.

Our result for group and cluster classification based on  $M_{500}$  shows comparable AGN fractions for the two mass classes. We expect low mass galaxy groups to have an environment and properties, such as stellar mass density similar to the outskirts of massive clusters. For the local universe, we expect groups to have higher AGN fraction than rich galaxy clusters due to an enhancement in triggering opportunities, especially because of lower relative velocities of galaxies in groups. We find slightly higher values for group-like objects, however, within the error bars, the difference is not significant (see Figure 2.4, left panel). Most clusters selected from the MCXC catalog are intermediate-mass to rich clusters. Therefore, the low-mass groups we have selected ( $\log_{10}(M_{500}/M_{\odot}) < 14.3$ ) are still relatively massive objects and we conclude that our calculated AGN fraction for the low-mass category may not be truly representative of small galaxy groups. For example, Lopes et al. (2017) find significantly higher AGN fraction for high mass systems than low mass systems. However, it should be noted that the mass cut they use is  $\log_{10}(M_{*}/M_{\odot}) > 10.6$ , which is much lower than our cluster mass range. Many studies support the broad idea that the population of active galaxies found in galaxy clusters and groups and

low tidal density field regions reduces from early universe ( $z \sim 1 - 2$ ) to present day. AGN fraction evolution with redshift shows a positive dependence as seen in Figures 2.3 and 2.4. Our results support this theory as we see an increase in mean cluster and field  $f_A$  from  $z = 0.1$  to  $z = 0.5$ . We infer our comparable  $f_A$  values for  $z = 0.4$  and  $z = 0.5$  within error bars are a result of larger uncertainties in photometric redshifts and a smaller sample of high  $z$  clusters and member galaxies. Several factors, such as reduced efficiency of massive mergers due to high relative velocities of member galaxies in clusters (Makino, & Hut 1997; Alonso et al. 2007), smaller fraction of gas-rich galaxies (Martini et al. 2013), and ram pressure stripping (see Poggianti et al. 2017; Marshall et al. 2018), affect the availability of cold gas that fuels the accreting black hole in the local universe. Hydrodynamical and N-body simulations suggest an increase in merger rate with redshift for field galaxies (Rodriguez-Gomez et al. 2015) which agrees with our result of higher AGN fraction in field at higher redshifts. At high redshifts, protoclusters provide a dense galaxy-rich environment which increases the probability of mergers in galaxies rich in gas aiding in fueling the central black holes and turning on the nuclear activity. This indicates a scenario for changing mechanisms for nuclear activity triggering over cosmic time where there is a transition from high-luminosity mergers dominant out to  $z \sim 1.5$  to more secular processes, such as minor mergers, tidal effects, playing a more significant role in the local universe (Martini et al. 2009). Our findings for enhanced cluster (high-mass) and group (low-mass) AGN fractions at higher  $z$  values is consistent with previous studies done in the literature that have found mergers of luminous, red galaxies in galaxy clusters and groups up to  $z \sim 1$  and lower merger fractions in low redshift clusters (e.g. Couch et al. 1998; Tran et al. 2005). By present day, cluster galaxies are believed to have been depleted of a significant amount of their cold gas relative to field galaxies, resulting in a smaller relative fraction of these active galaxies. Higher number of AGNs relative to total galaxies have been found at high redshifts (e.g.

Eastman et al. 2007; Haggard et al. 2010; Martini et al. 2013).

Studies have also found AGN fractions to vary with clustercentric distance (Ehlert et al. 2014; Koulouridis, & Bartalucci 2019). Our result for AGN fraction dependence on clustercentric distance shows a higher rate of AGN occurrence from as we go from cluster core to the outer regions of the cluster ( $R \sim R_{500}$ ) for all the redshift bins between 0.0 – 0.5. This increase in AGN fraction suggests the presence of different physical conditions in the cluster core and outskirts and might be indicative of more efficient AGN quenching processes, such as ram pressure stripping, and fewer mergers near the cluster potential where majority of the red and dead ellipticals with high velocity dispersions reside. This result is in agreement with the increasing density of X-ray AGNs from  $0 < R/R_{500} < 1$  found by Koulouridis, & Bartalucci (2019) in massive ( $M_{500} > 10^{14} M_{\odot}$ ), high redshift ( $z \sim 1$ ) clusters. However, variation of AGN density with distance from the cluster center and in the outskirts has also been found to depend on mass range of the sample. For example, Gordon et al. (2018) look at the distribution of AGN in the infall region of the cluster projected phase space compared to cluster core and find that in high-mass groups ( $\log_{10}(M_{200}/M_{\odot}) > 13.5$ ), AGN prefer the infalling galaxy population whereas for low-mass groups, they do not find any difference in AGN fraction between core and infall region. To better understand the environment dependence of AGN fraction in galaxy groups versus large clusters, we will need a sample of low-mass galaxy groups to perform the same analysis. The lack of redshift evolution of this trend might indicate that the cluster evolution from  $z = 0.5$  to  $z = 0$  does not affect the rate of AGNs inside the cluster. However, it should be noted that the larger errors in galaxy members' redshifts may result in a bias at high  $z$ .

We obtain inconclusive results for the relation between AGN fraction and SDSS r-band absolute magnitudes for cluster galaxies. The field AGN fraction decreases with increasing absolute R magnitude in SDSS bands. For  $0.0 < z < 0.1$ , the AGN



fraction peaks at  $M_r \sim -20.0$  for field galaxies and levels out for galaxies brighter than  $M_r \sim -21.0$ . Whereas for the remaining four  $z$  intervals,  $0.1 < z < 0.5$ , there is a steady decline in AGN fraction from  $M_r = -20.0$  to  $M_r = -22.0$ . This contradicts the result found in Haggard et al. (2010) where they compared field X-ray AGN fractions in absolute i-band magnitude bins and found higher AGN fraction for  $-22 < M_i < -21$  than for  $-21 < M_i < -20$ . This might be due to selection bias in our mid-IR selected AGNs in the field where very few of the WISE-selected AGNs are brighter than SDSS-i  $\sim 19$ . We only select a small range of absolute magnitudes to study intermediate luminosity AGNs to keep it consistent over all the redshift bins and find no significant trend for cluster active galaxies or the relative AGN fraction. Larger sample of AGNs over a wider luminosity range would be needed to understand if luminosity dependence of AGN fraction is a function of luminosity class.

## 2.6 Conclusions

We have presented a study of the fraction of active galaxies in clusters and fields in an attempt to understand the still-debated environmental dependence of nuclear activity in AGNs. We have calculated the fraction of AGNs in clusters and fields in five redshift intervals between redshifts 0.0 to 0.5. For each redshift bin, we find that the field AGN fraction is significantly higher than the cluster AGN fraction. This result is in agreement with several studies done in the literature where low density (field) regions were found to have higher AGN fraction than their overdense counterparts at low to intermediate redshifts. It suggests that fields provide an ideal environment for facilitating gas inflows during mergers because of the relatively lower velocity dispersions in galaxies, triggering nuclear activity in AGNs more efficiently than the dense clusters. As we go from low to high redshifts, the relative fraction of AGNs seems to flatten out. AGN fraction has previously been found to increase

with redshift which indicates a significant depletion in the availability of cold gas in clusters and fields in present universe compared to the scenario at high redshifts ( $z \sim 1 - 1.5$ ). The comparable AGN fraction values for  $z = 0.4$  and  $z = 0.5$  could be because of higher uncertainty due to much smaller sample of galaxies compared to lower redshift galaxies. We also find a strong dependence of cluster AGN fraction on clustercentric distance which might be indicative of the differences in galaxy evolution due to different physical conditions present in the cluster core and outskirts, further reinforcing the environmental dependence of AGN activities. The field AGN fraction is almost constant with distance from the cluster center, showing that we have selected field regions sufficiently away from the clusters. The dependence of AGN fraction on  $R$  absolute magnitude is not conclusive and we attribute mid-IR selection bias to be a reason due to the selection of relatively brighter AGN candidates. In future, we plan to increase our sample size with spectroscopic data and low-mass X-ray selected clusters to improve the statistical significance of our results to better understand the environmental dependence of AGN fraction.

## 2.7 Acknowledgements

This chapter is reproduced with permission from AAS from the following publication: Mishra, H. D. and Dai, X. 2020, AJ, 159, 69, “Lower AGN Abundance in Galaxy Clusters at  $z < 0.5$ ”, accepted in the Astronomical Journal.

We are grateful to the anonymous referee for the helpful comments and recommendations that made the paper clearer and stronger. We acknowledge the financial support from the NASA ADAP programs NNX15AF04G, NNX17AF26G, NSF grant AST-1413056.

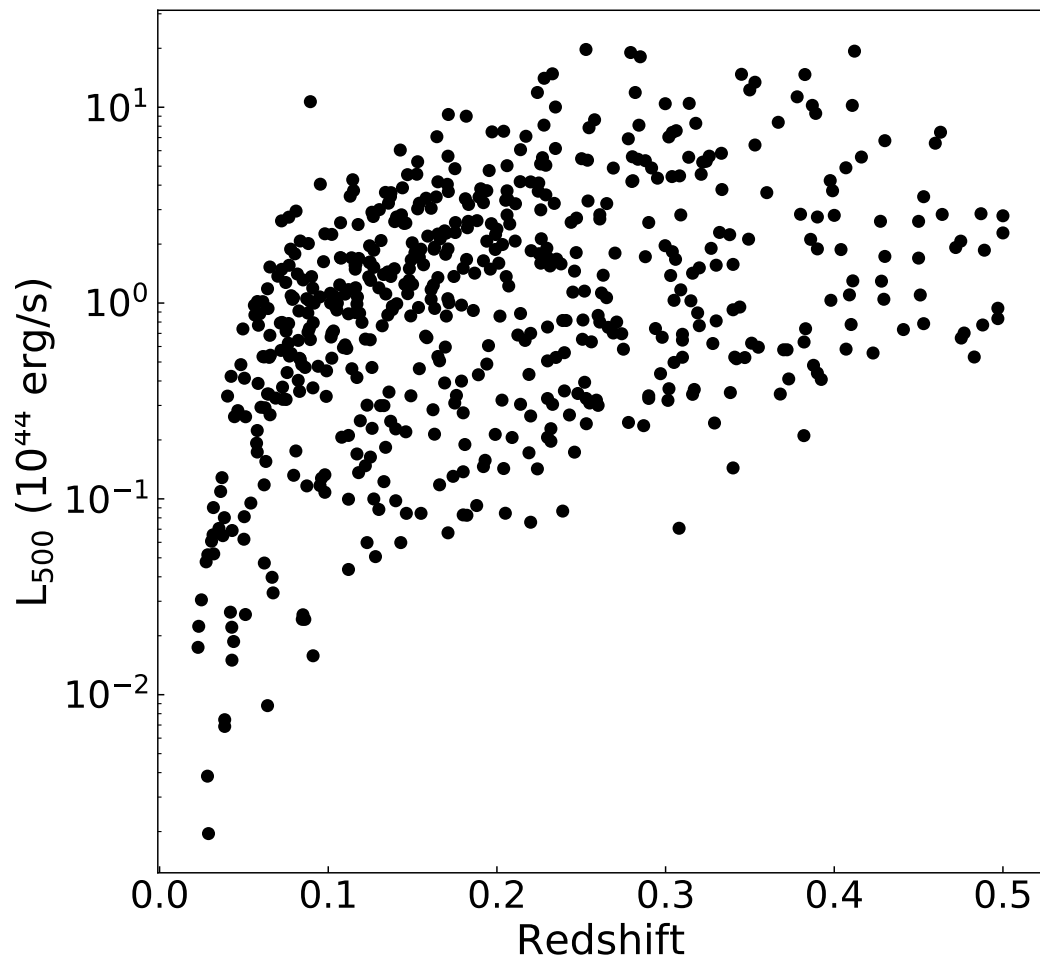


Fig. 2.1.— Luminosity ( $L_{500}$ ) versus redshift of the X-ray clusters used in this study.

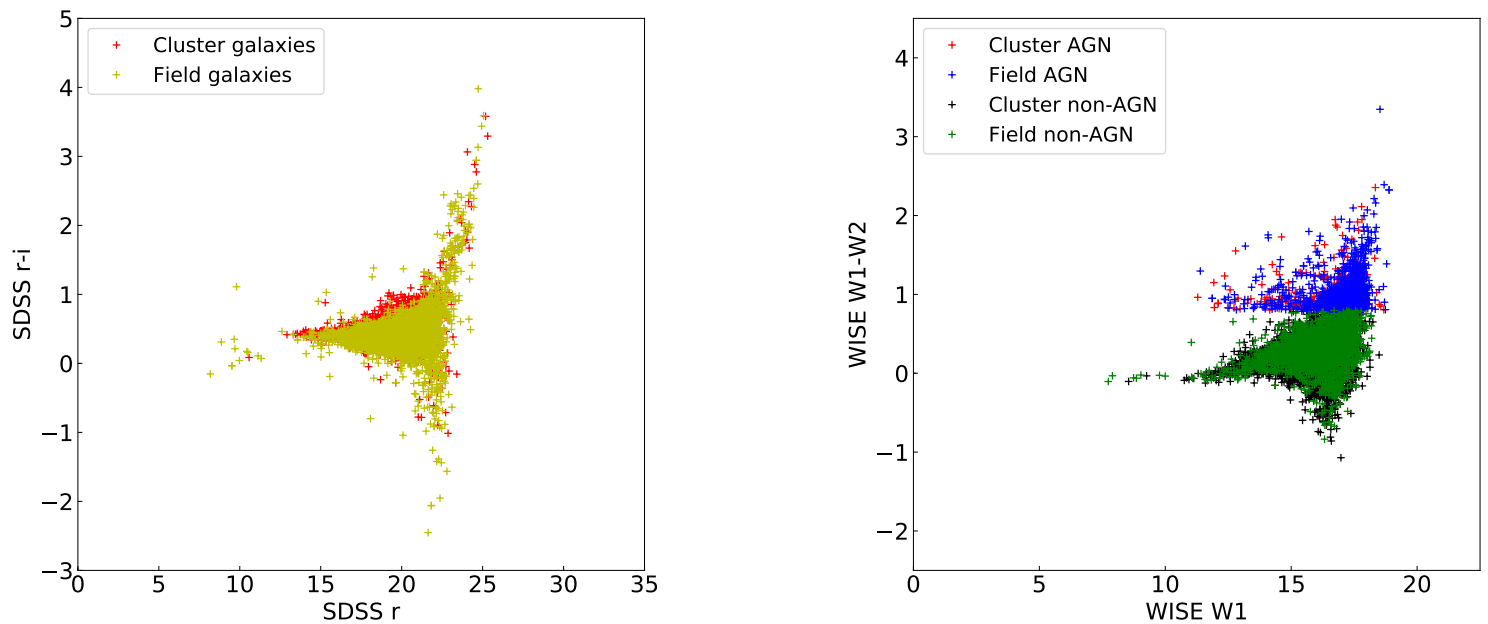


Fig. 2.2.— Color-magnitude diagrams for our galaxy sample for redshift range 0.0–0.5. Left panel: Optical color-magnitude diagram in SDSS  $r$  and  $i$  bands for all cluster galaxies (red) and all field galaxies (yellow). Right panel: Mid-IR color-magnitude diagram using WISE  $W1$  and  $W2$  magnitudes for cluster AGNs (in red), field AGNs (in blue), cluster non-active galaxies (in black), and field non-active galaxies (in green).

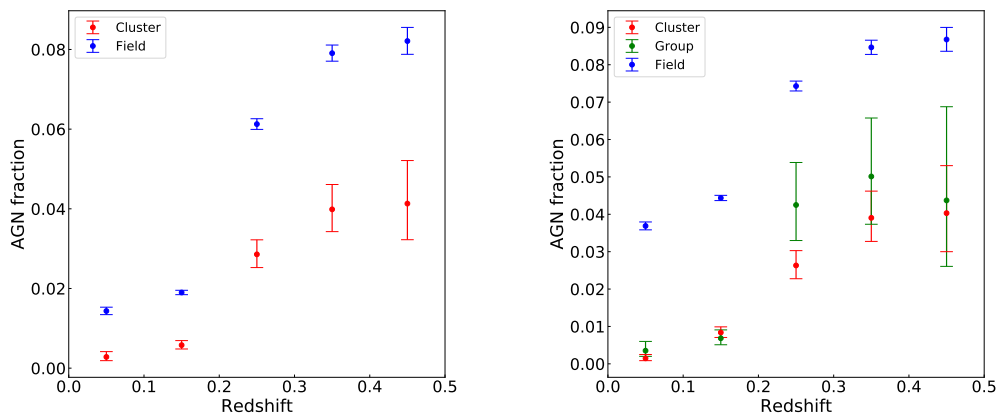


Fig. 2.3.— Fraction of AGNs in high and low density environments as a function of redshift. Left panel: AGN fraction for redshift bins from  $z=0.0$  to  $z=0.5$ , with bin size=0.1 for cluster and field objects. The errors are Poisson errors that correspond to  $1\sigma$  confidence limits. Right panel: Same as the left panel, but we divide cluster galaxies into low mass objects (green circles) and high mass objects (red circles). The blue circles are field galaxies in both panels.

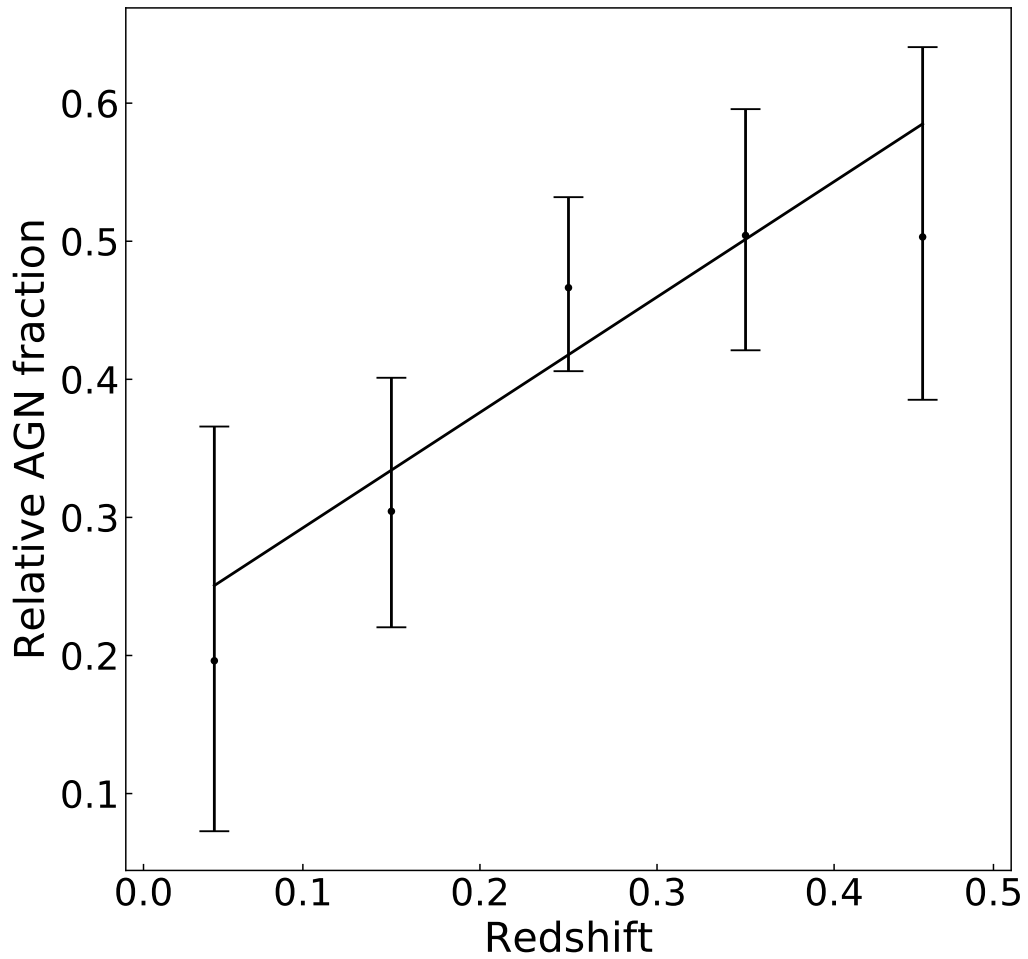


Fig. 2.4.— Relative AGN fraction for cluster and field galaxies as a function of redshift. The errors are Poisson errors that correspond to  $1\sigma$  confidence limits. The best-fit line has a slope of  $0.84 \pm 0.24$ .

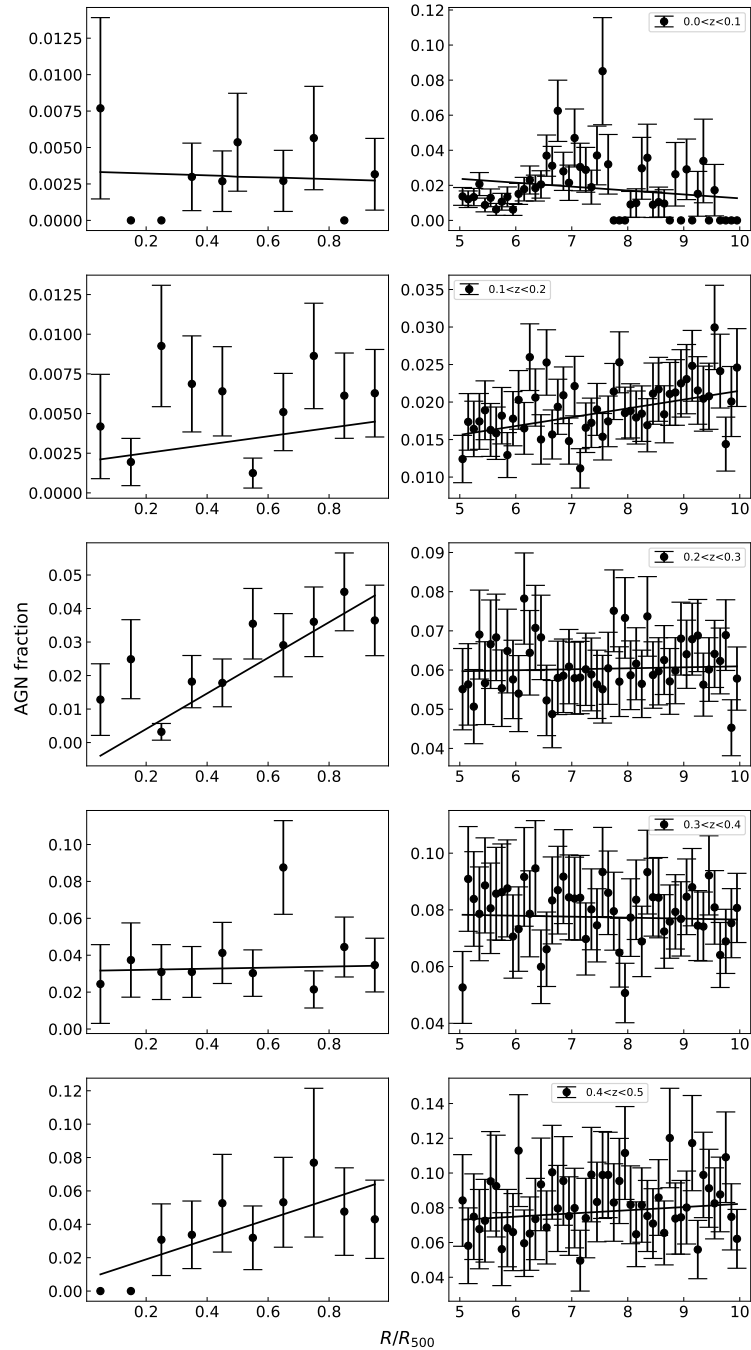


Fig. 2.5.— Fraction of AGNs as a function of angular clustercentric distance (in terms of  $R_{500}$ ). Left panel:  $f_A$  for cluster galaxies for the five  $z$  bins. Right panel: Same as the left panel, but for field galaxies. The errors are Poisson errors that correspond to  $1\sigma$  confidence limits.

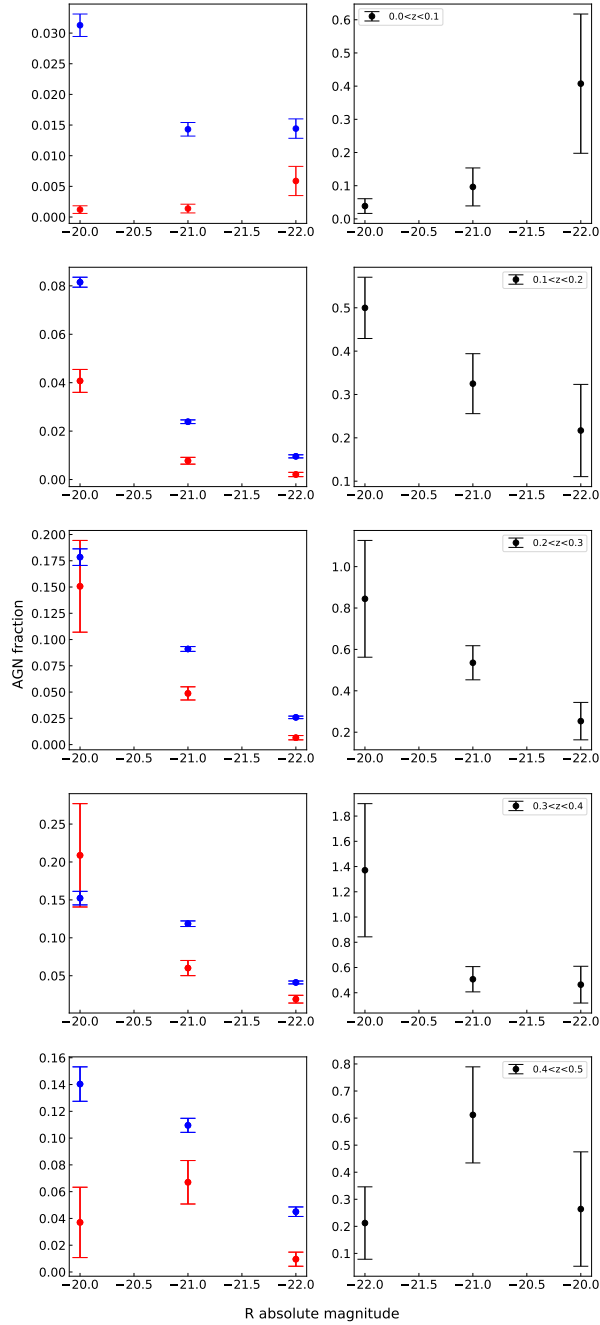


Fig. 2.6.— Fraction of AGNs as a function of R absolute magnitude. Left panel:  $f_A$  for cluster (red) and field (blue) galaxies for the five  $z$  bins. Right panel: Same as the left panel, but for relative AGN fractions. The errors are Poisson errors that correspond to  $1\sigma$  confidence limits.



Table 2.1. AGN fraction in clusters and fields for the five redshift bins

Redshift <sup>a</sup>	Cluster	Field	Low mass cluster	High mass cluster
$0.0 \leq z \leq 0.1$	$0.0028^{+0.0013}_{-0.0009}$	$0.0143^{+0.0009}_{-0.0009}$	$0.0015^{+0.0010}_{-0.0006}$	$0.0035^{+0.0024}_{-0.0015}$
$0.1 \leq z \leq 0.2$	$0.0058^{+0.0011}_{-0.0009}$	$0.0190^{+0.0005}_{-0.0005}$	$0.0084^{+0.0015}_{-0.0013}$	$0.0068^{+0.0022}_{-0.0017}$
$0.2 \leq z < 0.3$	$0.0286^{+0.0036}_{-0.0033}$	$0.0745^{+0.0013}_{-0.0013}$	$0.0263^{+0.0039}_{-0.0035}$	$0.0425^{+0.0113}_{-0.0095}$
$0.3 \leq z < 0.4$	$0.0399^{+0.0062}_{-0.0055}$	$0.0791^{+0.0020}_{-0.0020}$	$0.0390^{+0.0071}_{-0.0063}$	$0.0501^{+0.0156}_{-0.0127}$
$0.4 \leq z < 0.5$	$0.0413^{+0.0108}_{-0.0090}$	$0.0821^{+0.0034}_{-0.0033}$	$0.0403^{+0.0127}_{-0.0103}$	$0.0437^{+0.0250}_{-0.0176}$

<sup>a</sup>All the data for cluster and field in each  $z$  bin is added

## Chapter 3

# Active Galactic Nuclei Abundance in Cosmic Voids

### 3.1 Introduction

Galaxies are found in different large-scales structures that form the cosmic web of the Universe: the overdense regions called galaxy clusters which expand out into filamentary structures, which in turn form boundaries of vast underdense regions, known as the cosmic voids (Bond et al. 1996; Pan et al. 2012), mostly devoid of matter (dark matter and baryons). Voids have a radius of tens of Mpc to over one hundred and constitute the majority of the universe's volume (e.g. Zeldovich et al. 1982; Pisani et al. 2019). They contain few, isolated galaxies and not much gas. Due to their underdense nature, void properties are dominated by unclustered components, such as dark energy. In voids, there is a spherical outward motion of matter toward the walls and filaments (e.g. Hamaus et al. 2016).

Most, if not all, galaxies have a supermassive blackhole (SMBH) at their center. Of these, a fraction of galaxies are active where their central engine is accreting mass from the dense central region of the galaxy at a sufficiently high rate. It is not well understood why only a few SMBHs show such high nuclear activity. There is strong evidence that galaxy evolution is closely related to its environment, influencing its star formation, morphology etc. (e.g. Marconi & Hunt 2003; Einasto et al. 2008; Alberts et al. 2016 ). Possible triggering mechanism(s), such as major and minor mergers (e.g. Di Matteo et al. 2005; Fontanot et al. 2015), tidal effects (Moore et al. 1996), disc instability (Dekel et al. 2009), may be significant in driving AGN activity by supplying cold gas to the central black hole, thus triggering it. In the AGN phase

model, where most black holes in galaxies undergo an intense activity period, the lifetimes of emission at AGN luminosities are estimated to be in the range  $10^6 - 10^8$  years. Based on the models of black hole growth via gas inflows, the strong accretion phase lasts for  $\sim 10^8$  years (Kauffmann, & Haehnelt 2000; Hopkins et al. 2005; Shankar et al. 2009). Understanding galaxy evolution requires the study of complex external and internal processes, such as mergers, gas stripping, disc instability, that might have strong influence on its evolution and AGN activity.

The role of the galaxy's environment in AGN triggering is widely debated. In galaxy clusters and filaments, a combination of factors, such as galaxy rich environment which leads to more galaxy interactions and mergers, extreme conditions in the cluster's gravitational potential well, concentration of cold gas in the cluster halo, and Ram-pressure stripping from the ICM, determines AGN activity (Gunn, & Gott 1972; Larson et al. 1980; Di Matteo et al. 2005). Many studies such as Ellison et al. (2019) and Mishra & Dai (2020) find evidence for variation in fraction of AGN with high and low-density environments, while several others see no to very weak correlation between the two (e.g. Miller et al. 2003; Pimblet et al. 2013; Man et al. 2019). The influence of environmental factors on AGN fraction is tied to the evolution of galaxies and clusters over cosmic time. Several studies show that cluster environments have been dynamically evolving over the history of the universe and that has strong influence on AGN fractions in both clusters and fields (Eastman et al. 2007; Bufanda et al. 2017). In the local universe, there is found to be evidence for anti-correlation between the AGN fraction and galaxy density (e.g. Lopes et al. 2017; Mishra & Dai 2020). Other studies have found comparable AGN fractions in clusters and fields for low-luminosity quasars (Haggard et al. 2010). However, at higher redshifts, the AGN evolution is seen to follow a different evolutionary path (Martini et al. 2013). Cosmic conditions at higher redshifts, such as galaxy and cluster morphologies, presence of denser ICM, dominance of dark matter, have greatly

impacted the large-scale matter distribution. Studies show that the clusters have undergone significant evolution over the history of the universe which has influenced AGN abundance (e.g. Eastman et al. 2007; Bufanda et al. 2017; Mishra & Dai 2020).

In contrast to clusters, void dynamics have remained largely unchanged. In void environment, galaxy evolution is more likely to be dominated by secular (in-situ) processes, because mergers and gas stripping don't occur as much due to the very low galaxy density (Porqueres et al. 2018; Habouzit et al. 2020). This would imply less evolved galaxies are contained in the voids, which must have formed at later times and followed different evolutionary path from cluster and group galaxies. Thus, voids form an ideal environment to investigate galaxy evolution and its dependence on secular processes in the absence of external processes, like mergers, which dominate in the high-density environments. Studies have shown that voids comprise of fainter, bluer galaxies, with higher star formation rates, than their overdense counterparts (e.g. Hoyle et al. 2005; Goldberg et al. 2005; Bruton et al. 2020). Previous works investigating AGN abundance and accretion activity in voids have also found mixed results that depend on host properties. For example, Constantin et al. (2008) found that AGN are more common in voids than walls for moderately luminous and massive galaxies ( $M_r \sim -20$ ,  $\log M/M_\odot < 10.5$ ), but the AGN abundance is comparable for brighter hosts ( $M_r < -20$ ). Kauffmann et al. (2003) find a decreasing fraction of strong AGN in massive galaxies as a function of density, which provides evidence for an environmental dependence.

Compared to the rich literature available for studying AGN activity in galaxy clusters, groups, and fields, there have not been many studies that have looked at the AGN abundance and AGN evolution in cosmic voids. Our motivation behind this study is to investigate the presence of environmental influence, if any, on the triggering of the supermassive black hole in the absence of “nurture” processes, and contribute to the understanding of AGN in the most underdense regions of the uni-

verse. We look at one of the largest spectroscopic void samples to study the fraction of optical AGN in voids. This is crucial to understand how the different local and global environmental processes found in baryon-devoid voids may trigger or suppress AGN activity.

## 3.2 Data and Methodology

We investigate AGN fraction using 1,228 cosmic voids, 166,067 member galaxies (non-AGN) and 3,100 AGN in the voids. In the following subsections, we describe the data and the method. Based on the dataset used in this study, the analysis of this paper is limited to investigate the AGN fraction at the luminous end ( $M_r \leq -22$ ) in inner and outer regions of voids in the local-intermediate universe ( $0.2 < z < 0.7$ ).

### 3.2.1 Galaxy Catalogs

The galaxies were selected from the Baryon Oscillation Spectroscopic Survey (BOSS; Dawson et al. 2013) which is part of the Sloan Digital Sky Survey III (SDSS III; Eisenstein et al. 2011). SDSS is a multi-band imaging and spectroscopic survey that uses a 2.5m telescope with a survey area of 14555 square degrees. BOSS spectrographs were used for the spectroscopic survey to measure the redshifts of 1.5 million luminous red galaxies and Lyman-alpha absorption towards 160,000 high- $z$  quasars.

The galaxy data comes from the Data Release 12 (DR12; Alam et al. 2015). The data has been divided into two redshift ranges, LOWZ, which covers  $0.0 < z < 0.4$ , and CMASS, which is in the interval  $0.4 < z < 0.7$ . LOWZ and CMASS samples are further divided into LOWZ/CMASS North and LOWZ/CMASS South. The catalogs provide data on the coordinates, spectroscopic redshift, different fluxes, as well as several other parameters (Reid et al. 2016).

### 3.2.2 Quasar Catalog

We use the SDSS-DR 12 quasar catalog in order to have the same coverage for galaxies and AGN. The catalog is described in its entirety in Pâris et al. (2017) and contains the object's coordinates, redshifts obtained using different methods, the photometric SDSS magnitudes in u-, g-, r-, i-, and z-bands and their associated errors, and the absolute i-band magnitude. The spectroscopic redshifts are crucial to accurately measure the quasar-void distances. AGN selection methods relying on photometric properties, such as MIR, and matching with galaxy positions do not work well for our study of underdense regions because of the large distance uncertainties and small sample statistics.

### 3.2.3 The Void Sample

The voids used for this study are from the catalog of cosmic voids based on SDSS III Data Release 12, described in Mao et al. (2017). The voids are based on galaxies from the large-scale structure (LSS) catalogs, which are a part of the BOSS database. Mao et al. (2017) use ZOBOV (Neyrinck 2008), which is an algorithm based on Voronoi tessellations and the watershed method (Platen et al. 2007) to detect voids. Since voids are irregular in shape, each void has been assigned a center and an effective Voronoi radius which is the equivalent radius it would have if the volume of the underdense region was spherically symmetric.

The cosmic voids catalog from Mao et al. (2017) provides the redshift of the weighted center of the void, the number of galaxies in the void, the total Voronoi volume, the effective void radius, the number density of the minimum density Voronoi cell in the void, the density contrast of the minimum density cell comparing to the mean density at that redshift, the ratio of the minimum density particle on a ridge to the minimum density particle of the void, the probability of the void origin as

Poisson fluctuations, and the distance between the weighted void center and the nearest survey boundary (Mao et al., 2017). The LOWZ voids are in the range  $0.2 < z < 0.43$ , whereas the CMASS voids cover the range  $0.43 < z < 0.7$ . The majority of the voids have effective radii ranging from 30–80  $h^{-1}$  Mpc (see Figure 2 in Mao et al. (2017) for the void size distribution), where the LOWZ sample exhibits an extra tail distribution on the larger size compared to CMASS. Figure 3.1 shows the redshift distribution for the cosmic voids sample used in this study for the LOWZ (low redshift) and CMASS (high redshift) samples.

### 3.2.4 Methodology

In this study, the size of the voids was characterized by the effective radius,  $R_{eff}$ , which lies in the range 30–80  $h^{-1}$  Mpc. Although individual voids can deviate from a sphere, Mao et al. 2017 found that stacking analyses using  $R_{eff}$  provide stable and average void properties, such as the galaxy density. The voids are divided into five redshift intervals: 0.21 – 0.28, 0.28 – 0.35, 0.35 – 0.42, 0.42 – 0.56, and 0.56 – 0.70, to study any evolutionary trend with redshift, if present. Member galaxies and AGN for the voids were selected from the SDSS CMASS and LOWZ galaxy catalogs and the quasar catalog. To select void members, physical distances in the three-dimensional space are calculated between the void center and the galaxy center. We utilize the spectroscopic redshifts available for the voids and galaxies in the BOSS catalogs for more accurate distances. To classify the galaxies and AGN as members, we use a simple method based on the proximity of a galaxy to its nearest void center given by the physical distance between the galaxy and the void center. To investigate the differences in physical conditions in the inner and outer regions of the voids and see if environmental factors play a role in AGN abundance closer to the void center versus farther away, we assign each member galaxy to either the inner or outer

region of the void. The criterion chosen for the inner and outer regions is based on the distance of a galaxy to the void center. The inner and outer void regions are defined to lie between  $0.0 - 0.6 R_{eff}$  and  $0.6 - 1.3 R_{eff}$  respectively, and their sizes vary with the effective radius of a void. This approach of assigning void membership to galaxies and defining inner and outer regions does not take into account the shape of the individual voids; however, for the purpose of a statistical study, the voids in each redshift bin are stacked and the effective shape of the resultant void is a sphere. For this study, we make an absolute magnitude cut in each redshift bin to select luminous galaxies, where the absolute magnitudes are calculated using the K-correction templates of Assef et al. (2010). The range used for the magnitude selection is absolute-r magnitude =  $-23$  to  $-22$  to focus on the luminous galaxies and is chosen to avoid the selection bias toward low luminosity galaxies at low redshifts. This provides the maximum number of galaxies for a statistical study of bright AGN and galaxies for all redshift bins. The fraction of AGN (or quasar fraction specific to this analysis),  $f_A$ , is defined as the ratio of the number of active galaxies and the total number of galaxies in the void.

### 3.3 Results

We separate the voids in five redshift bins and calculate the AGN fractions in the inner and outer void regions in each redshift bin by stacking the voids in the bin. The AGN fractions for the inner and outer void regions for each redshift range are listed in Table 4.1, which also provides the raw galaxy counts for AGN and non-AGN in the voids. The uncertainties associated with  $f_A$  are Poisson errors with  $1\sigma$  confidence limit. Figure 3.2 shows the fraction of AGN in inner and outer void regions for each redshift bin. Our goal is to independently investigate the low redshift range (the LOWZ sample) and higher redshift range (the CMASS sample). At low redshifts,



$z \leq 0.42$ , we do not see a significant difference in the AGN abundance in the inner and outer regions of the void. However, for the two highest redshift bins,  $0.42 < z < 0.56$  and  $0.56 < z < 0.72$ , the AGN fraction in the inner void region is significantly higher than for the outer void region. The differences in the AGN fractions between the inner and outer regions for the highest two  $z$  bins are  $0.0152 \pm 0.0049$  and  $0.0192 \pm 0.0053$ , at  $3.1\sigma$  and  $3.6\sigma$  significances, respectively. Considering that we have five independent tests for the five redshift bins, the significance of the deviation between  $f_A$  values are  $2.6\sigma$  and  $3.1\sigma$  sigma, respectively for these two redshift bins. The average AGN fraction across all redshifts for the inner void region is  $0.028 \pm 0.004$ , which is 1.3 times higher than that for the outer void region, where the average fraction is  $0.021 \pm 0.001$ .

We further divide the inner and outer regions into smaller bins to investigate the dependence of AGN fraction on the distance from the center of the cosmic voids. The distances are measured in  $R_{eff}$  and range from the void center to  $1.3 R_{eff}$ . The size of the radial bins is fixed at  $0.1 R_{eff}$  except for the first bin, which is  $0.3 R_{eff}$ . This was done to increase the signal-to-noise ratios as there are very few galaxies near the center of the void. The greater size of the first radial bin does not affect our analysis results since the motivation is to investigate any difference in AGN abundance that might be present between the inner and outer void regions and cosmic voids have very large effective radii.

Figure 3.3 shows the AGN fraction plotted as a function of distance of the member galaxies from the void center for the five redshift intervals. The slopes and  $1\sigma$  uncertainties, where the amplitude uncertainty has been marginalized, for the best-fit lines are  $-0.001 \pm 0.004$ ,  $-0.005 \pm 0.002$ ,  $0.004 \pm 0.003$ ,  $-0.010 \pm 0.006$ , and  $-0.023 \pm 0.008$ , respectively, for the five redshift bins  $0.21 - 0.28$ ,  $0.28 - 0.35$ ,  $0.35 - 0.42$ ,  $0.42 - 0.56$ , and  $0.56 - 0.70$ . For the first three low redshift bins, we see some scattered results for  $f_A$  from the center of the void out to  $1.3 R_{eff}$ . The first and second redshift bins show a slightly negative trend, especially for the second bin where

the significance is  $\sim 2\sigma$ . The third bin has a positive slope which is not significant compared to measurement uncertainties. For the two higher redshift bins, we see  $\sim 2\sigma$  decreases in AGN fractions with distance from the void center by comparing the measured slopes and uncertainties.

### 3.4 Discussion and Conclusions

We found a significantly higher AGN fraction in the inner void regions in the two higher redshift bins ( $0.42 < z < 0.72$ ) either using small bin sizes or separating the voids into two regions. There is a 50% increase in  $f_A$  in the inner void region for the higher redshift voids, and we observe a decrease in AGN abundance as we move away from the void center. For the lower redshifts, the second bin ( $0.28 < z < 0.35$ ) shows a moderate decreasing trend ( $\sim 2\sigma$ ) in Figure 3.3, whereas the first and third  $z$  bins do not show a significant dependence on voidcentric distance when the uncertainties are taken into account. Although the difference in the analysis conclusions in the five redshift bins coincides with the LOWZ and CMASS boundary, where we measured environmental dependent AGN fractions in CMASS voids but largely no dependence for LOWZ counterparts, we did not identify potential biases affecting our analysis results between CMASS and LOWZ samples, since our analysis was focusing comparing different void regions within the same redshift bin and potential biases in galaxy, AGN, and void selections will cancel out in the comparison. There are differences in selection of galaxies for LOWZ and CMASS samples, where the LOWZ galaxy sample selects bright, red galaxies and CMASS, similarly, targets luminous, red galaxies, along with extending to some blue galaxies. While this limits our analysis to more luminous red galaxies for both low and high- $z$  ranges, the selection bias is consistent for inner and outer void regions. The void size distributions between LOWZ and CMASS samples are slightly different; however, again, since we are comparing the

AGN fractions in the inner and outer void regions, it is unlikely these size difference can contribute significantly to our analysis results. The redshift range  $z < 0.7$  of this study is relatively narrow compared to the parent quasar catalog with  $z \leq 7$ , and the quasar selection at  $z < 0.7$  mainly relies on the UV excess approximated by the  $u - g$  color (Ross et al. 2012). Thus, it is unlikely that the biases from quasar selections at  $z < 0.7$  contribute to the differences in our analysis between LOWZ and CMASS samples. Thus, the weaker environmental dependence for the three lower redshift bins could be physical, where the void environment close to the void center and in the outer parts responsible for AGN triggering has become more homogeneous as voids evolved, or it could be a result of the sample size. The spectroscopic SDSS data, while it provided more accurate redshifts, limited the sample to a smaller size, preventing us from measuring a minute trend smaller than the one observed in the two high redshift bins.

Our result of finding an increasing AGN fraction as we move toward the center of the void, in some redshift bins, provides a baseline result to be tested further with future studies. In the overdense regions, it is a better established result that the AGN abundance is lower in clusters and groups compared to the surrounding field regions at  $z < 1$  (e.g. Lopes et al., 2017; Mishra & Dai, 2020). Combining the result from this analysis, where we found hints of higher AGN fractions at void centers, we propose a thesis that at low redshifts where the AGN activities have declined from the cosmic peak, there is an overall trend of decreasing AGN activities with increasing environment density from the lowest void to the highest cluster regions, and this can be further confronted with future analysis using larger data sample.

Study conducted by Constantin et al. (2008) showed no change in AGN abundance from voids to walls for massive, luminous galaxies ( $M_r \lesssim -20$  and  $\log M/M_\odot > 10.5$ ) at very low redshifts which is in agreement with our results of finding no significant trend for lower redshifts. For moderately massive and luminous galaxies

( $M_r \sim -20$  and  $\log M/M_\odot < 10.5$ ), Constantin et al. (2008) found higher AGN abundance in voids than walls, especially for low-luminosity AGN.

According to the model that the inflow of cold gas toward the center of the galaxy and accretion onto the central engine regulates black hole growth (e.g. Di Matteo et al., 2005; Hopkins et al., 2005; Zanisi et al., 2021), the availability of gas in these systems would determine the AGN activity. Since we have selected the luminous galaxies ( $M_r < -20$ ) in both inner and outer void regions, they have more matter available to feed the central AGN. It is possible that the galaxies in the inner void region are able to hold onto their gas reservoirs in the absence of less gravitational disruptions resulting from the interactions with nearby systems as would be the case for outer regions of the void, where galaxies near and in the walls are not as isolated. This could potentially explain the higher AGN fractions in the void centers observed at the two higher redshift bins.

It is worth noting that our study is based on the BOSS CMASS catalog to select galaxies at high redshifts which selects more red galaxies. This may result in the selection of more galaxies in the outer regions of the void since galaxies that are found near the void center tend to be bluer and faint (e.g. Bruton et al., 2020; Rojas et al., 2004). However, this selection bias would affect the AGN and normal galaxies equally and thus, would not skew the  $f_A$  toward a higher value for the outer regions. We also measure the trend of AGN abundance relative to blue galaxies with voidcentric distance for the two highest redshift bins for discussion purposes. For this, we used the results from Bruton et al. (2020) which is a comparative study of the relative abundance of red and blue galaxies in voids. Bruton et al. (2020) uses the CMASS data and galaxies from the WiggleZ Dark Energy Survey (Drinkwater et al., 2010) to study the density profiles of the red and blue galaxies as a function of the void radius. They report lower red-to-blue galaxy ratio at void centers, and their relation can be used to convert the AGN fraction for CMASS galaxies investigated in

this paper to the AGN fraction with respect to blue galaxies. After doing that, we do not find a significant trend for  $f_A$  relative to the blue galaxies with distance from the center of the void within error bars, in contrast to the decreasing AGN abundance from inner regions to the outer regions found in our study. This might be indicative of differences in the evolutionary track or environmental dependence of the red versus the blue galaxies in the voids or simply the case where signal-to-noise is low to make any conclusions. A larger sample of blue galaxies will be needed to study the AGN abundance in the blue galaxies. The red-to-blue galaxy ratio in LOWZ voids are not reported in (Bruton et al., 2020), which precludes us from estimating AGN-to-blue galaxy ratios in LOWZ voids.

While the literature for AGN activity and evolution of active galaxies in over-dense regions, like clusters and groups, and their surrounding fields, is rich, the field of investigating the AGN evolution in cosmic voids remains greatly unexplored, but is extremely important to study the impact of local and global environmental factors that might play a role in triggering the nuclear activity in the central engine. The triggering mechanisms can also provide useful insight into the different conditions present in the cosmic voids and their evolution as compared to the high-density regions of the Large Scale Structure. Future studies using larger samples of spectroscopic data will be able to increase the signal-to-noise ratio and constrain the void AGN abundance better at lower redshifts and enable the expansion of this analysis to a much larger redshift range.

### **3.5 Acknowledgements**

This chapter is reproduced with permission from AAS from the publication: Mishra, H. D., et al. 2021, ApJL, 922, L17, “Active Galactic Nuclei Abundance in Cosmic

Voids”, accepted in the *Astrophysical Journal Letters*. Here is the original publication’s author list: Hora D. Mishra, Xinyu Dai, and Eduardo Guerras.

We are grateful to the anonymous referee for the helpful comments and recommendations that made the paper clearer and stronger. We acknowledge the financial support from the NASA ADAP programs NNX15AF04G, NNX17AF26G, NSF grant AST-1413056.

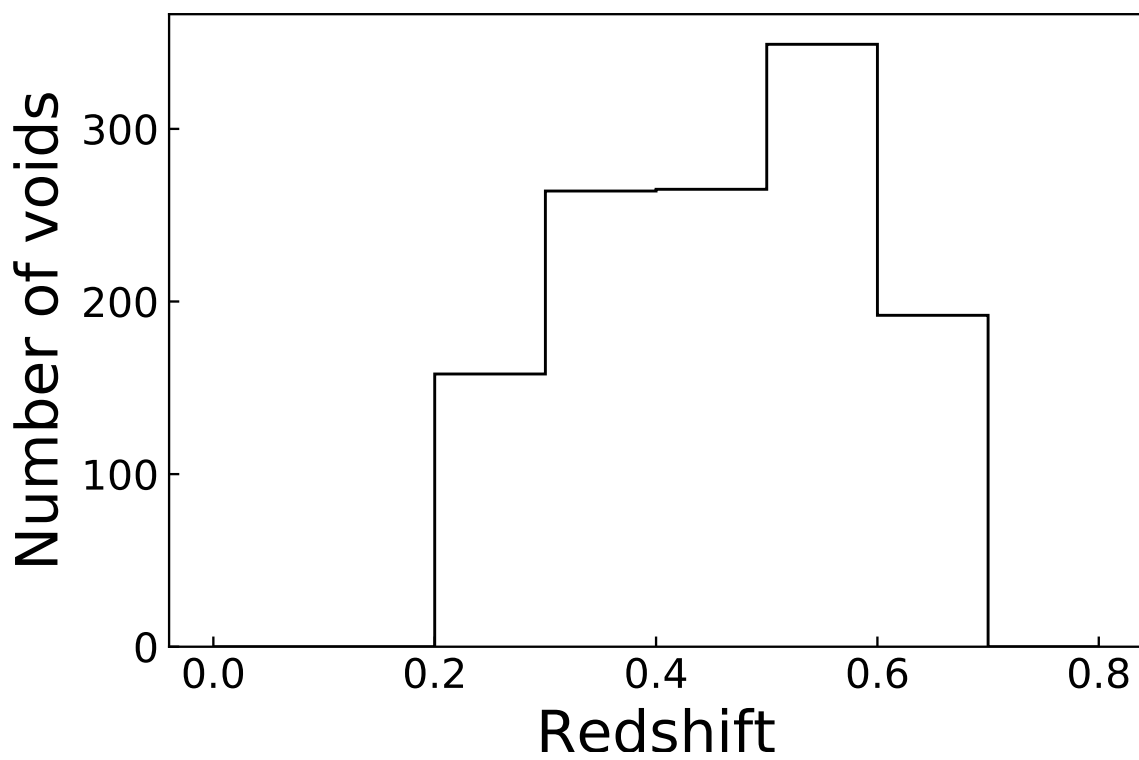


Fig. 3.1.— Redshift distribution for the voids used in this study.

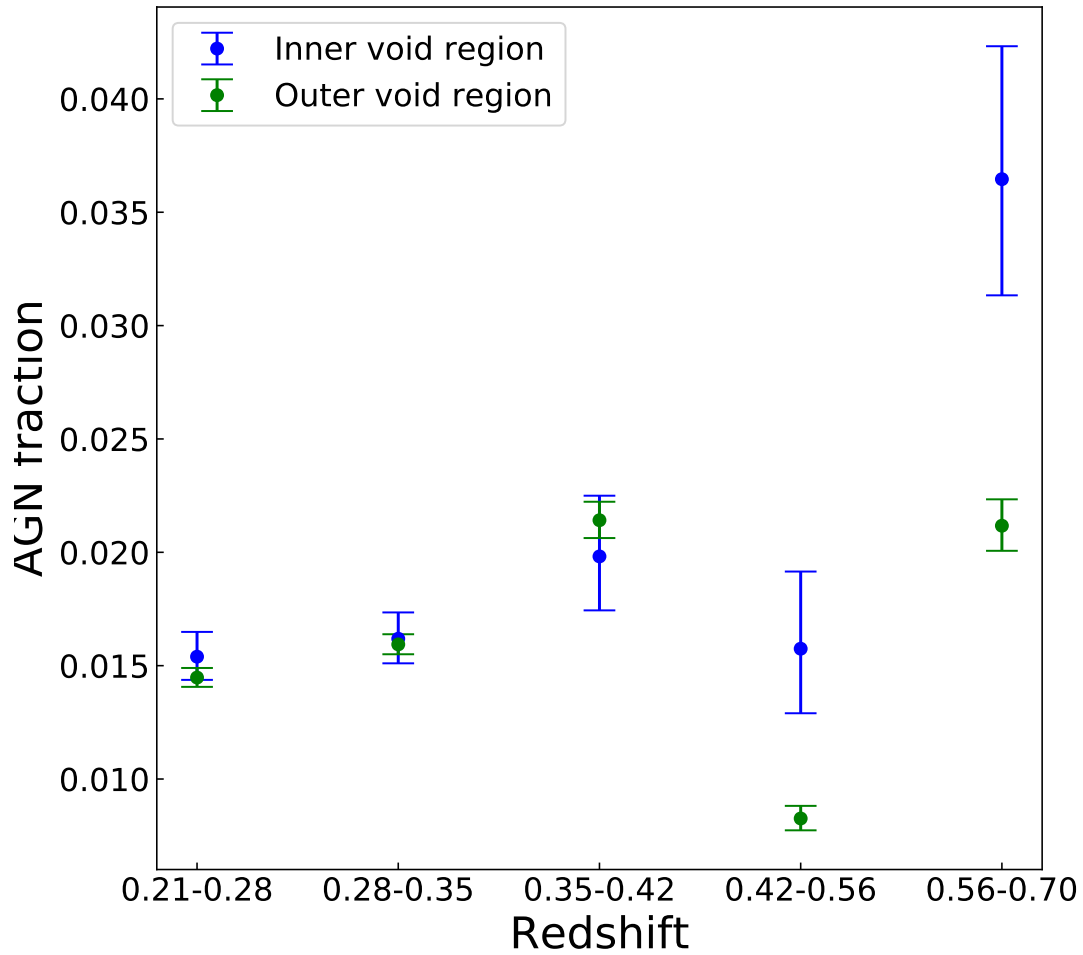


Fig. 3.2.— AGN fraction in the inner and outer regions of the void for the five redshift intervals. The errors are Poisson errors that correspond to  $1\sigma$  confidence limits.



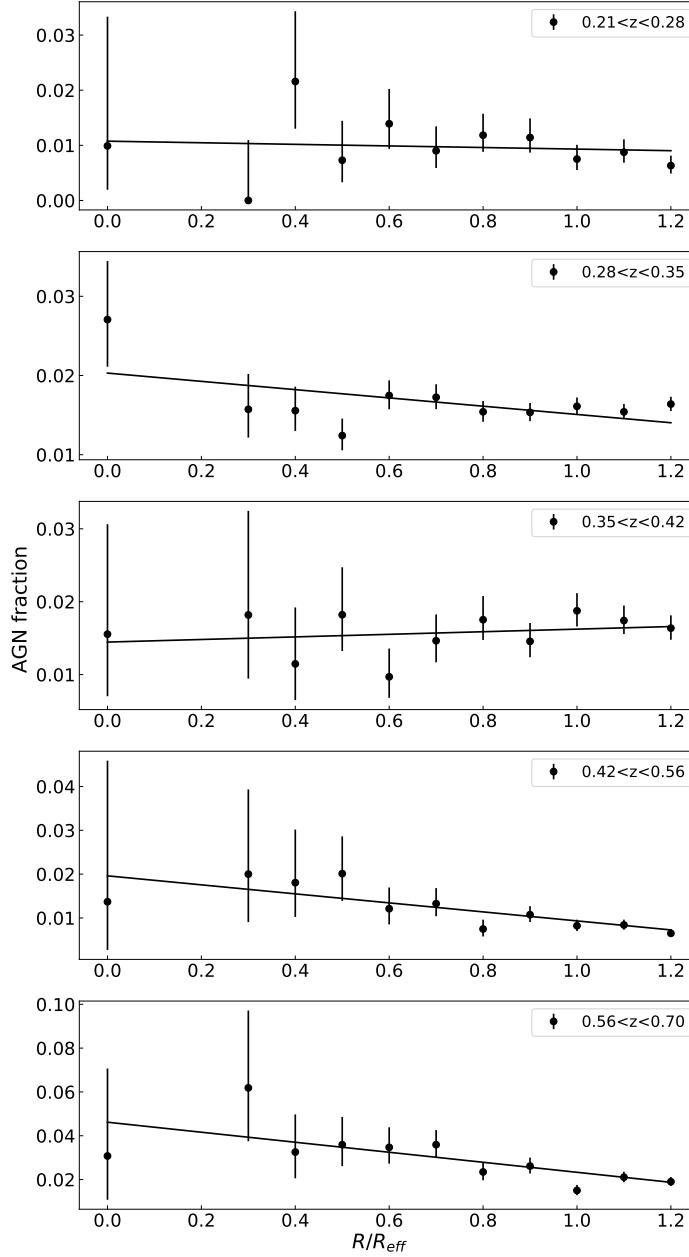


Fig. 3.3.— AGN fraction as a function of the distance from the center of the void in the units of  $R_{eff}$  (the effective radius of the void region) for the five redshift intervals. A best-fit linear model (solid black line) has been calculated for each bin.

Table 3.1. AGN fraction in inner and outer void regions for the five redshift bins

Redshift <sup>a</sup>	Inner void	Outer void	Slope <sup>b</sup>	AGN*	Non-AGN*
$0.21 \leq z < 0.28$	$0.012^{+0.003}_{-0.003}$	$0.0086^{+0.0009}_{-0.0008}$	$-0.001^{+0.004}_{-0.004}$	19;94	1585;10820
$0.28 \leq z < 0.35$	$0.016^{+0.001}_{-0.001}$	$0.0159^{+0.0004}_{-0.0004}$	$-0.005^{+0.002}_{-0.002}$	219;1319	13309;81436
$0.35 \leq z < 0.42$	$0.013^{+0.003}_{-0.002}$	$0.0167^{+0.0009}_{-0.0008}$	$0.004^{+0.003}_{-0.003}$	36;372	2660;21807
$0.42 \leq z < 0.56$	$0.035^{+0.006}_{-0.005}$	$0.0198^{+0.0011}_{-0.0010}$	$-0.010^{+0.006}_{-0.006}$	39;368	1073;18132
$0.56 \leq z < 0.70$	$0.062^{+0.007}_{-0.006}$	$0.0428^{+0.0017}_{-0.0017}$	$-0.023^{+0.008}_{-0.008}$	77;627	1163;14021

<sup>a</sup>All the data in each  $z$  bin is co-added.

<sup>b</sup>The slope of AGN fraction as a function of void-centric distance from inner to outer regions.

\*Inner region; outer region

# Chapter 4

## The Changing Look Blazar B2 1420+32

### 4.1 Introduction

Active Galactic Nuclei (AGN) are subdivided into several broad categories. Type I AGNs (also called quasars, Seyfert I) show a blue continuum from an accretion disk and broad emission lines created by photoionization. The continuum flux stochastically varies with modest amplitudes (e.g., MacLeod et al., 2010) and the broad lines respond after a delay. Type II AGNs (or Seyfert II) show only narrow lines and no continuum variability (e.g., Khachikian & Weedman, 1974; Nagao et al., 2001; Peterson et al., 2004). The most common paradigm to unify the two classes is to assume that the line of sight to the central engine is unobscured for Type I AGN and obscured for Type II AGN (e.g., Antonucci, 1993; Urry & Padovani, 1995). Most AGNs are not strong radio sources (i.e., “radio quiet”). Those which are radio loud can be divided into flat and steep spectrum radio sources. Here, the radio emission is believed to be due to a jet. The emission from flat spectrum radio quasars (FSRQs) is dominated by direct emission from the jet (e.g., Garofalo et al., 2018) and the steep spectrum sources are dominated by emission from the extended “lobes”, where the jet is interacting with the ambient medium (e.g., Fanti et al., 1990). Since the jets are relativistic, emission from the jet can dominate if the jet is pointed towards the observer. In the extreme case of blazars (also optically violent variables, OVV), the jet emission dominates at all wavelengths and no emission lines from an underlying quasar are visible. Blazars also show much higher amplitude and shorter time scale variability than quasars at all wavelengths, from the radio band to  $\gamma$ -rays (e.g., Edelson & Malkan, 1987; Urry & Padovani, 1995; Sesar et al., 2007).

An increasingly powerful means of understanding these divisions is to discover and analyze “changing look” AGN, where a source moves from one class to another. Most examples are AGN shifting between Type I and Type II spectra (e.g., Matt et al., 2003; Bianchi et al., 2005; Marchese et al., 2012; Shappee et al., 2014), a change which calls into question the standard unification picture for the difference between these classes. With the availability of large spectroscopic and time domain surveys, there have been a series of systematic searches that have found increasing number of examples of such AGNs (e.g., Álvarez Crespo et al., 2016; Kollatschny et al., 2018; Ai et al., 2020). One interesting bias of these searches is that they generally exclude blazars from the search because their optical variability amplitudes are so high. This is unfortunate, because changing look phenomena in blazars can provide useful insight into understanding the origin and particle acceleration processes of the radio jets, the role of changing structure and geometry of the jets, and the accretion disk-jet connection (e.g., Falcke & Biermann, 1995). Jets are also an important feedback mechanism at the galaxy cluster scale (e.g., McNamara & Nulsen, 2012) and the galaxy scale for the milder decelerated jets in radio galaxies (Capetti et al., 2005; Ishibashi et al., 2014; Baldi et al., 2019).

Blazars can be broadly divided into two categories – FSRQs and BL Lac objects, based on the rest-frame equivalent width of the strongest broad emission line. If the equivalent width is less than  $5\text{\AA}$ , the blazar is classified as a BL Lac object, otherwise, an FSRQ (Urry & Padovani, 1995). An alternate classification is based on the total broad line luminosity in units of the Eddington luminosity with the boundary at  $\sim 10^{-3}L_{Edd}$  (Ghisellini et al., 2011). As with Type I and II AGNs, there are arguments about potential unification schemes for the two classes. The broadband spectral energy distributions (SED) of blazars have two peaks. There is a lower energy component from sub-millimeter to X-ray energies due to synchrotron emission and a high energy component at MeV to TeV energies due to the inverse

Compton process. Fossati et al. (1998) and Donato et al. (2001) proposed that FSRQs and BL Lacs are a sequence, where the broadband SED moves blue-ward, with the bolometric luminosity decreasing from FSRQs to BL Lacs because cooling is more efficient in FSRQ jets than in BL Lacs (Ghisellini et al., 1998). In this picture, FSRQs have an efficient accretion disk powering the broad-line region (BLR) and BL Lacs have inefficient accretion disks. Alternative unification schemes for FSRQs and BL Lacs have been proposed (e.g., Giommi et al., 2012).

Studying systems that alternate between FSRQ and BL Lac states, using photometric and spectroscopic data, should illuminate their differences, but there are few studies in literature that can really be used to explore the question of blazar unification. While there are many studies of blazar variability at particular energies as well as studies of correlations of the variability between different energies and changes in the overall SED (Paliya, 2015; Zhang et al., 2015; Yoo & An, 2020), there are many fewer spectroscopic monitoring studies of blazars (e.g., Zheng & Burbidge, 1986; Bregman et al., 1986; Perez et al., 1989; Vermeulen et al., 1995; Ulrich et al., 1997; Corbett et al., 2000). In a few cases, large emission line flux changes have been observed. For example, Vermeulen et al. (1995) reported an increase in the  $H\alpha$  luminosity by a factor of 10 for the BL Lacertae prototype VRO 42.22.01 between 1989 and 1995. More recently, Isler et al. (2013, 2015) observed BEL equivalent width changes accompanied by large Fermi  $\gamma$ -ray flares for four FSRQs.

Here we discuss observations of the blazar B2 1420+32 doing this not once, but multiple times over a two year period. B2 1420+32 at  $z = 0.682$  was identified as an FSRQ and has been detected from radio to  $\gamma$ -energies. From its luminosity and broad line width, Brotherton et al. (2015) estimated a black hole mass of  $M_{BH} \simeq 4 \times 10^8 M_{\odot}$ , corresponding to a minimum light crossing time of approximately  $r_g/c = GM_{BH}/c^3 = 0.5$  hours (rest-frame). We first became interested in the source after the All-Sky Automated Survey for Supernovae (ASAS-SN, Shappee et al., 2014;

Kochanek et al., 2017) detected an optical flare of  $> 2$  mag on 2017 Dec 28 (Stanek et al., 2017) after nearly a decade of relative quiescence in the Catalina Real Time Survey (CRTS, Drake et al., 2009). At this point we started to obtain multi-color light curves using the Las Cumbres Observatory Global Telescope Network (LCOGT, Brown et al., 2013) 1m telescopes and spectra from a variety of sources. Over the next two years, additional flares were flagged in the optical/near-IR (e.g., Carrasco et al., 2019; Marchini et al., 2019),  $\gamma$ -rays (Ciprini, 2018), and even very high energy (VHE,  $E > 100$  GeV)  $\gamma$ -rays (Mirzoyan, 2020).

Here we report the results of our campaign. The most striking result is that during these high amplitude brightness fluctuations, B2 1420+32 shifted back and forth between the optical spectrum of an FSRQ and that of a BL Lac several times, while also developing new spectral features. We discuss the photometric data in section 4.2, including cross correlation analyses between the various energy bands. We present and discuss the spectral evolution in section 4.3. We consider the implications of this behavior for understanding FSRQs, blazars and their differences in section 4.4. We adopt the cosmological parameters  $\Omega_m = 0.3$ ,  $\Omega_\Lambda = 0.7$ , and  $H_0 = 70$  km s $^{-1}$  Mpc $^{-1}$ .

## 4.2 Temporal Evolution

B2 1420+32 is detected across the entire electromagnetic spectrum – from the radio to  $\gamma$ -ray bands. In this section we examine the optical and  $\gamma$ -ray variability of B2 1420+32 and the correlations between them. We also obtained a single Swift (Gehrels et al., 2004) XRT (Burrows et al., 2005) X-ray observation. These results are reported in Table 4.3 for the optical observations and Table 4.4 for the  $\gamma$ -ray observations. The X-ray observation is only described in the text.

For the  $\gamma$ -rays, we analyzed the full 12-year *Fermi*-LAT (Atwood et al., 2009) PASS8 data in the 0.1–500 GeV band from MJD 54689 to 59090. We used different

temporal bins depending on the brightness of the source. Prior to MJD 58000, we used bins of two months, and afterwards we used bins of 3 days. During the period with LCOGT monitoring data, we used bins of a single day, and during the TESS observations we used bins of 0.5 days to better match the high cadence TESS optical data. For each bin, we performed a maximum likelihood analysis using the *PYTHON* script *make4FGLxml.py*<sup>a</sup> to model the source spectrum and flux. The minimum detection threshold is set at  $TS = 2.69$ , corresponding to the 90% confidence level.

The optical data came from multiple sources. The earliest data is a V-band light curve from CRTS (Drake et al., 2009). Next we used the ASAS-SN V- and g-band data (Shappee et al., 2014; Kochanek et al., 2017), with the light curves obtained using image subtraction as described in Jayasinghe et al. (2018) and Jayasinghe et al. (2019). B2 1420+32 was observed by the Transiting Exoplanet Survey Satellite (TESS, Ricker et al., 2015) during Sector 23. The TESS band light curve was extracted using image subtraction methods optimized for TESS, as described in Vallely et al. (2019).

We monitored B2 1420+32 in the B, V, r and i-bands with the LCOGT (Brown et al., 2013) 1-m telescope at the McDonald Observatory. After basic reduction, the images were downloaded from Las Cumbres Observatory Science Archive (<https://archive.lco.global>). We used the IRAF (Tody, 1986) *apphot* task to perform aperture photometry with an aperture size twice the full width at half maximum (FWHM) of the stellar profile. AAVSO Photometric All-Sky Survey (APASS; Henden et al., 2016) DR9 catalog stars were used for photometric calibration.

We observed B2 1420+32 with *Swift* (Gehrels et al., 2004) on 2018-01-20:UT 15:44:46 for 1 ks with the XRT in the WT mode. We measured a net count rate of  $0.046 \pm 0.019$  ct s<sup>-1</sup> in the 0.2–10 keV band with an unabsorbed flux of  $1.7 \times 10^{-12}$  erg cm<sup>-2</sup> s<sup>-1</sup>, assuming a powerlaw photon index of 1.7 and adopting a Galactic

---

<sup>a</sup><https://fermi.gsfc.nasa.gov/ssc/data/analysis/user/>

absorption of  $N_{\text{H}} = 1.07 \times 10^{20} \text{ cm}^{-2}$  (HI4PI Collaboration et al., 2016). Compared to the *ROSAT* All-Sky Survey flux of  $5.4 \times 10^{-13} \text{ erg cm}^{-2} \text{ s}^{-1}$  in the 0.1–2.4 keV band (Massaro et al., 2009) or equivalently  $9.3 \times 10^{-13} \text{ erg cm}^{-2} \text{ s}^{-1}$  in the 0.2–10 keV band, the X-ray flux increased by a factor of 2. Prince et al. (2019, 2021) measured an increase in X-ray activity using the Swift-XRT on MJD 58830 with an unabsorbed flux of  $8.3 \pm 1.7 \times 10^{-12} \text{ erg cm}^{-2} \text{ s}^{-1}$  in the 0.3–10 keV band, assuming a powerlaw photon index of  $1.35 \pm 0.22$ . This is a further increase in the XRT flux by a factor of 5.

Figures 4.1 and 4.2 show the optical and  $\gamma$ -ray evolution on a series of time scales. Fig. 4.1 shows the evolution over the last 15 years and is divided roughly into the pre and post-outburst phases. Over the entire decade long period of photometric monitoring, the long-term  $\gamma$ -flux increased by a factor of 1500, when comparing the highest and lowest  $\gamma$ -ray fluxes detected, and the optical flux increased by a factor of 100. The top panel of Fig.4.2 shows the period in 2018 where we obtained the higher cadence, multi-band LCOGT data. Finally, the bottom panel of Fig.4.2 shows the 26 day period of TESS observations in early 2020. For roughly the decade prior to the ASAS-SN flare at the end of 2017, the source was fairly quiescent. The optical mean magnitude was  $\langle V \rangle = 18.3$  with a scatter of 0.20 mag. This is similar to its fluxes in the SDSS survey, measured on March 17, 2004 and the early CRTS data. Other than a weak flare in June 2009 there is little variability. Similarly, the  $\gamma$ -ray flux is low (mean =  $1.4 \times 10^{-8} \text{ ph/s/cm}^2$ ), with too few counts to really characterize the variability.

The bottom panel of Fig.4.1 shows that the optical flare flagged by ASAS-SN was accompanied by a  $\gamma$ -ray flare (MJD 58100–58150). The optical outburst, where the flux increases by  $3.0 \pm 0.2$  mags (factor of 16), was intensely followed-up with multi-band LCOGT observations (Figure 4.2, top panel). However, the  $\gamma$ -ray flux does not show a significant flare at the peak of the optical outburst (MJD 58125). Afterwards,



the optical flux remained somewhat higher than before the flare, but the  $\gamma$ -ray flux increases by  $2.7 \pm 0.3$  mags. Another  $\gamma$ -ray flare is observed near November 2018 (MJD 58450) when the flux increases by a factor of 16, after which the  $\gamma$ -ray flux stays in the high state, and the amplitudes of the  $\gamma$ -ray flares are reduced to 1.5 mag. Then, near May 2019, both the optical and  $\gamma$ -ray fluxes increased by another two orders of magnitude (Fig.4.1, bottom panel), with a further increase in March 2020 (MJD 58868) to a peak of  $g = 14.4$  mags and  $2.0 \times 10^{-6}$  ph/s/cm<sup>2</sup>, respectively. At this peak, the optical flux is 6 times brighter than the pre-flare mean, while the  $\gamma$ -ray flux is 16 times brighter. The optical and  $\gamma$ -ray data follow each other almost exactly.

Finally, the bottom panel of Figure 4.2 shows the brief period of TESS observations (MJD 58927–58954) with the Fermi data binned into 0.5 day intervals. The high S/N and cadence (0.5 hours) TESS light curve shows multiple, intra-day flares with the flux change being as large as a factor of 4, for example, at MJD 58927 and 58933. The  $\gamma$ -flux appears to track the TESS light curve (Figure 4.2, bottom panel), although the lower S/N in the smaller temporal bins limits the comparison. While the high amplitude  $\gamma$ -ray variability on intra-day timescale is frequently observed in blazars (e.g., Aharonian et al., 2007; Bonnoli et al., 2011; Aleksić et al., 2014), the accompanying high amplitude (3 mags) optical variability is rare (e.g., CTA 102, D’Ammando et al., 2019).

With these overlapping optical and  $\gamma$ -ray observations and their rich, correlated temporal structures, we can look for temporal offsets between the variations at different energies. We did this using both Javelin (Zu et al., 2011) and the Interpolated Cross Correlation Function (ICCF) (Peterson et al., 1998, 2004) methods, focusing on the Javelin results since they are generally less biased and provide better uncertainty estimates (Yu et al., 2020). For the inter-optical bands, we used the multi-band LCOGT light curves measured between MJD 58124–58360 (Figure 4.2,

top panel), to find lags between the LCOGT BV, Vr, and ri light curves of  $-0.07_{-0.69}^{+0.24}$ ,  $0.05_{-0.27}^{+0.15}$ , and  $0.06_{-0.43}^{+0.10}$  days, respectively. For the  $\gamma$ -ray-optical band correlation, we first performed the analysis between the long-term Fermi and ASAS-SN g-band light curves between MJD 58100–59000 and around the overall peak of the light curves (MJD 58800–59000) between Fermi and ASAS-SN-g band, then in short periods with either significant flares or higher quality data during the period with LCOGT coverage (MJD 58124–58360) and the TESS segment (MJD 58927–58954). The four  $\gamma$ -optical lags between the long-term Fermi-ASAS-SN g band, Fermi-ASAS-SN g around the overall peak, Fermi-LCOGT B, and Fermi-TESS are measured as  $3.3_{-6.3}^{+7.7}$ ,  $0.9_{-3.1}^{+0.1}$ ,  $0.4_{-3.6}^{+3.2}$ , and  $-2.1_{-1.5}^{+3.1}$  respectively. Using the ICCF method, we found that the optical light curves are well correlated with no significant inter-band lags, (e.g.,  $0.00 \pm 0.35$  days between  $B$  and  $i$  bands). For the  $\gamma$ -ray and the ASAS-SN light curves, we found a lag  $0.00 \pm 0.45$  day using the ICCF method. We also confirmed that all of these light curves are significantly correlated (Figure 4.3). The fractional amplitudes of many of the optical and  $\gamma$ -ray flares are quite similar (Figure 4.1).

### 4.3 Spectral Evolution

We have nine spectra to examine the spectra variability, the archival SDSS spectrum from August 2005 and 8 spectroscopic follow-up observations after the 2018 January outburst. The spectra are shown in Figures 4.4 and 4.5, where we present the spectra ordered by time in Figure 4.4 and by absolute flux in Figure 4.5. The first format makes it easier to follow the evolution, while the second makes it easier to see how the spectral structure changes with luminosity. Table 4.1 lists the spectroscopic observations with the parameters describing the continua, and Table 4.2 lists the emission line measurements. We corrected the spectra for Galactic extinction of  $E(B - V) = 0.001$  (Schlegel et al., 1998) and converted them into the rest-frame.

The spectral analysis was performed using CIAO’s Sherpa software (Freeman et al., 2001), by minimizing the  $\chi^2$  statistics of the fits, which also provides uncertainties of the fitting parameters. We first fit the continuum by filtering out the spectral regions with major emission lines including Mg II, H $\beta$ , H $\gamma$ , [O III] lines, earth absorption lines, and potential artifacts from data. For spectra 1, 6, 7, 8, and 9 with significant Fe emission, we further filtered out Fe emission bands from the continuum fitting process leaving only spectral windows with minimal Fe emission contributions. However, for spectra 8 and 9, we kept the spectral regions with moderate Fe emission contributions to increase the continuum fitting regions and better constrain the continuum model, since the fitting process suggested more complex continuum models. For all the spectra, the continuum was fit first using a power law model, since the non-thermal jet emission is assumed to be a power-law, and we obtained reduced  $\chi^2/\text{dof}$  of 1.8/89, 1.5/418, 2.0/4000, 1.1/1722, 0.82/4049, 2.1/3190, 1.64/1791, 1.7/546, and 1.4/348, respectively for the nine spectra. The reduced  $\chi^2$  values are less than 2.1 for all the fits, and we generally consider them to be acceptable, because either the uncertainties of the spectra can be underestimated/overestimated or there are the still unaccounted emission line contributions in the spectral fitting regions. We next checked if alternative or additional model components are needed for the continuum model, by examining the presence of continuous residuals above or below the best-fit models, and identified spectra 4, 7 and 8. For spectrum 4, the broken powerlaw model was used to improve the  $\chi^2$  value and hence the fit, where the reduced  $\chi^2$  is 0.44 significantly decreased from 1.1 for a single power-law. For spectra 7 and 8, adding a blackbody component have improved their fitting statistics from reduced  $\chi^2 = 1.64$  to 0.94 for spectrum 7 and from 1.7 to 0.63 for spectrum 8. The residuals of the fittings were also more randomly scattered about the alternative broken powerlaw model or the addition of blackbody component for spectra 4, 7 and 8, indicating better fits compared to the single powerlaw model. For the emission

line measurements, we followed the general steps of Shen et al. (2011), by first fitting a local power-law to the spectral regions containing the emission lines, then adding Gaussian components for the lines. We first used one Gaussian model for each emission lines, and obtain reduced  $\chi^2 < 1.2$  for all the fits with the residuals randomly scattered about the best-fits, suggesting single Gaussian models are adequate for modeling these lines. In most cases, we allow the line center, width, and flux to be free parameters. However, when the S/N is too low, we fix the widths of the lines to reasonable prior values. For the Fe pseudo-continuum, since the observed profiles can be quite different from those typically observed in non-jetted AGN (Figures 4.4 and 4.5), we did not use the template fitting method, but simply estimated the flux by subtracting the continuum from the observed spectra and excluding other known spectral lines.

B2 1420+32 shows rich and complex spectral changes, with multiple transitions between the FSRQ and BL Lac spectral types. Here we describe the main features. From spectrum 1 to 10, we see the source transition from an FSRQ (spec 1)  $\rightarrow$  BL Lac (specs 2–4)  $\rightarrow$  FSRQ (spec 5–7)  $\rightarrow$  BL Lac (specs 8–9), accompanied by complex line and continuum flux changes. Figure 4.6 shows the line flux and equivalent width variations for the 9 spectral epochs. The archival SDSS spectrum (spec 1) of B2 1420+32 is a typical FSRQ spectrum, with a powerlaw continuum and broad Mg II,  $H\beta$ ,  $H\gamma$ , and [O III] lines with equivalent widths ranging from 4–35Å. Spectra 2–4 were taken during the January 2018 outburst, and we can see that the spectrum evolved into a BL Lac spectrum with an almost featureless continuum and BEL equivalent widths  $< 5\text{Å}$  over spectra 2–4, and then back to an FSRQ in spectrum 5 when the continuum drops. The broad lines vary in both the line flux and equivalent widths. Comparing the Mg II flux and equivalent width variations during the transition of FSRQ  $\rightarrow$  BL Lac  $\rightarrow$  FSRQ in spectra 1–5 (excluding spectrum 2 because of its large measurement uncertainties), we find that the Mg II

flux changes by a factor of two and the equivalent width first decreases by a factor of 10 and then increases by a factor of 4. The much larger equivalent width variations suggest that the change to having the spectrum of a blazar is mainly due to the large changes in the continuum flux. We also correlated Mg II equivalent width with the continuum and found a negative correlation using Pearson correlation coefficient, with a correlation coefficient of  $-0.5$ . We see a decreased Mg II equivalent width as the jet contribution increases consistent with model predictions (e.g. Foschini, 2012). Spectrum 4 exhibits a broken power-law continuum.

We continued spectroscopic monitoring as the source continued to show large gamma-ray and optical variability. Spectrum 6 shows a significant Fe II pseudo-continuum, and spectra 7 and 8 show additional components that can be modeled with blackbodies with temperatures of 5200 and 12,000 K, respectively, on top of the power-law continuum. In spectrum 9, the continuum returned to a single power-law, with the addition of Fe pseudo-continuum emission in the rest-frame ultraviolet. Between spectra 6 and 9, the source again changes from an FSRQ into a BL Lac. The broad Mg II line flux drops by a factor of 1.7 while the equivalent width drops by a factor of 28. Figure 4.6 shows the evolution of emission line fluxes and equivalent widths for the major emission lines and Fe emission. The broad  $H\beta$  and  $H\gamma$  lines are only marginally detected in spectra 2–8. The upper limits are best constrained in spectrum 7, where  $H\gamma$  and  $H\beta$  fluxes drop by a factor of 4. The equivalent widths drop by a factor of 9 from the SDSS spectrum. There are detections of a narrow [O III]5007Å line in spectra 1–9. The line flux increases by a factor of 1.5 between the minimum and maximum values, while the equivalent width changes by a factor of 70. We note that while this small line flux change could be explained by observing conditions like clouds (Fausnaugh et al., 2017), the large change in equivalent width suggests this may be a real phenomenon and not just systematics. The variations in the Mg II,  $H\beta$ ,  $H\gamma$ , and [O III] lines are consistent with the picture that the differences

between FSRQ and BL Lac spectra are due to the changes in the continuum flux. Where they can be measured, the actual broad line widths and fluxes change little. For example, the FWHM of Mg II is  $\sim 4000 \text{ km s}^{-1}$  and that of [O III]5007Å is  $\sim 500 \text{ km s}^{-1}$  both before and after the FSRQ  $\rightarrow$  BL Lac  $\rightarrow$  FSRQ evolution.

#### 4.4 Discussion

Our multi-wavelength and spectroscopic monitoring observations show that B2 1420 +32 exhibits extreme spectral and temporal variability. We observe flux increases over the past two decades by factors of 1500 (8 mags) and 100 (5 mags) in the  $\gamma$ -ray and optical bands, respectively, with correlated optical and  $\gamma$ -ray variability. The  $\gamma$ -ray and optical flux changes can be up to factors of 40 and 16 respectively, on week-to-month timescales and a factor of 3 on intraday timescales in the optical. The optical and  $\gamma$ -ray lightcurves are well-correlated with lags  $< 3$  days.

We can estimate the sizes of the  $\gamma$ -ray and optical emission regions based on our variability and lag measurements. Here we use the mass reported in Brotherton et al. (2015) ( $M_{BH} \simeq 4 \times 10^8 M_{\odot}$ ), implying an Eddington luminosity of  $5.2 \times 10^{46} \text{ erg s}^{-1}$ . We also measured the black hole mass independently using H $\beta$  line width and luminosity from the SDSS spectrum and found the mass to be consistent within 2% the above mentioned value, and the Mg II mass is within 40%. The black hole has a gravitational radius size of  $r_g = 5.9 \times 10^{13} \text{ cm}$ . Assuming a typical Doppler factor of  $\delta = 10$  for the jet (Hovatta et al., 2009; Liodakis et al., 2017) and considering the source redshift of  $z = 0.68$ ,  $\Delta t_{intr} = \Delta t_{obs} \delta / (1+z)$ , an observed lag of one day corresponds to an emission region size of  $260 r_g$ . The measured inter-optical lags are  $< 0.5$  days, corresponding to an intrinsic source size of  $< 130 r_g$ . Using a conservative lag uncertainty of 3 days for our  $\gamma$ -ray-optical lag measurements on short time-scales, the  $\gamma$ -ray and optical emission regions are separated by  $< 800 r_g$ .

Dramatic spectral variations were also observed. In particular, we observe, for the first time, multiple, rapid transitions between the FSRQ and BL Lac spectral classifications. Few changing-look blazars have been reported previously, for example VRO 42.22.01 (Vermeulen et al., 1995) and 5BZB J0724+2621 (Álvarez Crespo et al., 2016), where a transformation from a BL Lac to an FSRQ spectral type was observed once. For our source, the initial FSRQ spectrum with broad emission lines with Mg II, H $\beta$ , and H $\gamma$  evolves to the featureless spectrum of a BL Lac object, and then back again, with the reappearance of Mg II lines plus a new Fe II and Fe III pseudo-continuum and other continuum features. However, the Balmer emission lines are never significantly detected after the first flares. The optical continuum changes in shape, where we can model it as a single powerlaw, a broken powerlaw, or a powerlaw plus blackbody components, depending on the spectrum.

Our optical spectra show that the optical emission during flares is still dominated by a powerlaw continuum, presumably from the jet. A jet origin is particularly indicated by the broken powerlaw spectrum, which is a characteristic non-thermal emission feature and has never been observed from accretion disks (Gierliński et al., 2001; Wu et al., 2013).

The large change in some of the line features shows that the BLR is significantly affected by the  $\gamma$ -ray and optical flares. While the Mg II, [O III], and Balmer line fluxes vary by a factor of 2–3, the equivalent width changes can be as high as a factor of 150 because of the huge changes in the optical continuum flux. This is consistent with the less dramatic case of 3C 279, where the Ly $\alpha$  flux is observed to vary by a factor of  $\sim 2$ , while the continuum changed by a factor of up to 50 (Koratkar et al., 1998). The lower variability amplitudes observed in these lines corroborate with the conclusions from studies of larger samples of moderate continuum variability blazars that the BLR clouds are mainly photo-ionized by the accretion disk with significant contribution from the jet to the ionization (e.g., Isler et al., 2013, 2015). The relative

consistency in the Mg II and [O III] line width measurements also suggests that the BLR is only partially affected by the dramatic optical and  $\gamma$ -ray variability. The appearance of a Fe II and Fe III pseudo-continuum is the exception, where we observe a flux increase by a factor of 45 from the archival SDSS to the most recent spectrum (spec 9), with a peak flux of 3% Eddington luminosity. The non-detections of Fe pseudo-continuum in spectra 2–5 can be caused by the reduction of the equivalent widths by the increase of the continuum flux. The appearance of a strong Fe II and Fe III pseudo-continuum suggests the disruption of dust clouds by shocks or radiation, which would free up a large amount of Fe (e.g., Kishimoto et al., 2011; Baskin & Laor, 2018; He et al., 2021). The variability in the emission line fluxes of different species (typically a factor of 2) and Fe II and Fe III ( $\sim 45$ ) suggests energy transfers from the relativistic jet to sub-relativistic components. It is also possible that the variations in the continuum flux from the disk (e.g., Kelly et al., 2009; MacLeod et al., 2010) could drive dust destruction while being masked by the far larger variations in the jet component.

One optical spectrum (spec 7) shows a prominent continuum feature, which is well-fit by a 5,200 K blackbody, and a second spectrum (spec 8) shows a prominent component well-fit by an 12,000 K blackbody. The two components have luminosities of 18–24%  $L_{Edd}$ . The narrowness of the blackbody peaks suggests that the emission source is most likely sub(mildly)-relativistic, because relativistic Doppler effects will broaden any narrow features. A modification from the powerlaw jet emission combined with the beaming effect can mimic a single blackbody spectral shape. These single temperature blackbody components are difficult to interpret as radiation from the accretion disk, because accretion disks span broad temperature ranges, leading to UV/optical SEDs that are essentially power-laws. Blackbody-like spectral components have been observed in blazars and they are commonly interpreted as the host galaxy contribution, particularly since many of them show absorption features typi-



cal of host galaxies (e.g., Paiano et al., 2020). However, the blackbody components detected in B2 1420+32 are clearly not from the host because the host contribution is constant. Here, the blackbody components are detected only when the source is near peak brightness, while there is no significant host component visible even in the archival, low-state, SDSS spectrum.

The unique blackbody components could be from the jet itself, if the jet is precessing and we are occasionally observing a part of the jet with low Doppler beaming factors. This model of changing viewing angles was also proposed to interpret the huge  $\gamma$ -ray and optical flux changes in CTA 102 (D’Ammando et al., 2019). Alternatively, it is possible that there are changes in the opening angles of the jet, and the blackbody component can be from episodes of jet activity with larger opening angles and low Lorentz factors propagating through a dust-rich region (presumably the torus) to free-up the ions producing the Fe pseudo-continuum. Regardless of the interpretation, the low Doppler factor suggests that these narrow blackbody spectra are more representative of the jet spectrum seen at a typical location in the central engine, and not directly along the jet.

AGN feedback has been broadly classified into the “quasar mode” and “radio mode”. The “quasar mode” is feedback from either the radiation (high-Eddington regime) or disk winds in the non-Eddington regime, while the “radio mode” is kinetic feedback from decelerated radio jet/lobes in low luminosity radio galaxies or galaxy clusters. Strongly relativistic jets are seldom considered as important galaxy scale feedback sources, because they penetrate through the galaxy and are only decelerated to mildly relativistic speeds for larger (cluster) scales. Here, we show that these jets may drive intermittent sub(mildly)-relativistic shocks in the central engine/host galaxy with luminosities of 20%  $L_{Edd}$  or Fe emission flux changes of 5%  $L_{Edd}$ .

Finally, we summarize the main conclusions of this paper:

- Between 2016–2019, the  $\gamma$ -ray and optical fluxes increased by factors of 1500 (8

mags) and 40 (4 mags) respectively. The optical variability amplitude observed is unprecedented, with the optical flux increasing by a factor of 100 (5 mags) compared to the SDSS observations in 1995.

- The optical- $\gamma$ -ray and inter optical band correlations constrain the  $\gamma$ -ray-optical lag to be  $< 3$  days and inter-optical band lags to be  $< 0.5$  days, corresponding to emission distance/sizes of less than  $\sim 800r_g$  and  $\sim 130r_g$ .
- B2 1420+32 is a changing-look blazar, transiting between the two major classifications of blazars, the FSRQ and BL Lac categories due to dramatic changes in the jet continuum flux diluting the line features.
- Complex spectral evolution is observed in both the continuum and emission lines, suggesting dramatic changes in the jet and photoionization properties of the emission line regions. The emergence of strong Fe II and Fe III pseudo-continuum is consistent with the sublimation of dust grains by either radiation or shocks releasing more Fe ions into the broad line regions. The Fe line fluxes approach  $3\% L_{Edd}$ .
- For the first time, we detect components in the optical spectra consistent with single temperature blackbody emission, with  $20\%$  of the Eddington luminosity.

This extreme variability we describe here has not been observed before. However, it may not be uncommon, because dedicated multi-band and spectroscopic monitoring of blazars are still rare. Dedicated searches for more changing-look blazars will extend the changing-look AGN studies to jetted AGNs and allow us to utilize the dramatic spectral changes to reveal AGN/jet physics.

## 4.5 Acknowledgements

This chapter is reproduced with permission from AAS from the publication: Mishra, H. D., Dai, X., et al. 2021, ApJ, 913, 146, “The Changing-Look Blazar B2 1420+32”, accepted in the *Astrophysical Journal*. Here is the original publication’s author list: Hora D. Mishra, Xinyu Dai, Ping Chen, Jigui Cheng, T. Jayasinghe, Michael A. Tucker, Patrick J. Valley, David Bersier, Subhash Bose, Aaron Do, Subo Dong, Thomas W.-S. Holoien, Mark E. Huber, Christopher S. Kochanek, Enwei Liang, Anna V. Payne, Jose Prieto, Benjamin J. Shappee, K. Z. Stanek, Saloni Bhatiani, John Cox, Cora DeFrancesco, Zhiqiang Shen, Todd A. Thompson, and Junfeng Wang.

We are grateful to the referee for the helpful comments and recommendations to make the paper stronger. We thank B. Peterson, R. Pogge, and J. Zhang for helpful discussions. HDM and XD acknowledge the financial support from the NASA ADAP program NNX17AF26G. We thank the Las Cumbres Observatory and its staff for its continuing support of the ASAS-SN project. ASAS-SN is supported by the Gordon and Betty Moore Foundation through grant GBMF5490 to the Ohio State University, and NSF grants AST-1515927 and AST-1908570. Development of ASAS-SN has been supported by NSF grant AST-0908816, the Mt. Cuba Astronomical Foundation, the Center for Cosmology and AstroParticle Physics at the Ohio State University, the Chinese Academy of Sciences South America Center for Astronomy (CAS-SACA), and the Villum Foundation. BJS, CSK, and KZS are supported by NSF grant AST-1907570. BJS is also supported by NASA grant 80NSSC19K1717 and NSF grants AST-1920392 and AST-1911074. CSK and KZS are supported by NSF grant AST-181440. KAA is supported by the Danish National Research Foundation (DNRF132). MAT acknowledges support from the DOE CSGF through grant DE-SC0019323. Support for JLP is provided in part by FONDECYT through

the grant 1151445 and by the Ministry of Economy, Development, and Tourism's Millennium Science Initiative through grant IC120009, awarded to The Millennium Institute of Astrophysics, MAS. TAT is supported in part by Scialog Scholar grant 24215 from the Research Corporation. We acknowledge the Telescope Access Program (TAP) funded by NAOC, CAS, and the Special Fund for Astronomy from the Ministry of Finance. PJV is supported by the National Science Foundation Graduate Research Fellowship Program Under Grant No. DGE-1343012.

ASAS-SN, Fermi, TESS, LCOGT, LTLT, MDM Hiltner, BAO 2.16m, Palomar, Hawaii 88in, Swift, SDSS

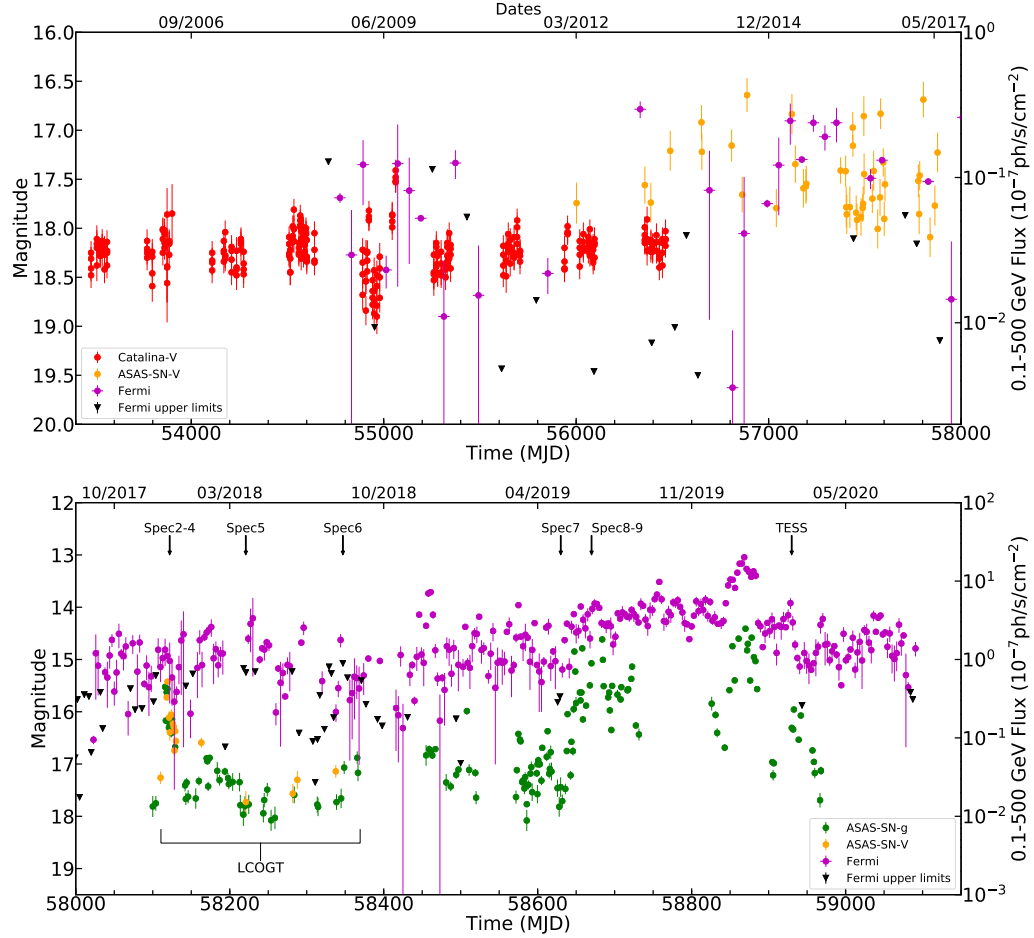


Fig. 4.1.— Long-term optical and 0.1–500 Gev  $\gamma$ -ray light curves of B2 1420+32, where the bottom panel shows the enhanced optical and  $\gamma$ -ray activities between MJD 58000 and 59100 and the top panel covers the range before MJD 58000. The  $\gamma$ -ray light curve is binned by 3 days in the bottom panel and 2 months in the top panel. The epochs of the spectroscopic observations, LCOGT, and TESS observations are marked.

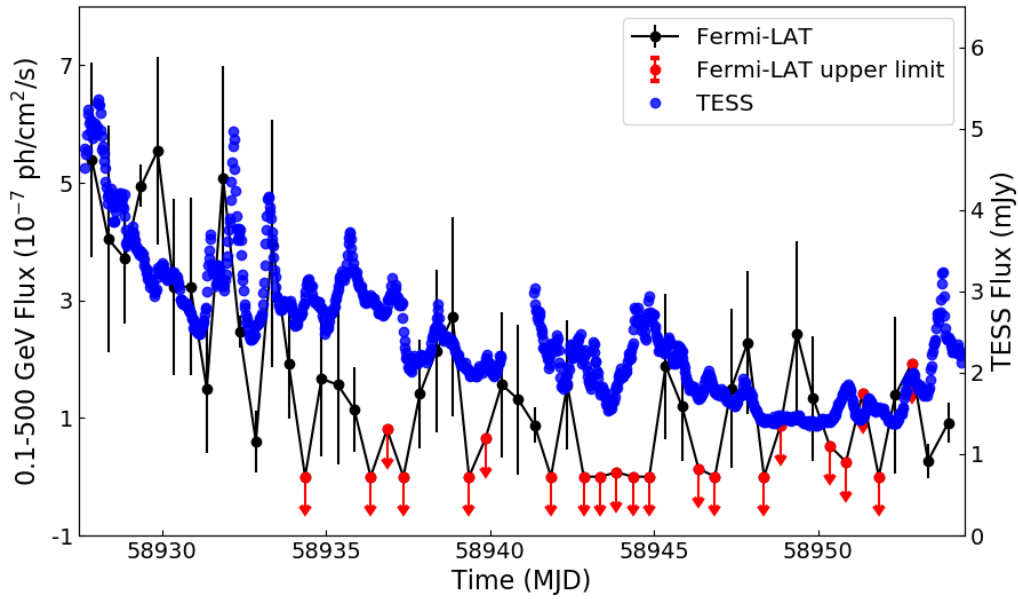
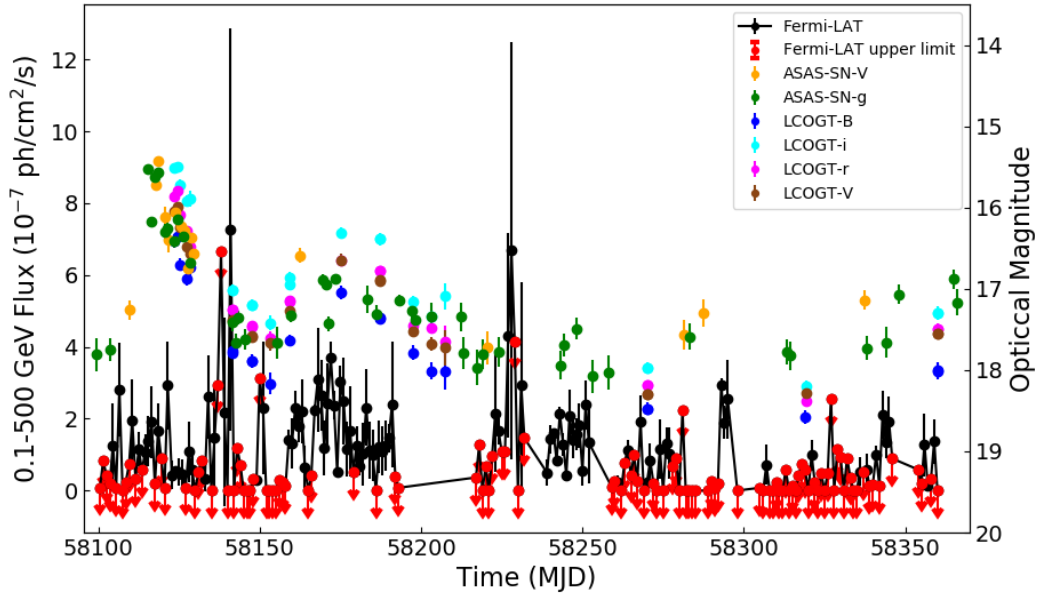


Fig. 4.2.— Multi-band optical LCOGT, ASAS-SN, and Fermi light curves of B2 1420+32 between MJD 58124 and 58360, where the Fermi data is binned by 1 day (top). TESS and Fermi light curves of B2 1420+32 between MJD 58927 and 58954, where the TESS cadence is 30 min and we binned the Fermi data by 0.5 days (bottom). The optical flux shows many flares on sub-day timescales with amplitudes exceeding 50%.

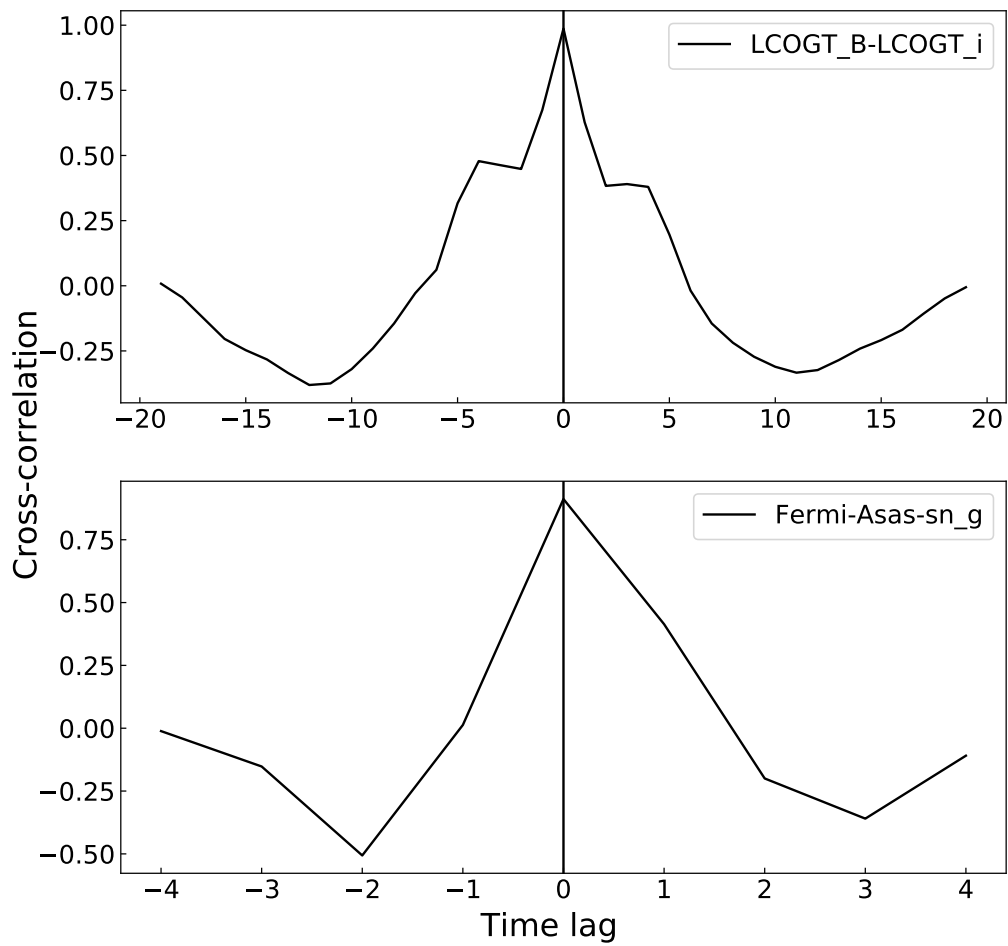


Fig. 4.3.— Two examples of the cross-correlations between the LCOGT B and LCOGT i-band (top panel) and the Fermi and ASAS-SN g-band light curves-overall peak (bottom panel) as a function of the time lag. For these cross-correlations, the lag estimates are  $0.0 \pm 0.4$  days (top) and  $0.0 \pm 0.5$  days (bottom).

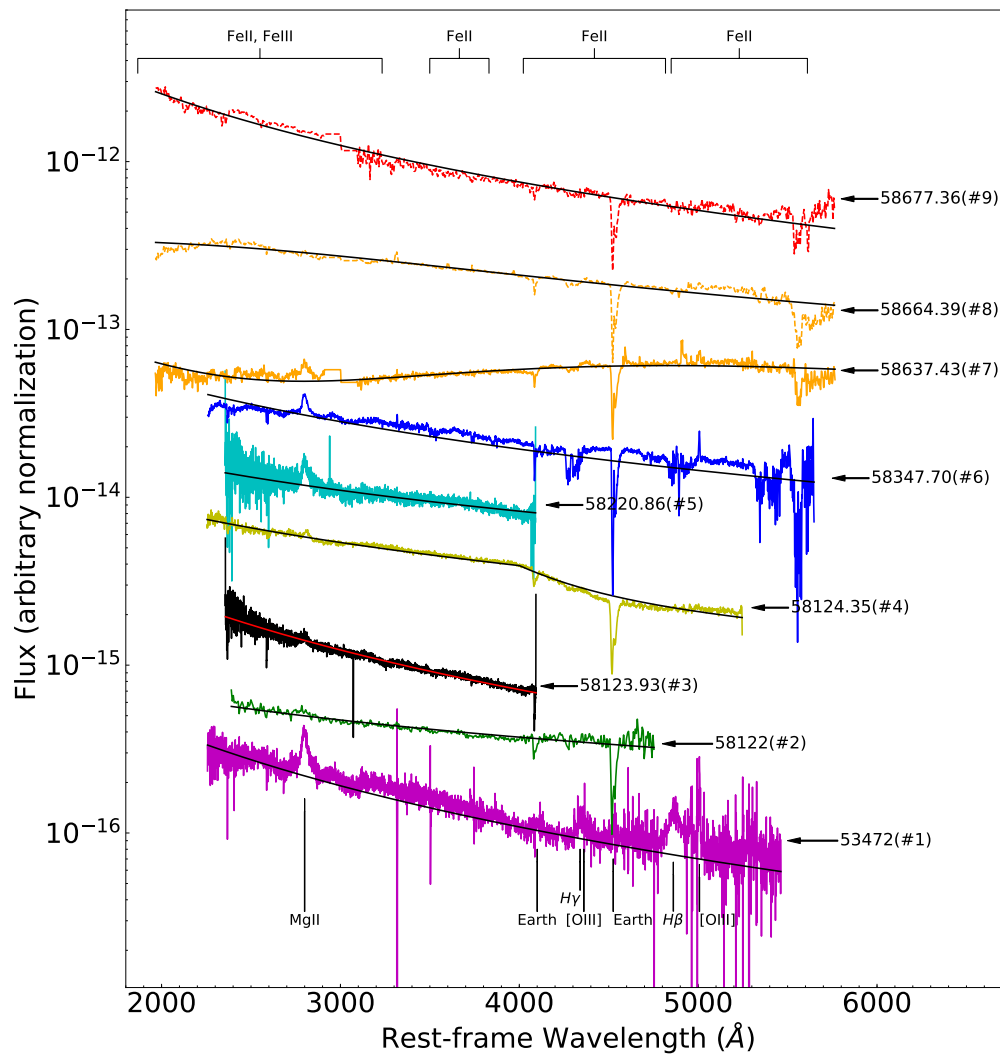


Fig. 4.4.— Spectroscopic evolution of B2 1420+32 in ascending chronological order from the bottom. The MJD of the observations and the spectrum number are given next to the arrows and the continuum fits are overplotted.



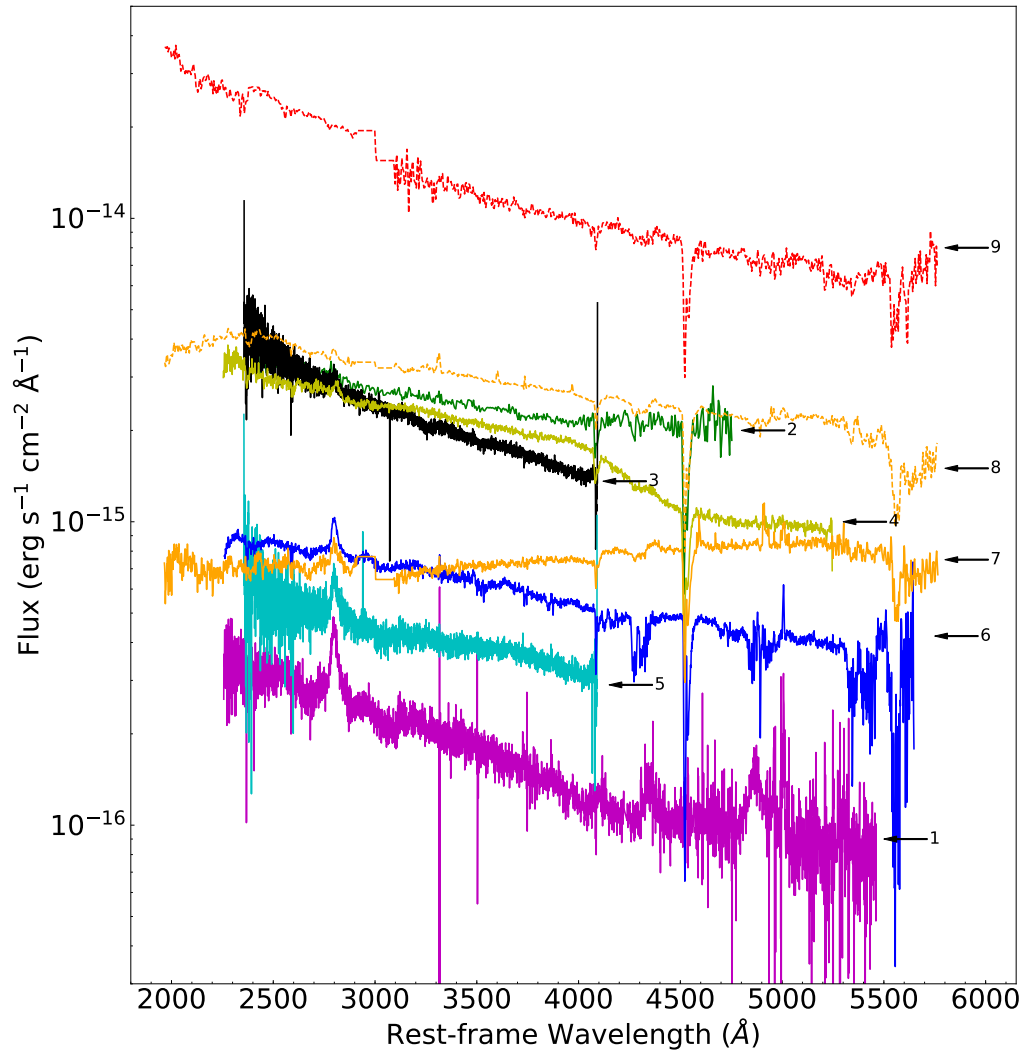


Fig. 4.5.— The spectra in absolute flux units. The number assigned to each spectrum describes the ascending chronological order in Table 4.1 and the labels in Fig. 4.4.

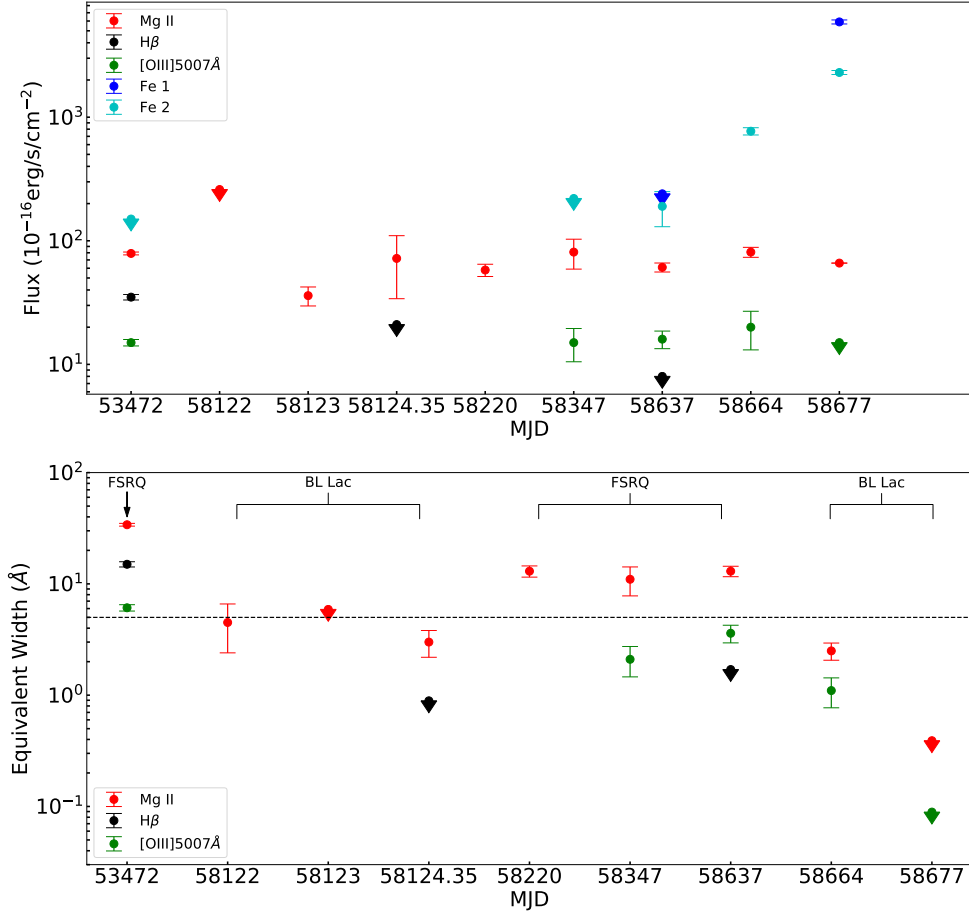


Fig. 4.6.— The evolution of Mg II, H $\beta$ , [OIII]5007Å, and Fe continuum fluxes from spectrum 1 to 9 in the upper panel. Fe 1 corresponds to the Fe II and Fe III emissions in 1250-3100Å and Fe 2 corresponds to 4900-5550Å Fe II emission. The lower panel shows the evolution of the equivalent widths (see Table 4.2). The black dashed line at 5Å denotes the equivalent width classification between FSRQ and BL Lac states. The downward triangles in both panels are upper limits.

Table 4.1. B2 1420+32 spectra continuum analysis

Spec	Telescope	Resolution (Å)	MJD	Powerlaw Amplitude <sup>a</sup>	Powerlaw Index 1	Powerlaw Index 2	Blackbody T (Kelvin)	Blackbody Flux <sup>b</sup>
1	SDSS	2.5	53472	$2.3^{+0.0042}_{-0.0042}$	$1.869^{+0.008}_{-0.008}$	...	...	...
2	LTLT	3	58122	$28^{+0.086}_{-0.086}$	$0.82^{+0.01}_{-0.01}$	...	...	...
3	2.4-m MDM	3	58123.93	$25^{+0.021}_{-0.021}$	$1.89^{+0.01}_{-0.01}$	...	...	...
4	2.16-m Xinglong	3	58124.35	$23.6^{+0.11}_{-0.11}$	$1.19^{+0.02}_{-0.02}$	$2.78^{+0.04}_{-0.04}$	...	...
5	2.4-m MDM	3	58220.86	$4.4^{+0.011}_{-0.011}$	$0.99^{+0.01}_{-0.01}$	...	...	...
6	f-JD-Palomar	7	58347.70	$7.1^{+0.033}_{-0.033}$	$1.64^{+0.01}_{-0.01}$	...	...	...
7	SNIFS	7	58637.43	$4.7^{+0.095}_{-0.097}$	$1.17^{+0.06}_{-0.06}$	...	$5200^{+29}_{-29}$	$4.8^{+0.12}_{-0.12}$
8	SNIFS	7	58664.39	$19^{+1.3}_{-1.4}$	$0.45^{+0.10}_{-0.11}$	...	$12000^{+320}_{-380}$	$6.2^{+0.35}_{-0.35}$
9	SNIFS	7	58677.36	$160^{+0.34}_{-0.34}$	$1.8^{+0.0085}_{-0.0085}$	...	...	...

<sup>a</sup>Normalized to 3000Å with a unit of  $10^{-16}\text{erg s}^{-1}\text{cm}^{-2}\text{Å}^{-1}$ .

<sup>b</sup>The flux unit is  $10^{-12}\text{erg s}^{-1}\text{cm}^{-2}$ .

Table 4.2. B2 1420+32 spectra emission line analysis

Spec	Mg II Flux	FWHM (km/s)	EQW (Å)	H $\beta$ Flux	FWHM (km/s)	EQW (Å)	H $\gamma$ Flux	FWHM (km/s)	EQW (Å)
1	$79^{+2.1}_{-2.1}$	$4800^{+160}_{-160}$	$34^{+0.97}_{-0.97}$	$35^{+1.8}_{-1.7}$	$3800^{+220}_{-210}$	$15^{+0.81}_{-0.77}$	$9.9^{+1.7}_{-1.6}$	$2600^{+340}_{-310}$	$4.3^{+0.75}_{-0.70}$
2	< 260	< 1400	$4.5^{+2.1}_{-2.1}$	...	...	...	...	...	...
3	$36^{+6.3}_{-6.3}$	3000*	< 5.9	...	...	...	...	...	...
4	$72^{+38}_{-35}$	$3200^{+2000}_{-1300}$	$3.0^{+0.81}_{-0.72}$	< 21	2000*	< 0.89	< 11	2000*	< 0.47
5	$58^{+6.6}_{-6.2}$	$3800^{+490}_{-430}$	$13^{+1.5}_{-1.4}$	...	...	...	...	...	...
6	$81^{+22}_{-19}$	$3600^{+1200}_{-890}$	$11^{+3.2}_{-2.7}$	...	...	...	...	...	...
7	$61^{+5.1}_{-4.9}$	$4800^{+580}_{-530}$	$13^{+1.4}_{-1.3}$	< 8.0	2000*	< 1.7	$2.3^{+1.7}_{-1.7}$	2000*	$0.49^{+0.37}_{-0.37}$
8	$48^{+14}_{-13}$	$2000^{+680}_{-550}$	$2.5^{+0.44}_{-0.45}$	...	...	...	...	...	...
9	< 66	1000*	< 0.39	...	...	...	...	...	...

<sup>a</sup>Flux unit is  $10^{-16}$  erg s $^{-1}$  cm $^{-2}$ .

\*These parameters were fixed.

Table 4.2. B2 1420+32 spectra emission line analysis (continued)

Spec	[OIII]4363Å Flux	FWHM (km/s)	EQW (Å)	[OIII]5007Å Flux	FWHM (km/s)	EQW (Å)
1	$2.2^{+0.39}_{-0.39}$	480*	$0.96^{+0.17}_{-0.17}$	$14^{+0.90}_{-0.87}$	$470^{+41}_{-38}$	$6.1^{+0.40}_{-0.39}$
2	...	...	...	...	...	...
3	...	...	...	...	...	...
4	< 3.3	< 210	< 0.15	...	...	...
5	...	...	...	...	...	...
6	< 2.5	< 480	< 0.35	$15^{+4.2}_{-4.5}$	< 420	$2.1^{+0.60}_{-0.64}$
7	< 0.67	< 480	< 0.16	$16^{+2.6}_{-2.4}$	$610^{+130}_{-103}$	$3.6^{+0.65}_{-0.60}$
8	< 2.4	< 480	< 0.13	$20^{+6.9}_{-6.9}$	< 420	$1.1^{+0.33}_{-0.33}$
9	< 13	< 480	< 0.09	< 15	< 420	< 0.089

<sup>a</sup>Flux unit is  $10^{-16}\text{erg s}^{-1}\text{cm}^{-2}$ .

\*These parameters were fixed.

Table 4.2. B2 1420+32 spectra emission line analysis (continued)

Spec	FeII,FeIII 1250-3100Å	FeII 3530-3800Å	FeII 4070-4750Å	FeII 4900-5550Å
1	...	$30^{+42}_{-42}$	...	< 150
2	...	...	...	...
3	...	...	...	...
4	...	...	...	...
5	...	...	...	...
6	...	< 160	< 110	< 220
7	< 240	...	...	$190^{+60}_{-60}$
8	...	...	...	$770^{+52}_{-52}$
9	$5900^{+220}_{-220}$	...	...	$2300^{+87}_{-87}$

<sup>a</sup>Flux unit is  $10^{-16}\text{erg s}^{-1}\text{cm}^{-2}$ .

\*These parameters were fixed.

Table 4.3. B2 1420+32 optical lightcurves

MJD	Telescope	Band	Magnitude	Uncertainty
53479.27321	CRTS	V	18.25	0.12
53479.28138	CRTS	V	18.48	0.13
53479.28951	CRTS	V	18.31	0.12
53479.2977	CRTS	V	18.41	0.13
53562.16491	CRTS	V	18.25	0.12
53562.17136	CRTS	V	18.14	0.12
58100.00768	ASAS-SN	g	17.81	0.20
58104.00069	ASAS-SN	g	17.75	0.14
58115.98322	ASAS-SN	g	15.52	0.03
58116.97997	ASAS-SN	g	16.17	0.03
58118.02747	ASAS-SN	g	15.62	0.03
58119.02784	ASAS-SN	g	15.56	0.03
58124.0043	LCOGT	B	16.41	0.06
58125.0281	LCOGT	B	16.36	0.07
58125.9248	LCOGT	B	16.70	0.07
58128.0192	LCOGT	B	16.88	0.07
58128.9496	LCOGT	B	16.73	0.12
58141.917	LCOGT	B	17.76	0.07
58927.60	TESS		14.36	0.00
58927.62	TESS		14.35	0.00
58927.64	TESS		14.29	0.00
58927.67	TESS		14.31	0.00
58927.69	TESS		14.30	0.00
58927.71	TESS		14.25	0.00

\*This is presented for form and content. The full table is available in the online version of the published ApJ paper.

Table 4.4. B2 1420+32 Fermi LAT lightcurves

MJD	Bin size	Flux	Uncertainty
54772.66	2 months	0.72	0.05
54832.66	2 months	0.29	0.30
54892.66	2 months	1.22	0.58
55012.66	2 months	0.23	0.05
55072.66	2 months	1.24	1.06
55132.66	2 months	0.81	0.55
57504.0	3 days	5.57	0.48
57543.0	3 days	9.86	1.82
57567.0	3 days	7.41	5.35
57585.0	3 days	7.79	3.71
57609.0	3 days	6.06	3.70
57615.0	3 days	2.12	1.45
58104.5	1 day	12.5	11.5
58106.5	1 day	28.1	13.0
58110.5	1 day	19.5	11.3
58112.5	1 day	11.4	4.83
58114.5	1 day	10.6	4.98
58115.5	1 day	13.8	7.08
58927.86	0.5 day	53.8	16.4
58928.36	0.5 day	40.4	19.2
58928.86	0.5 day	37.1	11.0
58929.36	0.5 day	49.4	3.63
58929.86	0.5 day	55.4	15.9
58930.36	0.5 day	32.3	14.9

\*This is presented for form and content. The full table is available in the online version of the published ApJ paper.

\*The flux is in the units of  $10^{-8}$  photon  $\text{cm}^{-2} \text{s}^{-1}$ .



## Chapter 5

# The Swift AGN and Cluster Survey: Detecting X-ray Galaxy Clusters

### 5.1 Introduction

Galaxy clusters are the largest and the most massive gravitational structures in the universe. They constitute the high-density peaks of the cosmic web and are connected through the network of filamentary structures which surround the large underdense regions called cosmic voids. More detailed description of galaxy clusters is provided in Section 1. X-ray surveys are very useful and powerful tools to detect and understand extragalactic X-ray emitting sources, such as galaxy clusters, groups, starburst galaxies, and AGN. The X-ray emission comes from the ICM which contains majority of the baryonic mass of a galaxy cluster (via the thermal brehmsstrahlung process). X-ray surveys have the advantage of being complete and almost pure surveys, and they are not affected by projection effects. X-ray scaling relations tightly correlate X-ray observables, such as temperature and lumionsity, with total cluster mass. However, these surveys may be biased toward relaxed clusters and rich clusters with higher ICM mass.

Serendipitous surveys, like *Chandra*, *ROSAT*, and *XMM-Newton*, use a large number of observational pointings that are originally intended to detect different sources in the sky to search for clusters (Dai et al. 2015). These surveys are economical and efficiently create large datasets which can be utilized to find extended X-ray sources. However, since these surveys utilize pointed observations for a variety of objects, the selection effects can be difficult to reconcile. Wide-area all-sky surveys play an important role in studying large-scale structure population and their abundance

and distribution in the universe, and cosmology at low redshifts (Fassbender et al. 2011; Dai et al. 2015), as well in the detection of the low-redshift, bright AGN population. Surveys, such as the *ROSAT* All-Sky Survey, have detected over a 100,000 X-ray sources which include supernova remnants, AGN, quasars, neutron stars, and galaxy cluster (Voges et al. 1999). On the other hand, deep, pencil-beam surveys have allowed for the investigation of high-redshift and obscured AGN (Lansbury et al. 2017). While shallow surveys efficiently search for low-redshift, massive galaxy clusters, deep pointed surveys are volume limited and probe redshifts where massive clusters are rare (Dai et al. 2015). This gives rise to the need for medium-deep surveys, which can cover wide areas of the sky to characterize cluster population and are sensitive enough to search for intermediate-redshift clusters and groups of galaxies.

*Swift* (Gehrels et al. 2005; Burrows et al. 2005) is a space-based multi-wavelength survey whose primary goal is to detect and study gamma-ray bursts (GRBs). *Swift* uses three instruments for gamma-ray, X-ray, and ultraviolet/optical bands. The Burst Alert telescope (BAT) is used to detect the GRB. The X-ray telescope (XRT) and the ultraviolet/optical telescope (UVOT) are used to look at the afterglow. It is a serendipitous, intermediate-depth survey and has observed GRBs at a rate of about 100 bursts per year since its launch in November 2004. XRT operates in the energy range 0.2-10 keV at an angular resolution of 18 arcseconds. The imager's effective area is 120 cm<sup>2</sup> at 1.5 keV and a field of view of 23.6 × 23.6 arcminutes. The sensitivity of the detector is  $2 \times 10^{-14}$  erg s<sup>-1</sup> cm<sup>-2</sup> in 10<sup>4</sup> s (Hill et al. 2004; D'Elia et al. 2013). XRT data is available in two modes: photon counting and windowed timing modes. The XRT observations span over an area of  $\sim 125$  square degrees in the sky (Dai et al. 2015). The GRB fields provide a very useful data set to detect extended X-ray sources in soft X-ray energy range for medium-depth, and is complementary to surveys, such as *ROSAT* and *Chandra*.

The luminosity functions and number counts of galaxy clusters obtained from such

surveys are useful cosmological probes to constrain the halo mass function and the redshift distribution of the dark matter halos. The detection of rich galaxy clusters ( $M \sim 10^{14} M_{\odot}$ ) at higher redshifts requires large survey areas and high sensitivity (Takey et al. 2016; Koulouridis et al. 2021).

The goal of this project is to construct a galaxy cluster catalog as an extended catalog to the Swift AGN and Cluster Survey. I. (Dai et al. 2015). The catalog will present the number count of galaxy clusters detected in the *Swift* survey, and other cluster properties – the flux, IR colors from *WISE* (W1, W2, W3, and W4).

This chapter is divided into the following sections: we describe the data, the data reduction, and the source detection process in Section 2, and in Section 3, we discuss the next steps that need to be taken in the analysis process.

## 5.2 Data Reduction and Source Detection

All the data was downloaded from the HEASARC Swift archive. The SWIFT-XRT data before 2017 December was used for this paper. This included all the XRT data from November 2004 to December 2017 in the form of FITS files, where the file’s name starts with sw as part of the labeling convention. The structure for the downloaded data includes the xrt, auxil, and log directories. We used HEASoft version 6.25 to reprocess all the data and the corresponding calibration files were downloaded and installed along with the HEASoft software. *Swift* CALDB files (version XRT 20210915) were used for calibration. The XRT data is available in the windowed timing mode, which preserves the one-dimensional image by covering the central 8 arcmin of the field of view. The photon counting mode preserves the imaging and spectroscopic resolution, but is limited in the time resolution. The time resolution in this mode is 2.51 seconds. We used the XRT files stored in the photon counting mode for our analysis.

Next, HEASoft tool *xrtpipeline* was used to reprocess the data and generate clean event files. In the first step, the file was calibrated, the bad pixels were removed, the coordinates were transformed, the events were time tagged, the events were reconstructed, the PHA (pulse height amplitude) and PI (pulse invariant) values were determined, and the partially exposed pixels were removed (Capalbi et al. 2005; Godet et al. 2009). In the next step, the calibrated files were screened based on various input parameters. Task *xrtscreen* cleaned the data to produce the clean event files, in addition to the lightcurve, spectra, and arfs for the target points in the PC mode. The exposure maps for the PC mode event files were created using the *xrteexpomap tool* (version 0.2.7) in HEASoft. The tool *expomap* utilized information, like bad pixels, attitude files, and telescope vignetting to generate these maps. All the observations were binned into two-dimensional  $20 \times 20$  square arcmin regions in the sky, based on their coordinates (right ascension and declination). We stacked all the processed files and exposure maps in each cluster region to increase the signal-to-noise ratio. The exposure times were also added to calculate the total exposure time for each bin. For further analysis, we selected the bins which had exposure time  $> 10000$  seconds. We used the merged event files to create the final images in the total X-ray band (2-10 keV). To detect sources, we used the package *wavdetect* (Freeman et al. 2002) from the *Chandra Interactive Analysis of Observations (CIAO)*. *wavdetect* is a wavelet-based algorithm commonly used for X-ray data from *ROSAT* and *Chandra* to detect sources. To detect sources with this algorithm, a wavelet function is defined and the correlation of the data with the wavelet function is calculated. Next, the image pixels with correlation value larger than a pre-set critical value are selected, in addition to characterizing the local background in each pixel.

For further analysis, we made a cut for the photon count to select sources with enough number of photons for a significant detection. We set the threshold at photon count  $> 20$ . We chose this cut to distinguish point sources from extended sources

with a significance of greater than  $4\sigma$  (Dai et al. 2015) for low-redshift photons. For clusters at a higher redshift, we would need a higher count of photons as the angular size would decrease. Based on this criteria, our sample consisted of 21015 point and extended sources. We calculated a  $4\sigma$  size cut for each off-axis bin (see Figure 5.4) to separate the point and extended sources in each bin. We applied the same  $4\sigma$  size cut for each bin for the signal-to-noise ratio (see Figure 5.5). Then we combined the extended sources whose size satisfied both the off-axis angle and the signal-to-noise ratio thresholds. To eliminate unrealistic sources with very large sizes that may have been selected by *wavdetect*, but suffer issues, such as being too close to the image boundary, we made a source size cut of  $R_c < 25$  pixels and got 855 total band extended cluster candidates.

### 5.3 Extended Source Analysis and Discussion

The next step in the analysis is to investigate these 855 extended sources selected in the previous step visually. We need to look at each field and inspect the clusters selected by the algorithm. This will be done to eliminate cluster candidates which have been incorrectly selected due to one or more factors. We will then correct the fluxes of the candidates by adding the Galactic absorption factor and using a  $\beta$ -model to calculate the total flux of the cluster at the average cluster redshift, with  $\beta = 0.6$  and  $R_c = 0.1$  Mpc for typical clusters of mass  $2 \times 10^{14} M_\odot$  (Dai et al. 2015).

The extragalactic X-ray sources most commonly fall under three categories: AGN, GRBs, and galaxy clusters. We will eliminate GRB sources from our candidate list by matching them against the existing XRT database. Next, the extended sources will be matched against the Meta Catalog of X-ray Clusters (Piffaretti et al. 2011) and the *WISE* database. The X-ray catalog of galaxy clusters under the SACS will be an extension to the SACS catalog from Dai et al. (2015). The catalog will contain

the number count of clusters, in addition to the source flux and the background count rate.

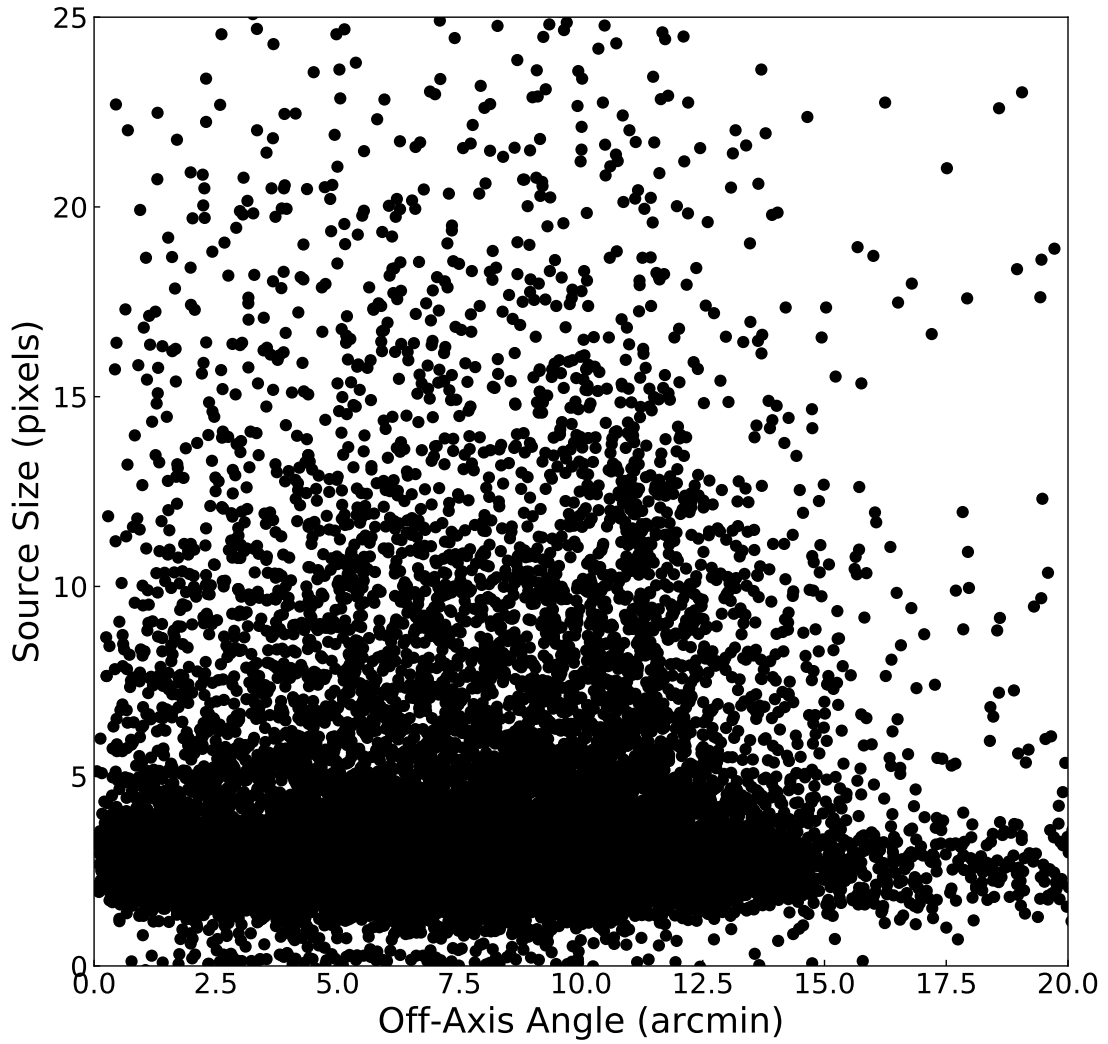


Fig. 5.1.— Core radius in pixels as a function of off-axis angle for point and extended sources which were selected using the criteria of photon count  $> 20$  and off-axis angle  $< 20$  arcmin.

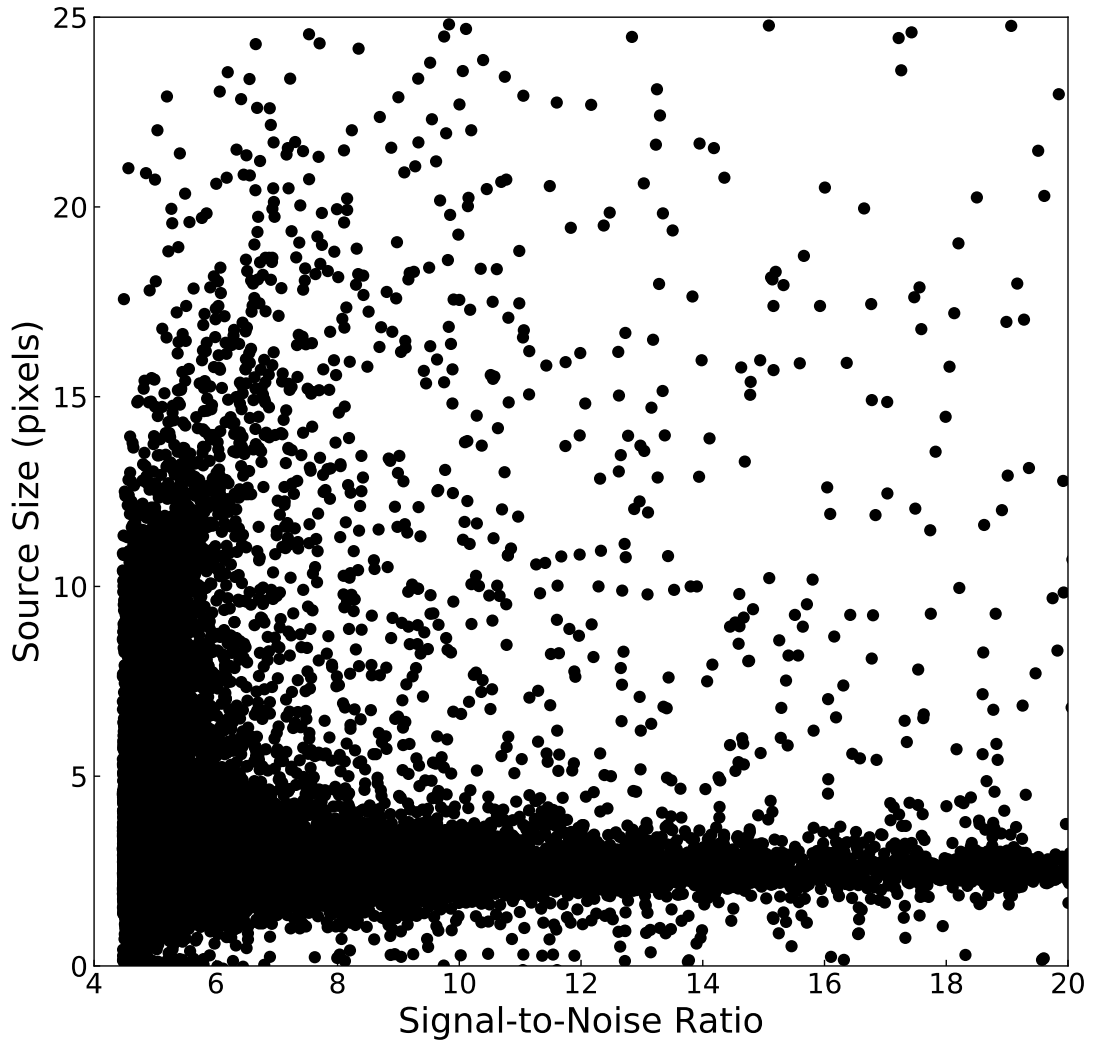


Fig. 5.2.— Core radius in pixels as a function of signal-to-noise ratio for point and extended which were selected using the criteria of photon count  $> 20$  and signal-to-noise ratio  $< 20$ .



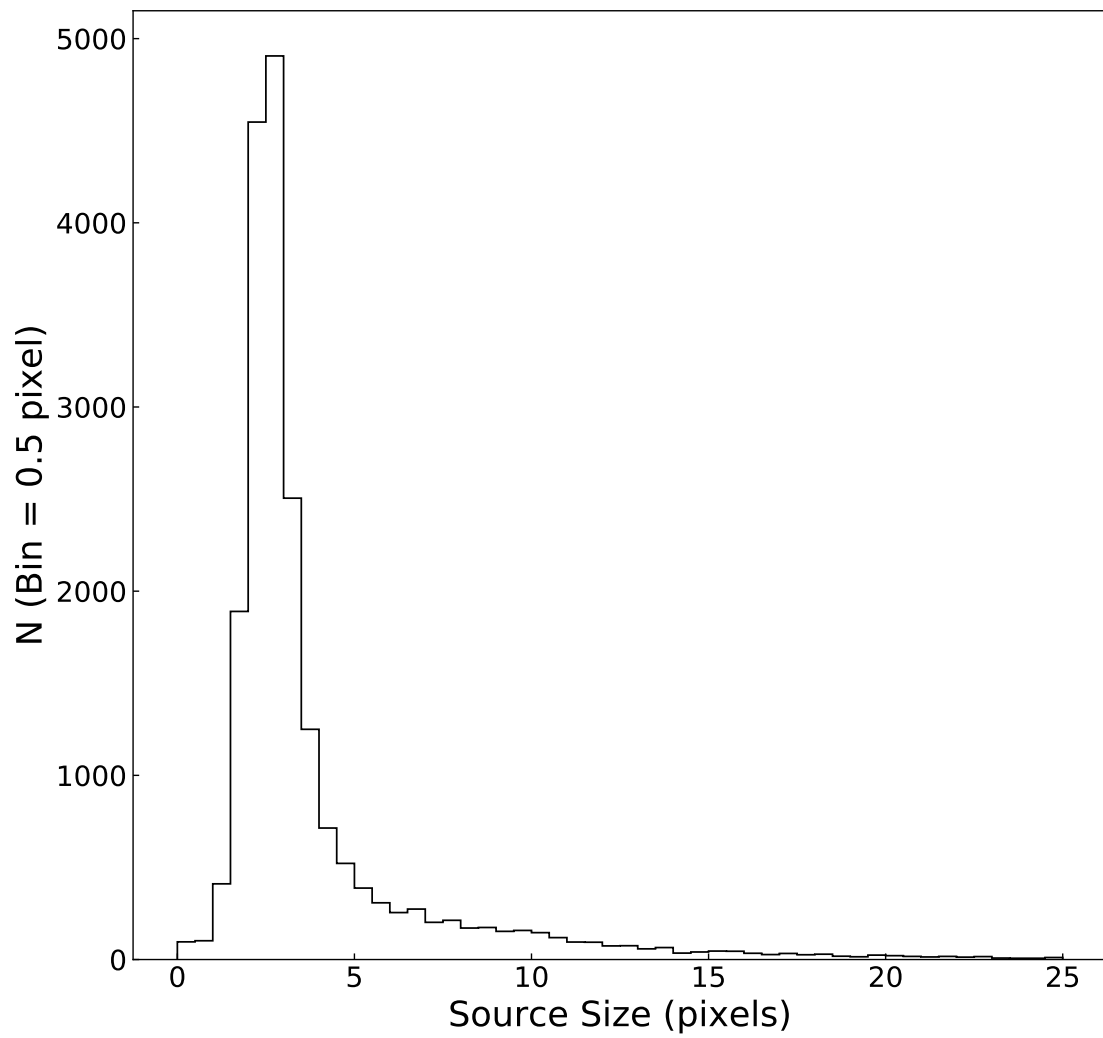


Fig. 5.3.— Histogram of the core radii for point and extended sources with size  $< 25$  pixels.

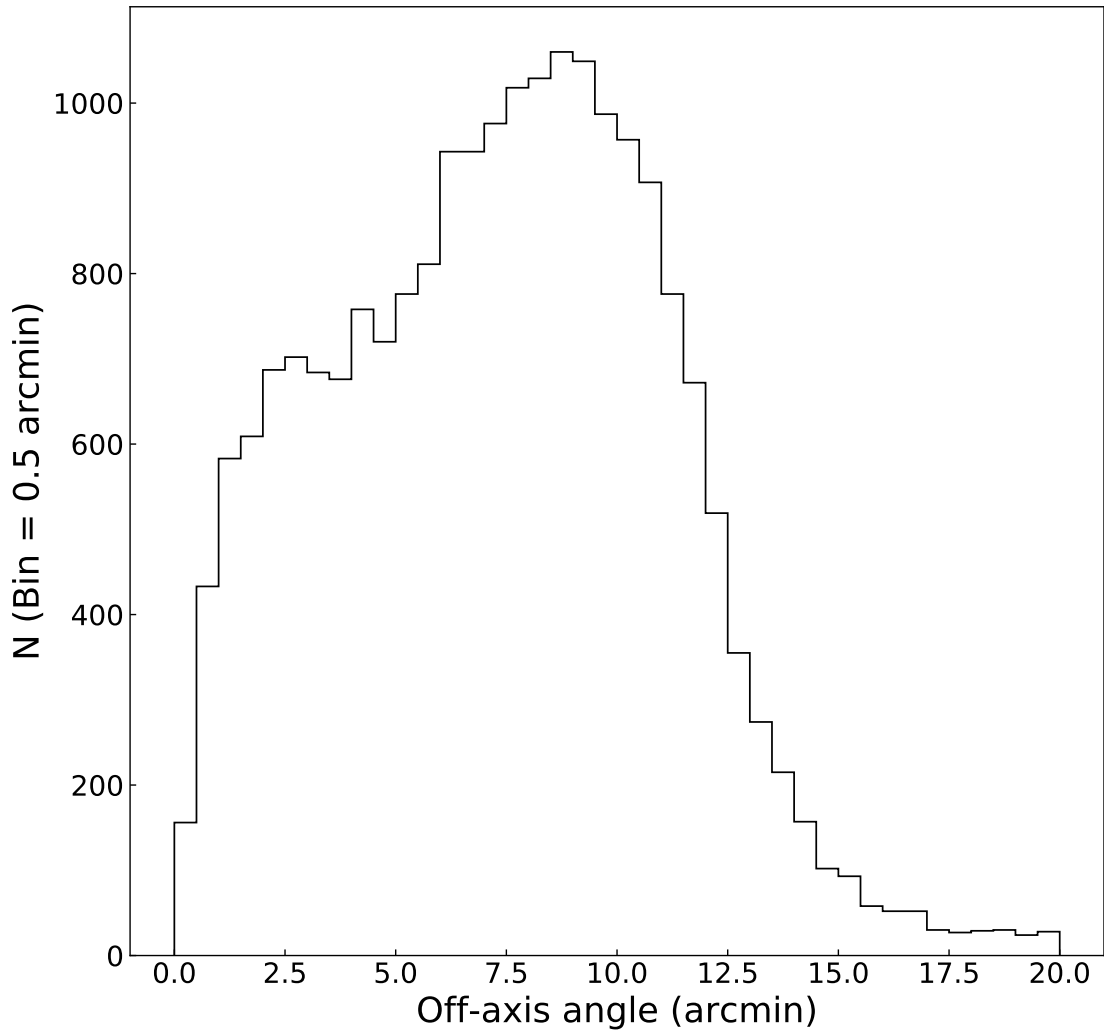


Fig. 5.4.— Histogram of the off-axis angles for point and extended sources with angle  $< 20$  arcmin.

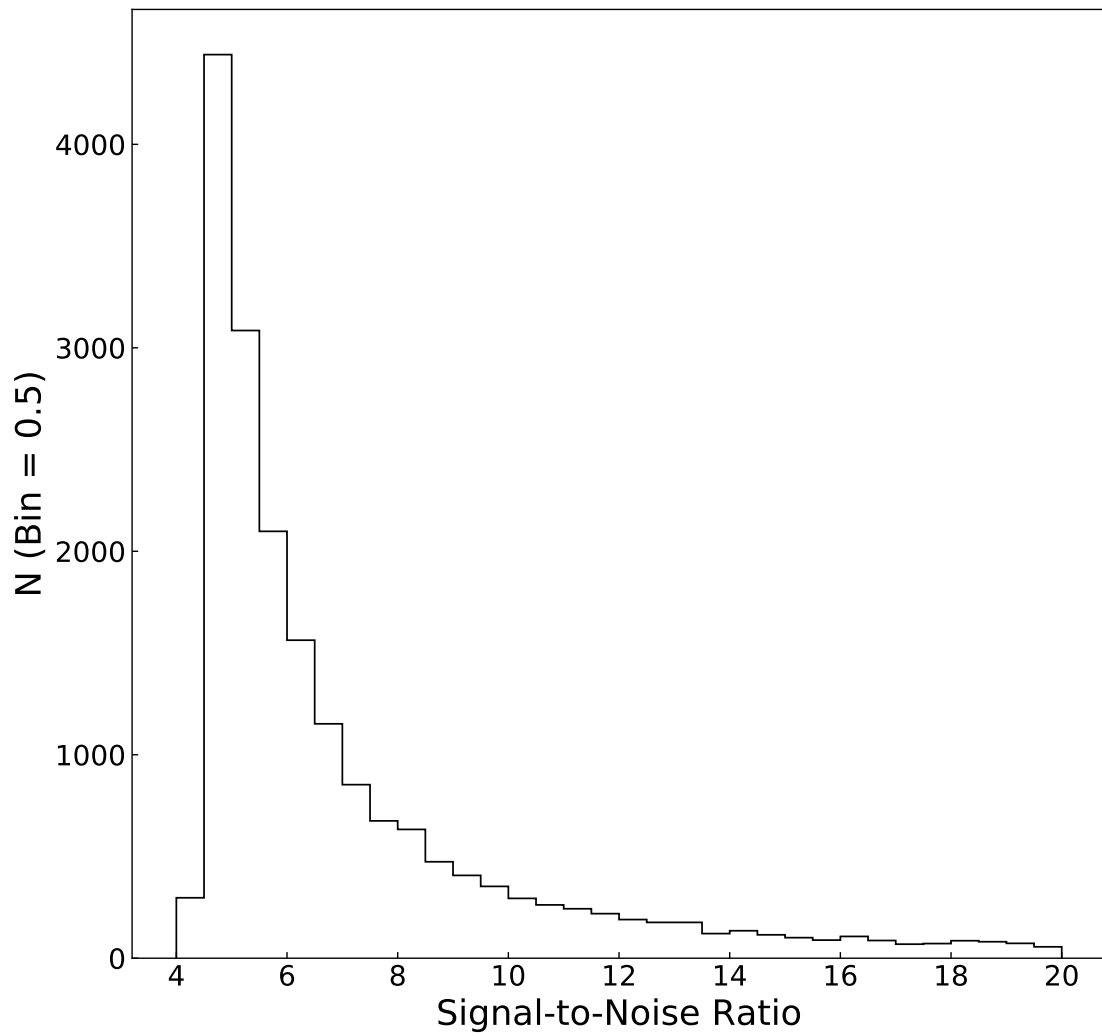


Fig. 5.5.— Histogram of signal-to-noise ratio point and extended sources with ratio  $< 20$ .

# Chapter 6

## Conclusion

### 6.1 Chapter Summaries

In Chapter 2, we presented our work on investigating AGN fraction in one of the largest samples of X-ray selected clusters from the *ROSAT* survey and their immediate surrounding field regions below  $z < 0.5$ . We found lower average AGN fraction in clusters ( $2.37 \pm 0.39$ )% than for the fields ( $5.12 \pm 0.16$ )%. The lower AGN fractions in clusters were measured, after dividing the clusters into five redshift intervals between 0.0 and 0.5, in each redshift interval, and we found an increase in the fraction for both cluster and field galaxies with redshift below  $z < 0.5$ , which clearly indicates an environment and redshift dependence. We further divided the clusters into low-mass and high-mass objects using a mass cut at  $\log_{10}(M_{500}/M_{\odot}) = 13.5$ , finding comparable AGN fractions for both classifications, while a significantly higher AGN fraction in field. We also measured increasing AGN fractions with clustercentric distance for all redshift bins, further confirming the environmental dependence of AGN activities. In addition, we did not find an obvious trend between AGN fraction and SDSS  $M_r$  absolute magnitudes among different redshift bins.

In Chapter 3, we investigated AGN fraction in one of the largest samples of optically selected cosmic voids from SDSS Data Release 12 for redshift range 0.2–0.7 for moderately bright and bright AGN. We separated inner and outer void regions based on the void size, given by its effective void radius. We found higher average fractions in the inner voids ( $4.9 \pm 0.7$ )% than for their outer counterparts ( $3.1 \pm 0.1$ )% at  $z > 0.42$ , which clearly indicates an environmental dependence. This conclusion was confirmed upon further separating the data in narrower void-centric distance

bins and measured a significant decrease in AGN activity from inner to outer voids for  $z > 0.42$ . At low redshifts ( $z < 0.42$ ), we found very weak dependence on the environment for the inner and outer regions for two out of three bins. We argue that the higher fraction in low-density regions close to void centers relative to their outer counterparts observed in the two higher redshift bins suggests that there may occur more efficient galaxy interactions at one-to-one level in voids which may be suppressed in denser environments due to higher velocity dispersions. It could also indicate less prominent ram pressure stripping in voids or some intrinsic host or void environment properties.

In Chapter 4, we discussed in detail the multi-wavelength photometric and spectroscopic monitoring observations of the blazar, B2 1420+32, focusing on its outbursts in 2018-2020. Multi-epoch spectra showed that the blazar exhibited large scale spectral variability in both its continuum and line emission, accompanied by dramatic gamma-ray and optical variability by factors of up to 40 and 15, respectively, on week to month timescales. Over the last decade, the gamma-ray and optical fluxes increased by factors of 1500 and 100, respectively. B2 1420+32 was an FSRQ with broad emission lines in 1995. Following a series of flares starting in 2018, it transitioned between BL Lac and FSRQ states multiple times, with the emergence of a strong Fe pseudo continuum. Two spectra also contain components that can be modeled as single-temperature black bodies of 12,000 and 5,200 K. Such a collection of “changing look” features has never been observed previously in a blazar. We measured the  $\gamma$ -ray-optical and the inter-band optical lags implying that the emission region separations were less than 800 and 130 gravitational radii respectively. Since most emission line flux variations, except the Fe continuum, are within a factor of 2–3, the transitions between FSRQ and BL Lac classifications are mainly caused by the continuum variability. The large Fe continuum flux increase suggests the occurrence of dust sublimation releasing more Fe ions in the central engine and an energy

transfer from the relativistic jet to sub-relativistic emission components.

Finally, in Chapter 5, we discussed the Swift AGN and Cluster Survey project. The chapter detailed the data reduction and initial analysis steps and discussed the next steps in building the cluster catalog. The goal of this project is to create a galaxy cluster catalog as an extended catalog to the Swift AGN and Cluster Survey. I. (Dai et al. 2015). The catalog will present the number count of galaxy clusters detected in the *Swift* survey, and other cluster properties – the flux and infrared colors from *WISE* (W1, W2, W3, and W4).

## References

- Abazajian, K., Adelman-McCarthy, J. K., Agüeros, M. A., et al. 2003, *AJ*, 126, 2081. doi:10.1086/378165
- Abbott, T. M. C., Allam, S., Andersen, P., et al. 2019, *ApJ*, 872, L30. doi:10.3847/2041-8213/ab04fa
- Abell, G. O. 1958, *ApJS*, 3, 211. doi:10.1086/190036
- Abolfathi, B., Aguado, D. S., Aguilar, G., et al. 2018, *ApJS*, 235, 42
- Abraham, R. G., McHardy, I. M., & Crawford, C. S. 1991, *MNRAS*, 252, 482. doi:10.1093/mnras/252.4.482
- Alam, S., Albareti, F. D., Allende Prieto, C., et al. 2015, *ApJS*, 219, 12. doi:10.1088/0067-0049/219/1/12
- Alam, S., Peacock, J. A., Farrow, D. J., et al. 2021, *MNRAS*, 503, 59. doi:10.1093/mnras/stab409
- Aharonian, F., Akhperjanian, A. G., Bazer-Bachi, A. R., et al. 2007, *ApJ*, 664, L71
- Ai, Y., Dou, L., Yang, C., et al. 2020, *ApJ*, 890, L29. doi:10.3847/2041-8213/ab7306
- Albert, C. E., White, R. A., & Morgan, W. W. 1977, *ApJ*, 211, 309. doi:10.1086/154935
- Alberts, S., Pope, A., Brodwin, M., et al. 2016, *ApJ*, 825, 72
- Aleksić, J., Ansoldi, S., Antonelli, L. A., et al. 2014, *Science*, 346, 1080
- Álvarez Crespo, N., Masetti, N., Ricci, F., et al. 2016, *AJ*, 151, 32
- Alexander, D. M., & Hickox, R. C. 2012, *New A Rev.*, 56, 93
- Alonso, M. S., Lambas, D. G., Tissera, P., et al. 2007, *MNRAS*, 375, 1017
- Andreon, S. 2018, *A&A*, 617, A53. doi:10.1051/0004-6361/201832627
- Antonucci, R. R. J. & Miller, J. S. 1985, *ApJ*, 297, 621. doi:10.1086/163559
- Antonucci, R. 1993, *ARA&A*, 31, 473. doi:10.1146/annurev.aa.31.090193.002353
- Aretxaga, I., Jouguet, B., Kunth, D., et al. 1999, *ApJ*, 519, L123. doi:10.1086/312114
- Argudo-Fernández, M., Lacerna, I., & Duarte Puertas, S. 2018, *A&A*, 620, A113
- Assef, R. J., Kochanek, C. S., Brodwin, M., et al. 2008, *ApJ*, 676, 286
- Assef, R. J., Kochanek, C. S., Brodwin, M., et al. 2010, *ApJ*, 713, 970
- Atwood, W. B., Abdo, A. A., Ackermann, M., et al. 2009, *ApJ*, 697, 1071

- Axon, D. J., Capetti, A., Fanti, R., et al. 2000, *AJ*, 120, 2284. doi:10.1086/316838
- Baade, W. & Mayall, N. U. 1951, *Problems of Cosmical Aerodynamics*, 165
- Bahcall, N. A. & Cen, R. 1993, *ApJ*, 407, L49. doi:10.1086/186803
- Bahcall, N. A. 1996, astro-ph/9611148
- Bahcall, N. A. & Oh, S. P. 1996, *ApJ*, 462, L49. doi:10.1086/310041
- Baldi, R. D., Rodríguez Zaurín, J., Chiaberge, M., et al. 2019, *ApJ*, 870, 53
- Bamford, S. P., Nichol, R. C., Baldry, I. K., et al. 2009, *MNRAS*, 393, 1324. doi:10.1111/j.1365-2966.2008.14252.x
- Bardeen, J. M., Steinhardt, P. J., & Turner, M. S. 1983, *Phys. Rev. D*, 28, 679. doi:10.1103/PhysRevD.28.679
- Barthel, P. D. 1989, *ApJ*, 336, 606. doi:10.1086/167038
- Baskin, A. & Laor, A. 2018, *MNRAS*, 474, 1970. doi:10.1093/mnras/stx2850
- Bassett, B. & Hlozek, R. 2010, *Dark Energy: Observational and Theoretical Approaches*, 246
- Baumann, O., Röser, H.-J., Tschamber, C., et al. 2002, *Tracing Cosmic Evolution with Galaxy Clusters*, 268, 333
- Begelman, M. C., Blandford, R. D., & Rees, M. J. 1984, *Reviews of Modern Physics*, 56, 255. doi:10.1103/RevModPhys.56.255
- Begelman, M. C. 1985, *Astrophysics of Active Galaxies and Quasi-Stellar Objects*, 411
- Begelman, M. C. 1989, *Accretion Disks and Magnetic Fields in Astrophysics*, 156, 255. doi:10.1007/978-94-009-2401-7\_27
- Bellovary, J., Brooks, A., Volonteri, M., et al. 2013, *ApJ*, 779, 136. doi:10.1088/0004-637X/779/2/136
- Bertschinger, E. 1998, *ARA&A*, 36, 599. doi:10.1146/annurev.astro.36.1.599
- Bhattacharya, S., Habib, S., Heitmann, K., et al. 2013, *ApJ*, 766, 32. doi:10.1088/0004-637X/766/1/32
- Bianchi, S., Guainazzi, M., Matt, G., et al. 2005, *A&A*, 442, 185
- Birkinshaw, M. 1999, *Phys. Rep.*, 310, 97. doi:10.1016/S0370-1573(98)00080-5
- Blackburne, J. A., Pooley, D., Rappaport, S., et al. 2011, *ApJ*, 729, 34. doi:10.1088/0004-637X/729/1/34
- Blandford, R. D. 1990, *Active Galactic Nuclei*, 161



- Blandford, R., Meier, D., & Readhead, A. 2019, *ARA&A*, 57, 467. doi:10.1146/annurev-astro-081817-051948
- Blanton, M. R., Eisenstein, D., Hogg, D. W., et al. 2005, *ApJ*, 629, 143. doi:10.1086/422897
- Blanton, M. R. & Moustakas, J. 2009, *ARA&A*, 47, 159. doi:10.1146/annurev-astro-082708-101734
- Bluck, A. F. L., Mendel, J. T., Ellison, S. L., et al. 2014, *MNRAS*, 441, 599. doi:10.1093/mnras/stu594
- Blundell, K. M. & Beasley, A. J. 1998, *MNRAS*, 299, 165. doi:10.1046/j.1365-8711.1998.01752.x
- Böhringer, H., Voges, W., Huchra, J. P., et al. 2000, *ApJS*, 129, 435
- Böhringer, H., Schuecker, P., Guzzo, L., et al. 2004, *A&A*, 425, 367
- Böhringer, H., Schuecker, P., Pratt, G. W., et al. 2007, *A&A*, 469, 363. doi:10.1051/0004-6361:20066740
- Bond, J. R., Kofman, L., & Pogosyan, D. 1996, *Nature*, 380, 603. doi:10.1038/380603a0
- Bonnoli, G., Ghisellini, G., Foschini, L., et al. 2011, *MNRAS*, 410, 368
- Borgani, S., Plionis, M., Coles, P., et al. 1995, *MNRAS*, 277, 1191. doi:10.1093/mnras/277.4.1191
- Bos, E. G. P., van de Weygaert, R., Dolag, K., et al. 2012, *MNRAS*, 426, 440. doi:10.1111/j.1365-2966.2012.21478.x
- Boselli, A., Voyer, E., Boissier, S., et al. 2014, *A&A*, 570, A69. doi:10.1051/0004-6361/201424419
- Bregman, J. N., Glassgold, A. E., Huggins, P. J., et al. 1986, *ApJ*, 301, 698
- Brotherton, M. S., Singh, V., & Runnoe, J. 2015, *MNRAS*, 454, 3864
- Brown, T. M., Baliber, N., Bianco, F. B., et al. 2013, *PASP*, 125, 1031
- Bruton, S. T., Dai, X., Guerras, E., et al. 2020, *MNRAS*, 491, 2496. doi:10.1093/mnras/stz2876
- Bufanda, E., Hollowood, D., Jeltema, T. E., et al. 2017, *MNRAS*, 465, 2531
- Burbidge, G. R. 1956, *ApJ*, 124, 416. doi:10.1086/146237
- Burenin, R. A., Vikhlinin, A., Hornstrup, A., et al. 2007, *ApJS*, 172, 561
- Burg, R., Giacconi, R., Forman, W., et al. 1994, *ApJ*, 422, 37. doi:10.1086/173701
- Burke, D. J., Collins, C. A., Sharples, R. M., et al. 2003, *MNRAS*, 341, 1093

- Burrows, D. N., Hill, J. E., Nousek, J. A., et al. 2005, *Space Sci. Rev.*, 120, 165. doi:10.1007/s11214-005-5097-2
- Byram, E. T., Chubb, T. A., & Friedman, H. 1966, *Science*, 152, 66. doi:10.1126/science.152.3718.66
- Cantalupo, S., Arrigoni-Battaia, F., Prochaska, J. X., et al. 2014, *Nature*, 506, 63. doi:10.1038/nature12898
- Capalbi, M., Perri, M., Saija, B., Tamburelli, F., Angelini, L, et al. 2005, “The SWIFT XRT Data Reduction Guide”
- Capetti, A., Verdoes Kleijn, G., & Chiaberge, M. 2005, *A&A*, 439, 935
- Carrasco, L., Escobedo, G., Recillas, E., et al. 2019, *The Astronomer’s Telegram*, 13028
- Ceccarelli, L., Padilla, N. D., Valotto, C., et al. 2006, *MNRAS*, 373, 1440. doi:10.1111/j.1365-2966.2006.11129.x
- Ceccarelli, L., Paz, D., Lares, M., et al. 2013, *MNRAS*, 434, 1435. doi:10.1093/mnras/stt1097
- Chiang, C.-Y., Goto, T., Hashimoto, T., et al. 2019, *PASJ*, 71, 31
- Cielo, S., Bieri, R., Volonteri, M., et al. 2018, *MNRAS*, 477, 1336. doi:10.1093/mnras/sty708
- Ciprini, S. 2018, *The Astronomer’s Telegram*, 12277
- Ciprini, S. & Cheung, C. C. 2020, *The Astronomer’s Telegram*, 13382
- Ciotti, L. & Ostriker, J. P. 1997, *ApJ*, 487, L105. doi:10.1086/310902
- Coles, P. & Lucchin, F. 2002, *Cosmology: The Origin and Evolution of Cosmic Structure*, Second Edition, by Peter Coles, Francesco Lucchin, pp. 512. ISBN 0-471-48909-3. Wiley-VCH, July 2002., 512
- Constantin, A., Hoyle, F., & Vogeley, M. S. 2008, *ApJ*, 673, 715. doi:10.1086/524310
- Corbett, E. A., Robinson, A., Axon, D. J., et al. 2000, *MNRAS*, 319, 685
- Couch, W. J., Barger, A. J., Smail, I., et al. 1998, *ApJ*, 497, 188
- Croton, D. J., Springel, V., White, S. D. M., et al. 2006, *MNRAS*, 367, 864
- Cruddace, R., Voges, W., Böhringer, H., et al. 2002, *ApJS*, 140, 239
- Czerny, B. & Hryniewicz, K. 2011, *A&A*, 525, L8. doi:10.1051/0004-6361/201016025
- D’Ammando, F., Raiteri, C. M., Villata, M., et al. 2019, *MNRAS*, 490, 5300
- D’Elia, V., Perri, M., Puccetti, S., et al. 2013, *A&A*, 551, A142. doi:10.1051/0004-6361/201220863

- Dai, X., Bregman, J. N., Kochanek, C. S., et al. 2010, *ApJ*, 719, 119. doi:10.1088/0004-637X/719/1/119
- Dai, X., Griffin, R. D., Kochanek, C. S., et al. 2015, *ApJS*, 218, 8. doi:10.1088/0067-0049/218/1/8
- Davé, R., Oppenheimer, B. D., & Sivanandam, S. 2008, *MNRAS*, 391, 110. doi:10.1111/j.1365-2966.2008.13906.x
- David, L. P., Slyz, A., Jones, C., et al. 1993, *ApJ*, 412, 479. doi:10.1086/172936
- Dawson, K. S., Schlegel, D. J., Ahn, C. P., et al. 2013, *AJ*, 145, 10. doi:10.1088/0004-6256/145/1/10
- Dekel, A. & Rees, M. J. 1994, *ApJ*, 422, L1. doi:10.1086/187197
- Dekel, A., Sari, R., & Ceverino, D. 2009, *ApJ*, 703, 785
- De Martino, I. & Atrio-Barandela, F. 2016, *MNRAS*, 461, 3222. doi:10.1093/mnras/stw1493
- Di Matteo, T., Croft, R. A. C., Springel, V., et al. 2003, *ApJ*, 593, 56
- Di Matteo, T., Springel, V., & Hernquist, L. 2005, *Nature*, 433, 604
- Di Matteo, T., Croft, R. A. C., Feng, Y., et al. 2017, *MNRAS*, 467, 4243. doi:10.1093/mnras/stx319
- Dolag, K., Schindler, S., Govoni, F., et al. 2001, *A&A*, 378, 777. doi:10.1051/0004-6361:20011219
- Donato, D., Ghisellini, G., Tagliaferri, G., et al. 2001, *A&A*, 375, 739
- Done, C. & Krolik, J. H. 1996, *ApJ*, 463, 144. doi:10.1086/177230
- Drake, A. J., Djorgovski, S. G., Mahabal, A., et al. 2009, *ApJ*, 696, 870
- Dressler, A. 1980, *ApJ*, 236, 351. doi:10.1086/157753
- Dressler, A. 1984, *ARA&A*, 22, 185. doi:10.1146/annurev.astro.22.1.185
- Drinkwater, M. J., Jurek, R. J., Blake, C., et al. 2010, *MNRAS*, 401, 1429. doi:10.1111/j.1365-2966.2009.15754.x
- Eastman, J., Martini, P., Sivakoff, G., et al. 2007, *ApJ*, 664, L9
- Ebeling, H., Stephenson, L. N., & Edge, A. C. 2014, *ApJ*, 781, L40
- Eckert, D., Gaspari, M., Gastaldello, F., et al. 2021, *Universe*, 7, 142. doi:10.3390/universe7050142
- Eckmiller, H. J., Hudson, D. S., & Reiprich, T. H. 2011, *A&A*, 535, A105. doi:10.1051/0004-6361/201116734

- Edelson, R. A. & Malkan, M. A. 1987, *ApJ*, 323, 516
- Edelson, R. A., Malkan, M. A., & Rieke, G. H. 1987, *ApJ*, 321, 233. doi:10.1086/165627
- Edge, A. C. & Stewart, G. C. 1991, *MNRAS*, 252, 428. doi:10.1093/mnras/252.3.428
- Ehlert, S., von der Linden, A., Allen, S. W., et al. 2014, *MNRAS*, 437, 1942
- Einasto, M., Saar, E., Martínez, V. J., et al. 2008, *ApJ*, 685, 83. doi:10.1086/590374
- Eisenstein, D. J., Weinberg, D. H., Agol, E., et al. 2011, *AJ*, 142, 72. doi:10.1088/0004-6256/142/3/72
- Eke, V. R., Navarro, J. F., & Frenk, C. S. 1998, *ApJ*, 503, 569. doi:10.1086/306008
- Elitzur, M. 2006, *New A Rev.*, 50, 728. doi:10.1016/j.newar.2006.06.027
- Elitzur, M. 2012, *ApJ*, 747, L33. doi:10.1088/2041-8205/747/2/L33
- Ellison, S. L., Viswanathan, A., Patton, D. R., et al. 2019, *MNRAS*, 487, 2491
- Elvis, M. 2000, *ApJ*, 545, 63. doi:10.1086/317778
- Elyiv, A. A., Karachentsev, I. D., Karachentseva, V. E., et al. 2013, *Astrophysical Bulletin*, 68, 1. doi:10.1134/S199034131301001X
- Ettori, S., Rasia, E., Fabjan, D., et al. 2012, *MNRAS*, 420, 2058. doi:10.1111/j.1365-2966.2011.20318.x
- Ettori, S. 2015, *MNRAS*, 446, 2629. doi:10.1093/mnras/stu2292
- Evrard, A. E., Metzler, C. A., & Navarro, J. F. 1996, *ApJ*, 469, 494. doi:10.1086/177798
- Faber, S. M. & Gallagher, J. S. 1979, *ARA&A*, 17, 135. doi:10.1146/annurev.aa.17.090179.001031
- Fabian, A. C. & Rees, M. J. 1995, *MNRAS*, 277, L55. doi:10.1093/mnras/277.1.L55
- Fabian, A. C. 1999, *Proceedings of the National Academy of Science*, 96, 4749. doi:10.1073/pnas.96.9.4749
- Falcke, H. & Biermann, P. L. 1995, *A&A*, 293, 665
- Falomo, R., Pian, E., & Treves, A. 2014, *A&A Rev.*, 22, 73. doi:10.1007/s00159-014-0073-z
- Fan, X.-L., Wu, Q., & Liao, N.-H. 2018, *ApJ*, 861, 97. doi:10.3847/1538-4357/aac959
- Fanaroff, B. L. & Riley, J. M. 1974, *MNRAS*, 167, 31P. doi:10.1093/mnras/167.1.31P
- Fanidakis, N., Baugh, C. M., Benson, A. J., et al. 2011, *MNRAS*, 410, 53. doi:10.1111/j.1365-2966.2010.17427.x
- Fanti, R., Fanti, C., Schilizzi, R. T., et al. 1990, *A&A*, 231, 333

- Fassbender, R., Böhringer, H., Nastasi, A., et al. 2011, *New Journal of Physics*, 13, 125014. doi:10.1088/1367-2630/13/12/125014
- Fausnaugh, M. M., Grier, C. J., Bentz, M. C., et al. 2017, *ApJ*, 840, 97. doi:10.3847/1538-4357/aa6d52
- Ferrarese, L. & Merritt, D. 2000, *ApJ*, 539, L9. doi:10.1086/312838
- Fixsen, D. J. 2009, *ApJ*, 707, 916. doi:10.1088/0004-637X/707/2/916
- Fontanot, F., Macciò, A. V., Hirschmann, M., et al. 2015, *MNRAS*, 451, 2968
- Foschini, L. 2012, *Research in Astronomy and Astrophysics*, 12, 359. doi:10.1088/1674-4527/12/4/001
- Fossati, G., Maraschi, L., Celotti, A., et al. 1998, *MNRAS*, 299, 433
- Freeman, P., Doe, S., & Siemiginowska, A. 2001, *Proc. SPIE*, 4477, 76. doi:10.1117/12.447161
- Freeman, P. E., Kashyap, V., Rosner, R., et al. 2002, *ApJS*, 138, 185. doi:10.1086/324017
- García-González, J., Alonso-Herrero, A., Hönig, S. F., et al. 2017, *MNRAS*, 470, 2578. doi:10.1093/mnras/stx1361
- Garofalo, D., Singh, C. B., & Zack, A. 2018, *Scientific Reports*, 8, 15097. doi:10.1038/s41598-018-33532-6
- Garofalo, D., Singh, C. B., Walsh, D. T., et al. 2019, *Research in Astronomy and Astrophysics*, 19, 013. doi:10.1088/1674-4527/19/1/13
- Gaur, H., Gupta, A. C., Strigachev, A., et al. 2012, *MNRAS*, 425, 3002. doi:10.1111/j.1365-2966.2012.21583.x
- Gehrels, N., Chincarini, G., Giommi, P., et al. 2004, *ApJ*, 611, 1005
- Gehrels, N., Chincarini, G., Giommi, P., et al. 2005, *ApJ*, 621, 558. doi:10.1086/427409
- Geller, M. J. & Huchra, J. P. 1989, *Science*, 246, 897. doi:10.1126/science.246.4932.897
- Ghisellini, G., Celotti, A., Fossati, G., et al. 1998, *MNRAS*, 301, 451
- Ghisellini, G., Tavecchio, F., Foschini, L., et al. 2011, *MNRAS*, 414, 2674
- Giacconi, R., Murray, S., Gursky, H., et al. 1972, *ApJ*, 178, 281. doi:10.1086/151790
- Gierliński, M., Maciolek-Niedźwiecki, A., & Ebisawa, K. 2001, *MNRAS*, 325, 1253. doi:10.1046/j.1365-8711.2001.04540.x
- Gilbank, D. G., Bower, R. G., Castander, F. J., et al. 2004, *MNRAS*, 348, 551. doi:10.1111/j.1365-2966.2004.07335.x

- Gilman, D., Benson, A., Bovy, J., et al. 2022, MNRAS, 512, 3163.  
doi:10.1093/mnras/stac670
- Giommi, P., Padovani, P., Polenta, G., et al. 2012, MNRAS, 420, 2899
- Giodini, S., Lovisari, L., Pointecouteau, E., et al. 2013, Space Sci. Rev., 177, 247.  
doi:10.1007/s11214-013-9994-5
- Gioia, I. M., Henry, J. P., Maccacaro, T., et al. 1990, ApJ, 356, L35
- Gladders, M. D. & Yee, H. K. C. 2000, AJ, 120, 2148. doi:10.1086/301557
- Godet, O., Beardmore, A. P., Abbey, A. F., et al. 2009, A&A, 494, 775. doi:10.1051/0004-6361:200811157
- Goldberg, D. M., Jones, T. D., Hoyle, F., et al. 2005, ApJ, 621, 643. doi:10.1086/427679
- Gong, Y., Ma, Y.-Z., & Tanimura, H. 2019, MNRAS, 486, 4904. doi:10.1093/mnras/stz1177
- González-Martín, O., Masegosa, J., García-Bernete, I., et al. 2019, ApJ, 884, 11.  
doi:10.3847/1538-4357/ab3e4f
- Gordon, Y. A., Pimblet, K. A., Owers, M. S., et al. 2018, MNRAS, 475, 4223
- Goulding, A. D., Greene, J. E., Bezanson, R., et al. 2018, PASJ, 70, S37
- Govoni, F., Taylor, G. B., Dallacasa, D., et al. 2001, A&A, 379, 807. doi:10.1051/0004-6361:20011355
- Green, P. J., MacLeod, C., Anderson, S. F., et al. 2017, AAS
- Gregory, S. A. & Thompson, L. A. 1978, ApJ, 222, 784. doi:10.1086/156198
- Gu, M.-F. & Ai, Y. L. 2011, A&A, 528, A95. doi:10.1051/0004-6361/201016280
- Gunn, J. E., & Gott, J. R. 1972, ApJ, 176, 1
- Habouzit, M., Pisani, A., Goulding, A., et al. 2020, MNRAS, 493, 899.  
doi:10.1093/mnras/staa219
- Haggard, D., Green, P. J., Anderson, S. F., et al. 2010, ApJ, 723, 1447
- Hajian, A., Battaglia, N., Spergel, D. N., et al. 2013, J. Cosmology Astropart. Phys., 2013, 064. doi:10.1088/1475-7516/2013/11/064
- Hamaus, N., Pisani, A., Sutter, P. M., et al. 2016, Phys. Rev. Lett., 117, 091302.  
doi:10.1103/PhysRevLett.117.091302
- Hardcastle, M. J. & Croston, J. H. 2020, New A Rev., 88, 101539.  
doi:10.1016/j.newar.2020.101539
- Hasinger, G., Miyaji, T., & Schmidt, M. 2005, A&A, 441, 417

- Hawken, A. J., Aubert, M., Pisani, A., et al. 2020, *J. Cosmology Astropart. Phys.*, 2020, 012. doi:10.1088/1475-7516/2020/06/012
- He, Z., Jiang, N., Wang, T., et al. 2021, *ApJ*, 907, L29. doi:10.3847/2041-8213/abd7fd
- Helsdon, S. F. & Ponman, T. J. 2000, *MNRAS*, 319, 933. doi:10.1046/j.1365-8711.2000.03916.x
- Henden, A. A., Templeton, M., Terrell, D., et al. 2016, *VizieR Online Data Catalog*, II/336
- Hernquist, L. 1989, *Nature*, 340, 687
- Hill, J., Burrows, D., Nousek, J., et al. 2004, *APS April Meeting Abstracts*
- HI4PI Collaboration, Ben Bekhti, N., Flöer, L., et al. 2016, *A&A*, 594, A116
- Hoffmeister, C. 1929, *Astronomische Nachrichten*, 236, 233. doi:10.1002/asna.19292361502
- Holt, S. S. & McCray, R. 1982, *ARA&A*, 20, 323. doi:10.1146/annurev.aa.20.090182.001543
- Hopkins, P. F., Hernquist, L., Cox, T. J., et al. 2005, *ApJ*, 630, 705
- Hopkins, P. F., Hernquist, L., Martini, P., et al. 2005, *ApJ*, 625, L71
- Hopkins, P. F., Hernquist, L., Cox, T. J., et al. 2008, *ApJS*, 175, 356
- Hopkins, P. F., & Hernquist, L. 2009, *ApJ*, 698, 1550
- Hopkins, P. F., Kocevski, D. D., & Bundy, K. 2014, *MNRAS*, 445, 823
- Horner, D. J., Perlman, E. S., Ebeling, H., et al. 2008, *ApJS*, 176, 374
- Hovatta, T., Valtaoja, E., Tornikoski, M., et al. 2009, *A&A*, 494, 527
- Hoyle, F., Rojas, R. R., Vogeley, M. S., et al. 2005, *ApJ*, 620, 618. doi:10.1086/427176
- Icke, V. 1984, *MNRAS*, 206, 1P. doi:10.1093/mnras/206.1.1P
- Igumenshchev, I. V., Illarionov, A. F., & Abramowicz, M. A. 1999, *ApJ*, 517, L55. doi:10.1086/312016
- Ishibashi, W., Auger, M. W., Zhang, D., et al. 2014, *MNRAS*, 443, 1339
- Isler, J. C., Urry, C. M., Coppi, P., et al. 2013, *ApJ*, 779, 100
- Isler, J. C., Urry, C. M., Bailyn, C., et al. 2015, *ApJ*, 804, 7
- Jaffe, W., Meisenheimer, K., Röttgering, H. J. A., et al. 2004, *Nature*, 429, 47. doi:10.1038/nature02531
- Jayasinghe, T., Kochanek, C. S., Stanek, K. Z., et al. 2018, *MNRAS*, 477, 3145
- Jayasinghe, T., Stanek, K. Z., Kochanek, C. S., et al. 2019, *MNRAS*, 485, 961

- Jha, V. K., Joshi, R., Chand, H., et al. 2022, MNRAS, 511, 3005.  
doi:10.1093/mnras/stac109
- Jiang, Y.-F., Stone, J. M., & Davis, S. W. 2013, ApJ, 778, 65. doi:10.1088/0004-637X/778/1/65
- Jiang, Y.-F. & Blaes, O. 2020, ApJ, 900, 25. doi:10.3847/1538-4357/aba4b7
- Jones, C. & Forman, W. 1984, ApJ, 276, 38. doi:10.1086/161591
- Jones, C. & Forman, W. 1992, Clusters and Superclusters of Galaxies, 366, 49.  
doi:10.1007/978-94-011-2482-9\_4
- Kaiser, N. 1986, MNRAS, 222, 323. doi:10.1093/mnras/222.2.323
- Kaspi, S., Maoz, D., Netzer, H., et al. 2005, ApJ, 629, 61. doi:10.1086/431275
- Katebi, R., Chornock, R., Berger, E., et al. 2019, MNRAS, 487, 4057.  
doi:10.1093/mnras/stz1552
- Kauffmann, G., & Haehnelt, M. 2000, MNRAS, 311, 576
- Kauffmann, G., Heckman, T. M., Tremonti, C., et al. 2003, MNRAS, 346, 1055.  
doi:10.1111/j.1365-2966.2003.07154.x
- Kauffmann, G., White, S. D. M., Heckman, T. M., et al. 2004, MNRAS, 353, 713
- Kaviraj, S., Devriendt, J. E. G., Ferreras, I., et al. 2005, MNRAS, 360, 60.  
doi:10.1111/j.1365-2966.2005.08883.x
- Kawaguchi, T., Mineshige, S., Umemura, M., et al. 1998, ApJ, 504, 671
- Kawata, D. & Gibson, B. K. 2005, MNRAS, 358, L16. doi:10.1111/j.1745-3933.2005.00018.x
- Kellermann, K. I., Sramek, R., Schmidt, M., et al. 1989, AJ, 98, 1195. doi:10.1086/115207
- Kellermann, K. I. 1992, Science, 258, 145. doi:10.1126/science.258.5079.145
- Kelly, B. C., Bechtold, J., & Siemiginowska, A. 2009, ApJ, 698, 895. doi:10.1088/0004-637X/698/1/895
- Khachikian, E. Y. & Weedman, D. W. 1974, ApJ, 192, 581. doi:10.1086/153093
- Kirshner, R. P., Oemler, A., Schechter, P. L., et al. 1981, ApJ, 248, L57. doi:10.1086/183623
- Kishimoto, M., Hönig, S. F., Antonucci, R., et al. 2011, A&A, 527, A121. doi:10.1051/0004-6361/201016054
- Kochanek, C. S., Shappee, B. J., Stanek, K. Z., et al. 2017, PASP, 129, 104502
- Kollatschny, W., Ochmann, M. W., Zetzl, M., et al. 2018, A&A, 619, A168.  
doi:10.1051/0004-6361/201833727



- Komatsu, E. & Kitayama, T. 1999, *ApJ*, 526, L1. doi:10.1086/312364
- Koratkar, A., Pian, E., Urry, C. M., et al. 1998, *ApJ*, 492, 173
- Koulouridis, E., & Plionis, M. 2010, *ApJ*, 714, L181
- Koulouridis, E., Poggianti, B., Altieri, B., et al. 2016, *A&A*, 592, A11
- Koulouridis, E., Ricci, M., Giles, P., et al. 2018, *A&A*, 620, A20
- Koulouridis, E., & Bartalucci, I. 2019, *A&A*, 623, L10
- Koulouridis, E., Clerc, N., Sadibekova, T., et al. 2021, *A&A*, 652, A12. doi:10.1051/0004-6361/202140566
- Kravtsov, A. V. & Borgani, S. 2012, *ARA&A*, 50, 353. doi:10.1146/annurev-astro-081811-125502
- Krolik, J. H. 2007, *ApJ*, 661, 52. doi:10.1086/515432
- La Franca, F., Gregorini, L., Cristiani, S., et al. 1994, *AJ*, 108, 1548. doi:10.1086/117176
- Lacerna, I., Rodriguez, F., Montero-Dorta, A. D., et al. 2022, *MNRAS*, 513, 2271. doi:10.1093/mnras/stac1020
- LaMassa, S. M., Cales, S., Moran, E. C., et al. 2015, *AAS*
- Lansbury, G. B., Stern, D., Aird, J., et al. 2017, *ApJ*, 836, 99. doi:10.3847/1538-4357/836/1/99
- Laor, A. & Behar, E. 2008, *MNRAS*, 390, 847. doi:10.1111/j.1365-2966.2008.13806.x
- Larson, R. B., Tinsley, B. M., & Caldwell, C. N. 1980, *ApJ*, 237, 692
- Lavaux, G. & Wandelt, B. D. 2010, *MNRAS*, 403, 1392. doi:10.1111/j.1365-2966.2010.16197.x
- León, G., Majhi, A., Okon, E., et al. 2018, *Phys. Rev. D*, 98, 023512. doi:10.1103/PhysRevD.98.023512
- Lee, J. & Park, D. 2006, *ApJ*, 652, 1. doi:10.1086/507936
- Legrand, L. & Carron, J. 2022, *Phys. Rev. D*, 105, 123519. doi:10.1103/PhysRevD.105.123519
- Li, F., Gu, Y.-Z., Yuan, Q.-R., et al. 2019, *MNRAS*, 484, 3806. doi:10.1093/mnras/stz267
- Li, Q., Yang, X., Liu, C., et al. 2022, *ApJ*, 933, 9. doi:10.3847/1538-4357/ac6e69
- Libeskind, N. I., van de Weygaert, R., Cautun, M., et al. 2018, *MNRAS*, 473, 1195. doi:10.1093/mnras/stx1976

- Lidman, C., Rosati, P., Tanaka, M., et al. 2008, *A&A*, 489, 981. doi:10.1051/0004-6361:200810528
- Liidakis, I., Marchili, N., Angelakis, E., et al. 2017, *MNRAS*, 466, 4625
- Liu, A., Tozzi, P., Ettori, S., et al. 2020, *A&A*, 637, A58. doi:10.1051/0004-6361/202037506
- Lopes, P. A. A., Ribeiro, A. L. B., & Rembold, S. B. 2017, *MNRAS*, 472, 409
- Lovisari, L., Schellenberger, G., Sereno, M., et al. 2020, *ApJ*, 892, 102. doi:10.3847/1538-4357/ab7997
- Lovisari, L., Ettori, S., Gaspari, M., et al. 2021, *Universe*, 7, 139. doi:10.3390/universe7050139
- Lukić, Z., Reed, D., Habib, S., et al. 2009, *ApJ*, 692, 217. doi:10.1088/0004-637X/692/1/217
- MacLeod, C. L., Ivezić, Ž., Kochanek, C. S., et al. 2010, *ApJ*, 721, 1014. doi:10.1088/0004-637X/721/2/1014
- Makino, J., & Hut, P. 1997, *ApJ*, 481, 83
- Malkan, M. A. 1983, *ApJ*, 268, 582. doi:10.1086/160981
- Man, Z.-. yi ., Peng, Y.-. jie ., Kong, X., et al. 2019, *MNRAS*, 1665
- Mantz, A. B., Allen, S. W., Morris, R. G., et al. 2017, *MNRAS*, 472, 2877. doi:10.1093/mnras/stx2200
- Mao, Q., Berlind, A. A., Scherrer, R. J., et al. 2017, *ApJ*, 835, 161. doi:10.3847/1538-4357/835/2/161
- Mao, P., Urry, C. M., Marchesini, E., et al. 2017, *ApJ*, 842, 87. doi:10.3847/1538-4357/aa74b8
- Marchini, A., Bonoli, G., Bellizzi, L., et al. 2019, *The Astronomer's Telegram*, 12886
- Marchese, E., Braito, V., Della Ceca, R., et al. 2012, *MNRAS*, 421, 1803
- Marconi, A. & Hunt, L. K. 2003, *ApJ*, 589, L21. doi:10.1086/375804
- Markevitch, M. 1998, *ApJ*, 504, 27. doi:10.1086/306080
- Marshall, M. A., Shabala, S. S., Krause, M. G. H., et al. 2018, *MNRAS*, 474, 3615
- Marshall, M. A., Ni, Y., Di Matteo, T., et al. 2020, *MNRAS*, 499, 3819. doi:10.1093/mnras/staa2982
- Martini, P., Sivakoff, G. R., & Mulchaey, J. S. 2009, *ApJ*, 701, 66
- Martini, P., Miller, E. D., Brodwin, M., et al. 2013, *ApJ*, 768, 1

- Massaro, E., Giommi, P., Leto, C., et al. 2009, *A&A*, 495, 691
- Matt, G., Guainazzi, M., & Maiolino, R. 2003, *MNRAS*, 342, 422
- Mayall, N. U. 1939, *Lick Observatory Bulletin*, 497, 33.  
doi:10.5479/ADS/bib/1939LicOB.19.33M
- McAlpine, S., Bower, R. G., Rosario, D. J., et al. 2018, *MNRAS*, 481, 3118.  
doi:10.1093/mnras/sty2489
- McNamara, B. R., & Nulsen, P. E. J. 2012, *New Journal of Physics*, 14, 055023
- Meekins, J. F., Fritz, G., Chubb, T. A., et al. 1971, *Nature*, 231, 107. doi:10.1038/231107a0
- Mehrtens, N., Romer, A. K., Hilton, M., et al. 2012, *MNRAS*, 423, 1024.  
doi:10.1111/j.1365-2966.2012.20931.x
- Meier, D. L. 2001, *ApJ*, 548, L9. doi:10.1086/318921
- Melnyk, O., Elyiv, A., Smolčić, V., et al. 2018, *A&A*, 620, A6
- Mesa, V., Duplancic, F., Alonso, S., et al. 2018, *A&A*, 619, A24. doi:10.1051/0004-6361/201832910
- Miller, A. D., Caldwell, R., Devlin, M. J., et al. 1999, *ApJ*, 524, L1. doi:10.1086/312293
- Miller, C. J., Nichol, R. C., Gómez, P. L., et al. 2003, *ApJ*, 597, 142
- Mirzoyan, R. 2020, *The Astronomer's Telegram*, 13412
- Mishra, H. D. & Dai, X. 2020, *AJ*, 159, 69. doi:10.3847/1538-3881/ab6225
- Mishra, H. D., Dai, X., Chen, P., et al. 2021, *ApJ*, 913, 146. doi:10.3847/1538-4357/abf63d
- Mishra, H. D., Dai, X., & Guerras, E. 2021, *ApJ*, 922, L17. doi:10.3847/2041-8213/ac36d9
- Mo, H., van den Bosch, F. C., & White, S. 2010, *Galaxy Formation and Evolution*, by Houjun Mo, Frank van den Bosch, Simon White, Cambridge, UK: Cambridge University Press, 2010
- Molendi, S. 2004, *Plasmas in the Laboratory and in the Universe: New Insights and New Challenges*, 703, 345. doi:10.1063/1.1718479
- Moore, B., Katz, N., Lake, G., et al. 1996, *Nature*, 379, 613
- Mullis, C. R., McNamara, B. R., Quintana, H., et al. 2003, *ApJ*, 594, 154
- Murata, R., Oguri, M., Nishimichi, T., et al. 2019, *PASJ*, 71, 107. doi:10.1093/pasj/psz092
- Nagao, T., Murayama, T., & Taniguchi, Y. 2001, *ApJ*, 546, 744. doi:10.1086/318300
- Narayan, R. & Yi, I. 1995, *ApJ*, 452, 710. doi:10.1086/176343

- Navarro, J. F., Frenk, C. S., & White, S. D. M. 1996, *ApJ*, 462, 563. doi:10.1086/177173
- Neyrinck, M. C. 2008, *MNRAS*, 386, 2101. doi:10.1111/j.1365-2966.2008.13180.x
- Oh, K., Yi, S. K., Schawinski, K., et al. 2015, *ApJS*, 219, 1. doi:10.1088/0067-0049/219/1/1
- Oke, J. B. & Gunn, J. E. 1974, *ApJ*, 189, L5. doi:10.1086/181450
- Oort, J. H. 1983, *ARA&A*, 21, 373. doi:10.1146/annurev.aa.21.090183.002105
- Osterbrock, D. E. & Ferland, G. J. 2006, *Astrophysics of gaseous nebulae and active galactic nuclei*, 2nd. ed. by D.E. Osterbrock and G.J. Ferland. Sausalito, CA: University Science Books, 2006
- Ostriker, J. P., Peebles, P. J. E., & Yahil, A. 1974, *ApJ*, 193, L1. doi:10.1086/181617
- Padovani, P. 1992, *MNRAS*, 257, 404. doi:10.1093/mnras/257.3.404
- Padovani, P. & Giommi, P. 1995, *MNRAS*, 277, 1477. doi:10.1093/mnras/277.4.1477
- Padovani, P., Alexander, D. M., Assef, R. J., et al. 2017, *A&A Rev.*, 25, 2. doi:10.1007/s00159-017-0102-9
- Paliya, V. S. 2015, *ApJ*, 804, 74. doi:10.1088/0004-637X/804/1/74
- Paiano, S., Falomo, R., Treves, A., et al. 2020, *MNRAS*, 497, 94
- Pan, D. C., Vogeley, M. S., Hoyle, F., et al. 2012, *MNRAS*, 421, 926. doi:10.1111/j.1365-2966.2011.20197.x
- Panessa, F., Baldi, R. D., Laor, A., et al. 2019, *Nature Astronomy*, 3, 387. doi:10.1038/s41550-019-0765-4
- Pâris, I., Petitjean, P., Ross, N. P., et al. 2017, *A&A*, 597, A79. doi:10.1051/0004-6361/201527999
- Paz, D., Lares, M., Ceccarelli, L., et al. 2013, *MNRAS*, 436, 3480. doi:10.1093/mnras/stt1836
- Peacock, J. A. 1987, *Astrophysical Jets and their Engines*, 208, 185
- Peebles, P. J. E. & Yu, J. T. 1970, *ApJ*, 162, 815. doi:10.1086/150713
- Peebles, P. J. E. 1980, *Large-Scale Structure of the Universe* by Phillip James Edwin Peebles. Princeton University Press, 1980. ISBN: 978-0-691-08240-0
- Peebles, P. J. E. 1982, *ApJ*, 263, L1. doi:10.1086/183911
- Perlman, E. S., Horner, D. J., Jones, L. R., et al. 2002, *ApJS*, 140, 265
- Perez, E., Penston, M. V., & Moles, M. 1989, *MNRAS*, 239, 75
- Peterson, B. M., Wanders, I., Horne, K., et al. 1998, *PASP*, 110, 660

- Peterson, B. M., Ferrarese, L., Gilbert, K. M., et al. 2004, *ApJ*, 613, 682
- Pichel, A., Donoso, L. G., Baravalle, L. D., et al. 2020, *MNRAS*, 491, 3448.  
doi:10.1093/mnras/stz3239
- Pier, E. A. & Krolik, J. H. 1992, *ApJ*, 399, L23. doi:10.1086/186597
- Pier, E. A. & Krolik, J. H. 1993, *ApJ*, 418, 673. doi:10.1086/173427
- Piffaretti, R., Arnaud, M., Pratt, G. W., et al. 2011, *A&A*, 534, A109
- Pimblett, K. A., Shabala, S. S., Haines, C. P., et al. 2013, *MNRAS*, 429, 1827
- Pisani, A., Massara, E., Spergel, D. N., et al. 2019, *BAAS*, 51, 40
- Platen, E., van de Weygaert, R., & Jones, B. J. T. 2007, *MNRAS*, 380, 551.  
doi:10.1111/j.1365-2966.2007.12125.x
- Platen, E., van de Weygaert, R., & Jones, B. J. T. 2008, *MNRAS*, 387, 128.  
doi:10.1111/j.1365-2966.2008.13019.x
- Plionis, M., López-Cruz, O., & Hughes, D. 2008, *A Pan-Chromatic View of Clusters of Galaxies and the Large-Scale Structure*, edited by M. Plionis, O. López-Cruz and D. Hughes. *Lecture Notes in Physics Vol. 740*. 474 p. 24 illus. in color., Hardcover, ISBN: 978-1-4020-6940-6. Published by Springer, Dordrecht, The Netherlands, 2008., 24. doi:10.1007/978-1-4020-6941-3
- Poggianti, B. M., Jaffé, Y. L., Moretti, A., et al. 2017, *Nature*, 548, 304
- Popesso, P., Böhringer, H., Brinkmann, J., et al. 2004, *A&A*, 423, 449. doi:10.1051/0004-6361:20035818
- Porqueres, N., Jasche, J., Enßlin, T. A., et al. 2018, *A&A*, 612, A31. doi:10.1051/0004-6361/201732141
- Postman, M., Lubin, L. M., Gunn, J. E., et al. 1996, *AJ*, 111, 615. doi:10.1086/117811
- Potter, W. J. & Cotter, G. 2013, *MNRAS*, 429, 1189. doi:10.1093/mnras/sts407
- Poudel, A., Heinämäki, P., Tempel, E., et al. 2017, *A&A*, 597, A86. doi:10.1051/0004-6361/201629639
- Pratt, G. W., Arnaud, M., Piffaretti, R., et al. 2010, *A&A*, 511, A85. doi:10.1051/0004-6361/200913309
- Prince, R., Khatoon, R., & Gupta, N. 2019, *The Astronomer's Telegram*, 13353
- Prince, R., Khatoon, R., & Stalin, C. S. 2021, *MNRAS*, 502, 5245.  
doi:10.1093/mnras/stab369
- Pushkarev, A. B., Hovatta, T., Kovalev, Y. Y., et al. 2012, *A&A*, 545, A113.  
doi:10.1051/0004-6361/201219173

- Ramos Almeida, C. & Ricci, C. 2017, *Nature Astronomy*, 1, 679. doi:10.1038/s41550-017-0232-z
- Randall, S. W., Clarke, T. E., van Weeren, R. J., et al. 2016, *ApJ*, 823, 94. doi:10.3847/0004-637X/823/2/94
- Raouf, M., Khosroshahi, H. G., Ponman, T. J., et al. 2014, *MNRAS*, 442, 1578
- Raouf, M., Silk, J., Shabala, S. S., et al. 2019, *MNRAS*, 486, 1509
- Reid, B., Ho, S., Padmanabhan, N., et al. 2016, *MNRAS*, 455, 1553. doi:10.1093/mnras/stv2382
- Ricarte, A., Tremmel, M., Natarajan, P., et al. 2019, *MNRAS*, 489, 802. doi:10.1093/mnras/stz2161
- Ricarte, A., Tremmel, M., Natarajan, P., et al. 2020, *ApJ*, 895, L8. doi:10.3847/2041-8213/ab9022
- Ricker, G. R., Winn, J. N., Vanderspek, R., et al. 2015, *Journal of Astronomical Telescopes, Instruments, and Systems*, 1, 014003
- Rigby, E. E., Best, P. N., Brookes, M. H., et al. 2011, *MNRAS*, 416, 1900. doi:10.1111/j.1365-2966.2011.19167.x
- Robichaud, F., Williamson, D., Martel, H., et al. 2017, *MNRAS*, 469, 3722. doi:10.1093/mnras/stx1121
- Rodriguez-Gomez, V., Genel, S., Vogelsberger, M., et al. 2015, *MNRAS*, 449, 49
- Rojas, R. R., Vogeley, M. S., Hoyle, F., et al. 2004, *ApJ*, 617, 50. doi:10.1086/425225
- Romer, A. K., Nichol, R. C., Holden, B. P., et al. 2000, *ApJS*, 126, 209
- Ross, N. P., Myers, A. D., Sheldon, E. S., et al. 2012, *ApJS*, 199, 3. doi:10.1088/0067-0049/199/1/3
- Rowan-Robinson, M. 1977, *ApJ*, 213, 635. doi:10.1086/155195
- Sahni, V., Sathyaprakah, B. S., & Shandarin, S. F. 1994, *ApJ*, 431, 20. doi:10.1086/174464
- Sahlén, M., Zubeldía, Í., & Silk, J. 2016, *ApJ*, 820, L7. doi:10.3847/2041-8205/820/1/L7
- Sambruna, R. M., Gliozzi, M., Eracleous, M., et al. 2003, *ApJ*, 586, L37. doi:10.1086/374612
- Sandage, A. 1965, *ApJ*, 141, 1560. doi:10.1086/148245
- Sanders, D. B., Soifer, B. T., Elias, J. H., et al. 1988, *ApJ*, 325, 74
- Sarazin, C. L. 1986, *Reviews of Modern Physics*, 58, 1. doi:10.1103/RevModPhys.58.1
- Saripalli, L. 2012, *AJ*, 144, 85. doi:10.1088/0004-6256/144/3/85

- Sbarrato, T., Ghisellini, G., Giovannini, G., et al. 2021, *A&A*, 655, A95. doi:10.1051/0004-6361/202141827
- Schlegel, D. J., Finkbeiner, D. P., & Davis, M. 1998, *ApJ*, 500, 525
- Schmitt, J. L. 1968, *Nature*, 218, 663. doi:10.1038/218663a0
- Sesar, B., Ivezić, Ž., Lupton, R. H., et al. 2007, *AJ*, 134, 2236
- Shakura, N. I. & Sunyaev, R. A. 1973, *A&A*, 24, 337
- Shankar, F., Weinberg, D. H., & Miralda-Escudé, J. 2009, *ApJ*, 690, 20
- Shankar, F., Marulli, F., Mathur, S., et al. 2012, *A&A*, 540, A23
- Shappee, B. J., Prieto, J. L., Grupe, D., et al. 2014, *ApJ*, 788, 48
- Shaver, P. A., Hook, I. M., Jackson, C. A., et al. 1999, *Highly Redshifted Radio Lines*, 156, 163
- Shen, Y., Richards, G. T., Strauss, M. A., et al. 2011, *ApJS*, 194, 45
- Sheth, R. K. & van de Weygaert, R. 2004, *MNRAS*, 350, 517. doi:10.1111/j.1365-2966.2004.07661.x
- Shields, G. A. 1999, *PASP*, 111, 661. doi:10.1086/316378
- Shimakawa, R., Tanaka, M., Bottrell, C., et al. 2022, *PASJ*, 74, 612. doi:10.1093/pasj/psac023
- Shin, M.-S., Ostriker, J. P., & Ciotti, L. 2010, *ApJ*, 711, 268. doi:10.1088/0004-637X/711/1/268
- Shirasaki, Y., Akiyama, M., Nagao, T., et al. 2018, *PASJ*, 70, S30
- Silk, J. & Rees, M. J. 1998, *A&A*, 331, L1
- Silk, J. 2005, *MNRAS*, 364, 1337. doi:10.1111/j.1365-2966.2005.09672.x
- Silverman, J. D., Kovač, K., Knobel, C., et al. 2009, *ApJ*, 695, 171
- Singh, V., Shastri, P., & Risaliti, G. 2011, *A&A*, 532, A84. doi:10.1051/0004-6361/201016387
- Smith, P. S., Balonek, T. J., Heckert, P. A., et al. 1986, *ApJ*, 305, 484. doi:10.1086/164261
- Smith, P. S., Elston, R., Berriman, G., et al. 1988, *ApJ*, 326, L39. doi:10.1086/185119
- Spinoglio, L. & Fernández-Ontiveros, J. A. 2021, *Nuclear Activity in Galaxies Across Cosmic Time*, 356, 29. doi:10.1017/S1743921320002549
- Springel, V., White, S. D. M., Jenkins, A., et al. 2005, *Nature*, 435, 629. doi:10.1038/nature03597

- Springel, V., Di Matteo, T., & Hernquist, L. 2005, MNRAS, 361, 776
- Stanek, R., Evrard, A. E., Böhringer, H., et al. 2006, ApJ, 648, 956. doi:10.1086/506248
- Stanek, K. Z., Kochanek, C. S., Thompson, T. A., et al. 2017, The Astronomer's Telegram, 11110
- Stern, D., Eisenhardt, P., Gorjian, V., et al. 2005, ApJ, 631, 163
- Stern, D., Assef, R. J., Benford, D. J., et al. 2012, ApJ, 753, 30
- Storchi Bergmann, T. 2015, Galaxies in 3D across the Universe, 309, 190. doi:10.1017/S1743921314009648
- Strazzullo, V., Rosati, P., Pannella, M., et al. 2010, A&A, 524, A17. doi:10.1051/0004-6361/201015251
- Sunyaev, R. A. & Zeldovich, Y. B. 1970, Ap&SS, 7, 3. doi:10.1007/BF00653471
- Sunyaev, R. A. 1974, Confrontation of Cosmological Theories with Observational Data, 63, 167
- Sutter, P. M., Elahi, P., Falck, B., et al. 2014, MNRAS, 445, 1235. doi:10.1093/mnras/stu1845
- Tadhunter, C. 2016, A&A Rev., 24, 10. doi:10.1007/s00159-016-0094-x
- Takey, A., Durret, F., Mahmoud, E., et al. 2016, A&A, 594, A32. doi:10.1051/0004-6361/201628105
- Takizawa, M. 1998, ApJ, 509, 579. doi:10.1086/306530
- Tempel, E., Stoica, R. S., Martínez, V. J., et al. 2014, MNRAS, 438, 3465. doi:10.1093/mnras/stt2454
- Tody, D. 1986, Proc. SPIE, 627, 733
- Tran, K.-V. H., van Dokkum, P., Franx, M., et al. 2005, ApJ, 627, L25
- Travascio, A., Bongiorno, A., Tozzi, P., et al. 2020, MNRAS, 498, 2719. doi:10.1093/mnras/staa2495
- Trindade Falcão, A., Kraemer, S. B., Fischer, T. C., et al. 2021, MNRAS, 505, 3054. doi:10.1093/mnras/stab1549
- Uklein, R. I., Malygin, E. A., Shablovinskaya, E. S., et al. 2019, Astrophysical Bulletin, 74, 388. doi:10.1134/S1990341319040059
- Ulrich, M.-H., Maraschi, L., & Urry, C. M. 1997, ARA&A, 35, 445. doi:10.1146/annurev.astro.35.1.445
- Urry, C. M. & Padovani, P. 1995, PASP, 107, 803. doi:10.1086/133630



- Urry, C. 2004, *AGN Physics with the Sloan Digital Sky Survey*, 311, 49
- Vallés-Pérez, D., Quilis, V., & Planelles, S. 2021, *ApJ*, 920, L2. doi:10.3847/2041-8213/ac2816
- Vallely, P. J., Fausnaugh, M., Jha, S. W., et al. 2019, *MNRAS*, 487, 2372
- Vermeulen, R. C., Ogle, P. M., Tran, H. D., et al. 1995, *ApJ*, 452, L5
- Verza, G., Pisani, A., Carbone, C., et al. 2019, *J. Cosmology Astropart. Phys.*, 2019, 040. doi:10.1088/1475-7516/2019/12/040
- Villforth, C., Hamilton, T., Pawlik, M. M., et al. 2017, *Galaxy Evolution Across Time*, 9
- Voges, W., Boller, T., & Supper, R. 1999, 26th International Cosmic Ray Conference (ICRC26), Volume 4, 4, 47
- Waddington, I., Dunlop, J. S., Peacock, J. A., et al. 2001, *MNRAS*, 328, 882. doi:10.1046/j.1365-8711.2001.04934.x
- White, S. D. M., Frenk, C. S., & Davis, M. 1983, *ApJ*, 274, L1. doi:10.1086/184139
- Wilson, A. S. 1997, *IAU Colloq. 159: Emission Lines in Active Galaxies: New Methods and Techniques*, 113, 264
- Woo, J.-H. & Urry, C. M. 2002, *ApJ*, 579, 530. doi:10.1086/342878
- Wright, E. L., Eisenhardt, P. R. M., Mainzer, A. K., et al. 2010, *AJ*, 140, 1868
- Wu, S., Lu, Y., Zhang, F., et al. 2013, *MNRAS*, 436, 3271. doi:10.1093/mnras/stt1811
- Yang, G., Brandt, W. N., Vito, F., et al. 2018, *MNRAS*, 475, 1887
- Xu, W. L. & Randall, L. 2020, *ApJ*, 900, 69. doi:10.3847/1538-4357/aba51f
- Yee, H. K. C. & Gladders, M. D. 2002, *AMiBA 2001: High-Z Clusters, Missing Baryons, and CMB Polarization*, 257, 109
- Yoo, S. & An, H. 2020, *ApJ*, 902, 2. doi:10.3847/1538-4357/abb3c1
- Yu, Z., Kochanek, C. S., Peterson, B. M., et al. 2020, *MNRAS*, 491, 6045. doi:10.1093/mnras/stz3464
- Zanisi, L., Shankar, F., Fu, H., et al. 2021, *MNRAS*, 505, 4555. doi:10.1093/mnras/stab1472
- Zeldovich, Y. B. & Sunyaev, R. A. 1969, *Ap&SS*, 4, 301. doi:10.1007/BF00661821
- Zeldovich, I. B., Einasto, J., & Shandarin, S. F. 1982, *Nature*, 300, 407. doi:10.1038/300407a0
- Zhang, B.-K., Zhou, X.-S., Zhao, X.-Y., et al. 2015, *Research in Astronomy and Astrophysics*, 15, 1784. doi:10.1088/1674-4527/15/11/002

- Zhang, X. & Huang, Q.-G. 2018, arXiv:1812.01877
- Zhang, C., Zhuravleva, I., Kravtsov, A., et al. 2021, MNRAS, 506, 839.  
doi:10.1093/mnras/stab1546
- Zhao, D., Ho, L. C., Zhao, Y., et al. 2019, ApJ, 877, 52
- Zheng, W., & Burbidge, E. M. 1986, ApJ, 306, L67
- Zu, Y., Kochanek, C. S., & Peterson, B. M. 2011, ApJ, 735, 80
- Zwicky, F. 1933, Helvetica Physica Acta, 6, 110
- Zuhone, J. & Markevitch, M. 2009, The Monster's Fiery Breath: Feedback in Galaxies, Groups, and Clusters, 1201, 383. doi:10.1063/1.3293082
- Zwicky, F., Herzog, E., & Wild, P. 1968, Pasadena: California Institute of Technology (CIT), 1961-1968